ABSTRACT

Title of Dissertation:	A 20-YEAR CLIMATOLOGY OF GLOBAL ATMOSPHERIC METHANE FROM HYPERSPECTRAL THERMAL INFRARED SOUNDERS WITH SOME APPLICATIONS
	Lihang Zhou, Doctor of Philosophy, 2022
Dissertation directed by:	Dr. Juying Xie Warner, Department of Atmospheric and Oceanic Science

Atmospheric Methane (CH_4) is the second most important greenhouse gas after carbon dioxide (CO_2), and accounts for approximately 20% of the global warming produced by all well-mixed greenhouse gases. Thus, its spatiotemporal distributions and relevant long-term trends are critical to understanding the sources, sinks, and global budget of atmospheric composition, as well as the associated climate impacts. The current suite of hyperspectral thermal infrared sounders has provided continuous global methane data records since 2002, starting with the Atmospheric Infrared Sounder (AIRS) onboard the NASA EOS/Aqua satellite launched on 2 May 2002. The Cross-track Infrared Sounder (CrIS) was launched onboard the Suomi National Polar Orbiting Partnership (SNPP) on 28 October 2011 and then on NOAA-20 on 18 November 2017. The Infrared Atmospheric Sounding Interferometer (IASI) was launched onboard the EUMETSAT MetOp-A on 19 October 2006, followed by MetOp-B on 17 September 2012, then Metop-C on 7 November 2018.

In this study, nearly two decades of global CH_4 concentrations retrieved from the AIRS and CrIS sensors were analyzed. Results indicate that the global mid-upper tropospheric CH_4 concentrations (centered around 400 hPa) increased significantly from 2003 to 2020, i.e., with an annual average of ~1754 ppbv in 2003 and ~1839 ppbv in 2020. The total increase is approximately 85 ppbv representing a +4.8% change in 18 years. More importantly, the rate of increase was derived using satellite measurements and shown to be consistent with the rate of increase previously reported only from in-situ observational measurements. It further confirmed that there was a steady increase starting in 2007 that became stronger since 2014, as also reported from the in-situ observations. In addition, comparisons of the methane retrieved from the AIRS and CrIS against in situ measurements from NOAA Global Monitoring Laboratory (GML) were conducted. One of the key findings of this comparative study is that there are phase shifts in the seasonal cycles between satellite thermal infrared measurements and ground measurements, especially in the middle to high latitudes in the northern hemisphere. Through this, an issue common in the hyperspectral thermal sensor retrievals were discovered that was unknown previously and offered potential solutions. We also conducted research on some applications of the retrieval products in monitoring the changes of CH_4 over the selected regions (the Arctic and South America). Detailed analyses based on local geographic changes related to CH_4 concentration increases were discussed. The results of this study concluded that while the atmospheric CH_4 concentration over the Arctic region has been increasing since the early 2000s, there were no catastrophic sudden jumps during the period of 2008-2012, as indicated by the earlier studies using pre-validated retrieval products. From our study of CH_4 climatology using hyperspectral infrared sounders, it has been proved that the CH_4 from hyperspectral sounders provide valuable information on CH_4 for the mid-upper troposphere and lower stratosphere. Future approaches are suggested that include: 1) Utilizing

extended data records for CH_4 monitoring using AIRS, CrIS, and other potential new generation hyperspectral infrared sensors; 2). Improving the algorithms for trace gas retrievals; and 3). Enhancing the capacity to detect CH_4 changes and anomalies with radiance signals from hyperspectral infrared sounders.

A 20-YEAR CLIMATOLOGY OF GLOBAL ATMOSPHERIC METHANE FROM HYPERSPECTRAL THERMAL INFRARED SOUNDERS WITH SOME APPLICATIONS

By

Lihang Zhou

Dissertation submitted to the Faculty of the Graduate School of the
University of Maryland, College Park, in partial fulfillment
of the requirements for the degree of
Doctor of Philosophy
2022

Advisory Committee:
Professor Juying Xie Warner, Co-Chair
Professor Rachel Pinker, Co-Chair
Professor Da-Lin Zhang
Professor Hugo Berbery
Professor Dongdong Wang, Dean's representative

Preface

This work consists of studies focused on analyzing global methane observed from hyperspectral thermal infrared sounders. Atmospheric methane and its importance are introduced in Chapter 1. Chapter 2 describes the hyperspectral thermal infrared sensors and the methane retrieval algorithms. Chapter 3 presents a climatology of global atmospheric methane revealed from the two decades of the hyperspectral thermal infrared sounders, followed by Chapter 4 showing the latitudinal distributions of methane and the inter polar differences. Chapter 5 describes two focused studies that were conducted over South America and the Arctic, and a unique technology to detect methane changes and anomalies using the radiance information. Chapter 6 gives a summary and conclusions of this study. The areas of future work are discussed in the final chapter.

Among all the studies, Chapters 3 and 4 have been summarized in a manuscript that was submitted to the *Journal of Remote Sensing,* which is currently undergoing revision (Zhou et al., 2022). During my study, I have also led a paper on the science performance of the NOAA operational polar satellite products (Zhou et al., 2019), and was second authors of two papers published in related areas: 1) The long-term sensor data records (Zou, Zhou et al., 2020), and 2) Outgoing Longwave Radiation (Wang, Zhou et al., 2021).

Dedication

To my husband Jerry, my daughter Annie for your love and support. To my parents Cihuan and Angong, for their unconditional love and encouragement.

Acknowledgements

First and foremost, I would like to thank my family for their continuous support and love.

I deeply appreciate the Department of Atmospheric and Oceanic Science, University of Maryland, College Park, for the opportunities to complete my degree work. I am extremely thankful to my advisor, Professor Juying Xie Warner, for spending numerous evenings and weekends with me through the past few years. Her encouragement and guidance resulted in a study will inspire new research and findings. I am also grateful to my committee, led by Professors Warner and Professor Pinker, and joined by Professor Da-Lin Zhang, Professor Hugo Berbery, and Dean's Representative/Professor Dongdong Wang. I would like to thank my NOAA supervisors, particularly Dr. Mitch Goldberg, for his advice and guidance throughout my career.

I want to thank my colleagues for their work on the sounding algorithms: Satya Kalluri, Chris Barnet, Walter Wolf, Xingpin Liu, Murty Divakarla, Nick Nalli, Ken Pryor, Flavio Iturbide-Sanchez, Mark Liu, Tong Zhu, Changyi Tian, Xiaozhen Xiong, Tianyuan Wang, Antonia Gambacorta, Eric Maddy, Tom King, Nadia Smith, and Rebekah Esmailli. I would like to particularly thank Zigang Wei for his help for data and coding. Thanks to Annie and Casey for their help for editing. I want to thank NOAA CLASS for the data, and my colleagues in Global Monitoring Lab (GML) for many discussions. I am grateful to NASA GES and AIRS team for making the data and tools publicly available for this study.

Table of Content

List of Tables

List of Figures

Chapter 1: Introduction

1.1 Motivation for Studies

Atmospheric methane (CH_4) is a potent greenhouse gas and responsible for approximately 20% of the warming produced by well-mixed greenhouse gases (Ramanathan et al., 1985; IPCC 2001, 2013). According to the climate data reconstructed from polar ice core records (Etheridge et al., 1998; Rubino et al., 2019; Nisbet et al., 2019), the concentration of CH_4 in 2019 has more than doubled since pre-industrial time (see Fig. 1). While the atmospheric CH_4 concentration is much smaller than that of CO_2, the observed CH_4 increase can still lead to a substantial impact on the climate system because CH_4 has a Global Warming Potential (GWP) 84 and 28 times larger than CO_2 for a time horizon of 20 and 100 years, respectively, as shown in Table 1 (Kirschke et al., 2013; Voulgarakis et al., 2013; Saunois et al., 2016; Dave Crisp et al., 2018). CH_4 also produces tropospheric ozone which is another greenhouse gas and a pollutant with negative impacts on human health and ecosystems.

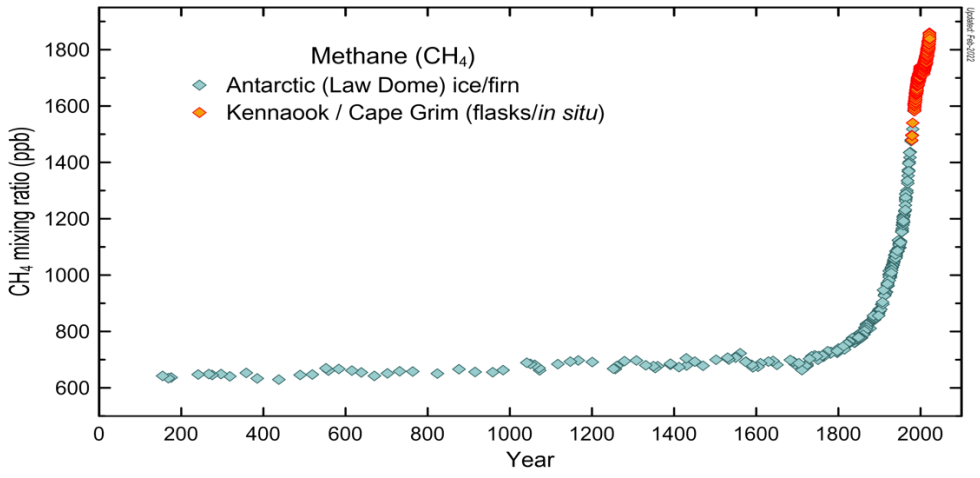

Fig. 1: Atmospheric CH_4 concentrations (in ppb) over the last 2000 years, based on measurements of air trapped in Antarctic ice and firn, shown in blue-gray diamonds, and the modern Cape Grim in situ record, shown in orange (updated Feb 2022, Source: BoM/CSIRO/AAD).

Table 1: Comparison of major Short-lived climate pollutants (SLCPs) and CO_2. Data was collected from Myhre et al. (2013).

Name	Molar mass (g mol^{-1})	Atmospheric lifetime	Global annual emission (Gt)	GWP 20	GWP 100
Carbon dioxide (CO_2)	44.01	Hundreds to thousands of years	3.69×10^7	1	1
Methane (CH_4)	16.04	12.4 years	3.64×10^5	84	28
Black carbon	–	7 to 10 days	5.31×10^3	1600	460
Tropospheric ozone (O_3)	48.00	Hours to weeks	–	–	–
HFC-134a (CH_2FCF_3)	102.03	13.4 years	163	3710	1300
HFC-152a (CH_3CHF_2)	66.05	1.5 years	27.9	506	138

Atmospheric CH_4 concentrations have changed dramatically in the past four decades (Shindell et al., 2021), rising rapidly in the 1980s, then going into a brief plateau period from 2000-2006. Atmospheric CH_4 concentration began increasing again globally after 2007 (Dlugokencky et al., 2009; Nisbet et al 2016; Rigby et al., 2009). Between 2005 and 2017, all inventories, except Environment Protection Agency (EPA), inferred an increase in emissions as fast as the warmest scenarios assessed by the recent Intergovernmental Panel on Climate Change (IPCC) report (IPCC, 2021), as shown in Fig.2. CH_4 concentrations rose even more rapidly from 2014 onward (Nisbet et al., 2019). Without further actions and regulations, CH_4 emissions are projected to continuously increase through the 2040s. In IPCC 2021, reducing human caused CH_4 emission was identified as one of the most cost-effective strategies to slow down the rate of warming and would contribute significantly to global efforts to limit temperature warming to less than 2ºC (with an aspiration for less than 1.5ºC) from pre-industrial levels (UNFCCC, 2015). Due to the importance of CH_4 in meeting global climate targets, it is critical to understand the past and current statuses while monitoring CH_4 trends in future years. This will help assess the efficiency of mitigation policies and define the pathways that constrain global warming (Nisbet et al., 2020).

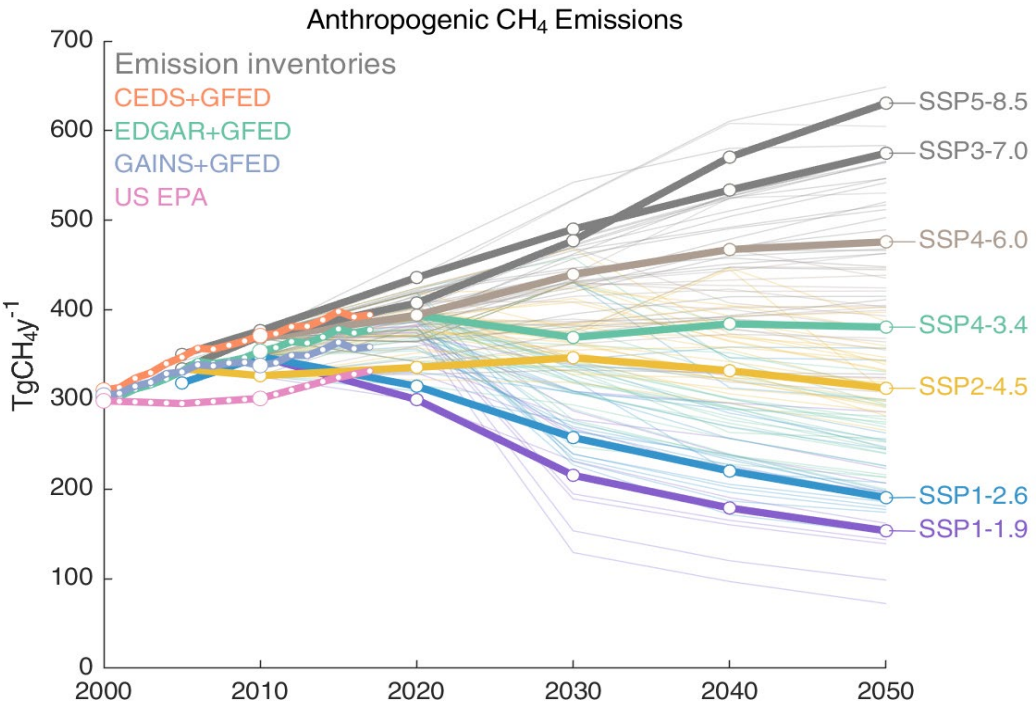

Fig. 2: Anthropogenic Methane Emissions & Socioeconomic Pathways (SSPs) (Saunois et al. 2020, ESSD)

1.1.1 CH_4 Sources and Sinks

CH_4 is emitted from a variety of anthropogenic (human-influenced) and natural sources (Fung et al., 1991). Anthropogenic CH_4 emissions account for roughly 60% of total CH_4 emissions, among which, more than 90% comes from fossil fuel (coal, gas/oil extraction, ~35%), agriculture (~40%), and waste (~20%) (Saunois et al., 2016, 2020). Approximately 40% of CH_4 is emitted into the atmosphere by natural sources (e.g., wetlands, inland water, permafrost, wildfire, wild animals, and termites, etc.,) (Saunois et al., 2020). The sink of CH_4 is mostly in the atmosphere by oxidation of CH_4 to CO_2. Therefore, CH_4 plays a key role in the chemical processes occurring in the troposphere through its oxidation by hydroxyl radical (OH). This sink reaction contributes to more than 80% of CH_4 total loss in the troposphere (Levy 1971; Badr et al. 1992; Denman et al. 2007; Kirschke et al. 2013). The rate of OH production depends on atmospheric temperature, water

vapor, and solar irradiance. The concentrations of OH are the highest at low latitudes (Prinn et al., 1987, Lelieveld et al., 2016). Other minor removal processes include uptakes by soil, reactions with chlorine atoms in the marine boundary layer, and transport to the stratosphere where CH_4 is rapidly destroyed by reaction with stratospheric chlorine and oxygen atoms (Saunois et al., 2017; Kirschke et al., 2013).

Comprehensive reports on the global CH_4 budget for the past decade have been published by the Global Carbon Project (GCP): The first report was published in 2013, and it was later updated in 2016. The latest version was recently released in July 2020 (Saunois et al., 2020). The global methane budget for the 2008–2017 decade is described in the latest GCP report (GCP, 2020). Both bottom-up (BU) and top-down (TD) estimates (Tg CH_4 yr^{-1}) were provided for each emission and sink category, as well as for total emissions and total sinks. BU uses diverse data inventories, observation-driven methods, and process-based models, while TD optimally combines measurements of atmospheric CH_4 at more than 100 stations around the world by using a first guess estimate of CH_4 emissions into an atmospheric inversion framework.

Based on the TD estimates for the decade of 2008-2017, the global CH_4 emissions are 576 Tg (550-594), and global CH_4 sink is 556 Tg (501-504) per year. The differences between the sources and sinks are consistent with the observed average imbalance in the atmosphere CH_4 of 13 Tg (0-49) per year. The global CH_4 emissions from BU estimates are 737 Tg (594-881) per year, which are nearly 30% higher than the estimates calculated using TD inversion methods. The BU estimates are higher than TD estimates for natural sources, e.g., other inland water systems, oceans, permafrost, and geological sources. Both TD and BU estimates are in general agreements for agricultural emissions, and biomass and biofuel burning emissions. The BU estimates are lower

than TD estimates for wetland emissions. There is a large discrepancy between TD and BU estimates for freshwaters and natural geological sources.

The most important source of uncertainty in the CH_4 budget is attributable to natural emissions, especially those from wetlands and other inland waters. The natural resources of the methane emissions include vegetated wetland emissions and inland water systems (lakes, small ponds, rivers), land geological sources (gas–oil seeps, mud volcanoes, micro seepage, geothermal manifestations, and volcanoes), wild animals, termites, thawing terrestrial and marine permafrost, and oceanic sources (biogenic, geological, and hydrate).

1.1.2 Changes in CH_4 Emissions

A comparison of the methane budget during the suspension period of increase in atmospheric methane concentration (2000–2006) and the budget assessment for 2017 found that the emissions in 2017 increased by 9%, which is equivalent to an increase of about 50 million tons a year (Jackson et al., 2020). Most of the increase was caused by emissions from human activities. In contrast, the methane emissions from natural sources such as wetlands, lakes and marshes, reservoirs, termites, geological emissions, and hydrates have remained nearly unchanged over the past two decades.

Emissions from anthropogenic activities have increased significantly and contribute to the majority of the 50 Tg CH_4 /yr increased emissions between 2000-2006 and 2017. The main areas contributing to the increase in CH_4 emissions are fossil fuels (production and consumption), agricultural activities, and waste. The increase of emissions is seen in the geographic regions of Africa and the Middle East, China, South Asia and Oceania, North America, and South America. In contrast to these regions, Europe is the only region with reduced emissions, due to the implementation of countermeasures to reduce CH_4 emissions from agricultural and waste fields.

It is critical to monitor the changes of CH_4 and to understand its response and impact on the Earth's climate and environment. Since current ground-based measurements are sparse in remote regions, satellite remote sensing measurements play an important role in assessing the global CH_4 concentration continuously over time. Hyperspectral infrared sounding observations have provided global CH_4 products since 2002 and can be used for monitoring the variation and distributions of atmospheric CH_4. In this study, the changes and distributions of the CH_4 concentration was analyzed by using the products from the nearly two decades of the advanced thermal hyperspectral sounders onboard the United States (U.S.) polar orbit satellites. Since the same type of the instrument is in the technical baseline for Joint Polar Satellite System (JPSS) satellites, the same high-quality hyperspectral observations are expected to be extended to the JPSS-4 timeframe (in the 2040s).

1.2 Objectives

The main goal of this study is to gain an understanding of the global distributions and changes in atmospheric methane derived from the new generation of the hyperspectral instruments (e.g., AIRS and CrIS). Based on the products from the past 20 years, the global distribution, seasonality, and long-term trends were analyzed. The comparisons of the satellite retrieved products with in-situ data and the model outputs were also conducted. The applications of the thermal hyperspectral sounders to monitor the atmospheric CH_4 changes at the global scale and regional scales, specifically in South America and the Arctic region, were demonstrated. The overarching research objectives of this study are:

- To analyze latitudinal dependences and seasonality dependencies of the methane trends.
- To characterize the spatiotemporal global distribution of atmospheric methane.

- To compare AIRS and CrIS retrievals with the observations from GML in-situ measurements.
- To understand global and regional trends of mid-to-upper tropospheric CH_4 from AIRS and CrIS products.
- To gain insight into changes between the surface and upper troposphere by comparing satellite retrieved CH_4 with in-situ observations and modeling results.
- To demonstrate the quality of the NUCAPS CH_4 products and the ability to monitor global environmental changes.

The specific scientific questions that I seek to answer through my dissertation research are:

- How has atmospheric CH_4 changed with time in the past two decades as observed by AIRS and CrIS?
- Can satellite retrievals be used to compute the rate of change which has only been done by in-situ data in the past?
- How do satellite trends compare with in-situ and why?
- Can CH_4 products be used for the detection of regional variations and trends?

In addition, this dissertation identifies areas for future research including ways to prepare the following datasets to be available to the user community, based on this study and the feedback received from the user community:

- The NUCAPS retrievals of the temperature, moisture, surface and cloud properties, ozone, trace gases with averaging kernels, principal component scores, and outgoing longwave radiation, using the latest, validated sounding algorithms.

- The collocated products (e.g., The Visible Infrared Imaging Radiometer Suite (VIIRS) clouds, surface properties, ice/snow products, active fire, vegetation) and other blended products (e.g., precipitation products).
- The collocated radiosonde observations (RAOB) matchup datasets.
- The collocated model output (e.g., parameters from CAM-CHEM).

1.3 Focused Areas of Studies

In addition to examining the global distribution and variability of atmospheric CH_4, the applications of the CH_4 products to the two selected focus regions were also demonstrated (South America, and the Arctic). These areas experienced significant environmental changes during the past several decades, yet there is a strong need for the remote sensing products due to the lack of ground observations. The Arctic ice and permafrost melting as well as the deforestation of the Amazonia rain forest are considered as the tipping points of climate changes, which means that they could have high impacts and are interconnected across different biophysical systems. This could result in potentially committing the world to long-term irreversible changes (Lenton et al., 2019).

1.3.1 South America

South America is one of the major contributors to global CH_4 emission due to various anthropogenic and natural emission sources of the region. It houses 25 percent of the Earth's forests and arable land, as well as more than 30 percent of the world's water resources. For many countries in the region, a significant proportion of the emissions (between 35 percent and up to 60 percent) come from agricultural, forestry and land use sectors. According to EDGARv4.3.2 South America total CH_4 emission ranks the third in the world, following East Asia and South Asia. South America contributes to more than 12% of the global CH_4 emissions.

Among the countries in South America, Brazil has the highest methane emission level in the region and is one of the world's biggest emitters of CH_4. Brazil's 2018 Biennial Update Report to the United Framework Convention on Climate Change (UNFCCC) states that the majority of these emissions were from agriculture (70% from enteric fermentation, manure management and crop residue burning) with the remainder coming from waste (16%), energy (4%), and land-use change (6%) (Ministry of Foreign Affairs et al., 2019).

Deforestation of the Brazilian Amazon has surged, and more than three-quarters of the Amazon rainforest has been losing resilience since the early 2000s (Boulton et al., 2022). Based on the balance of all natural and human-caused greenhouse gases coming in and out of the Amazon Basin, a recent study found that the region may turn to a net carbon emitter from carbon sink (Covey et al., 2021). The warming of the region, the forest fires, and drying out of seasonally flooded forests, as well as increased human activities such as agriculture, forest loss due to illegal logging, and fossil fuels, has caused the region to release large volumes of CH_4 and nitrous oxide. The projections suggest that a 4°C temperature increase in tropical South American wetlands could double already substantial regional CH_4 emissions (Zhang et al., 2018). There are increasing concerns that the region is rapidly approaching a catastrophic "tipping point" (Boers et al., 2017; Lovejoy and Nobre, 2018).

For this geographical area, the time series of the methane products derived from AIRS was analyzed. The annual maps of each year from 2003 to 2020 were also generated to examine the changes of CH_4 over the region during the past decades.

1.3.2 The Arctic

Arctic ecosystems and communities are increasingly at risk due to continued warming and declining sea ice (Richter-Menge et al., 2019). One of the key findings from the Fourth National

Climate Assessment (NCA4), conducted by U.S. Global Change Research Program (USGCRP, 2017 and 2018) is that the annual average near-surface air temperatures across Alaska and the Arctic have been increasing at a rate more than twice as fast as the rest of the planet over the last 50 years. The 2019 NOAA Arctic Report Card reported a 1.9°C mean annual surface air temperature (SAT) anomaly for October 2018 - September 2019 for land weather stations north of 60°N, relative to the 1981 - 2010 mean. This is the second highest value (after 2015/16) in the observational record starting in 1900 (Fig. 3). Observed annual mean Arctic temperatures over the past six years (2014-19) have all exceeded previous records. Since the mid-1990s the Arctic has warmed at more than twice the magnitude of global mean temperature increases; a phenomenon known as Arctic amplification (Budyko, Sellers, 1969; Manabe, 1975).

Around the same period, a decrease in the sea ice has also been observed in the Arctic region, as reported by the NOAA National Snow & Ice Data Center (NSIDC). Fig. 4 shows monthly ice extent anomalies plotted as a time series of the percentage difference between the extent for a month in question and the mean for that month based on the January 1981 to December

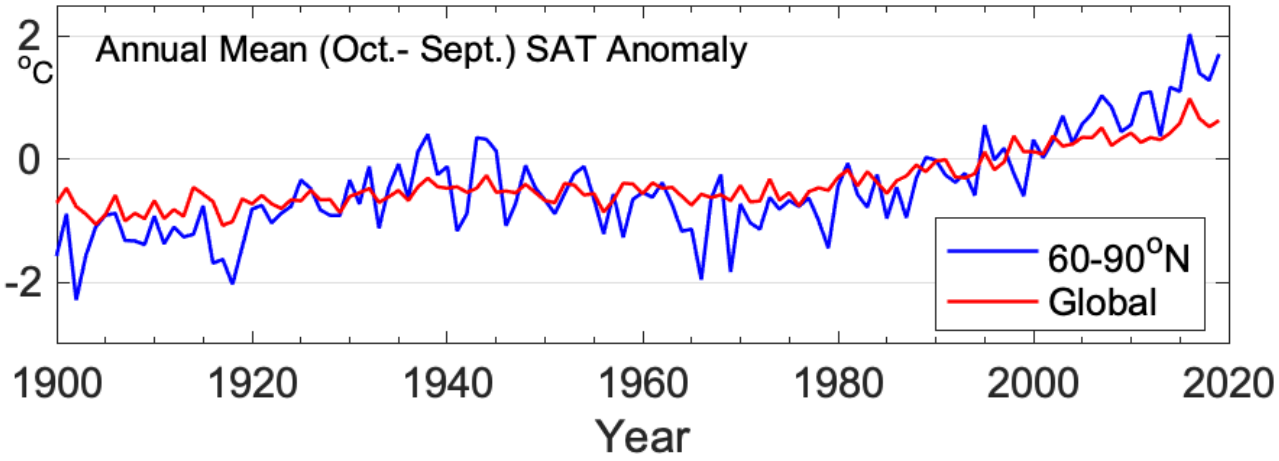

Fig. 3: Arctic (land stations north of 60° N; blue line) and global (red line) mean annual land surface air temperature (SAT) anomalies (in °C) for the period 1900-2019 relative to the 1981-2010 mean value. Note that there were few stations in the Arctic, particularly in northern Canada, before 1940. Source: CRUTEM4 dataset, which is available at www.cru.uea.ac.uk/cru/data/temperature/.

2010 data. The anomalies are plotted as plus sign symbols and the trend is plotted with a dashed gray straight line.

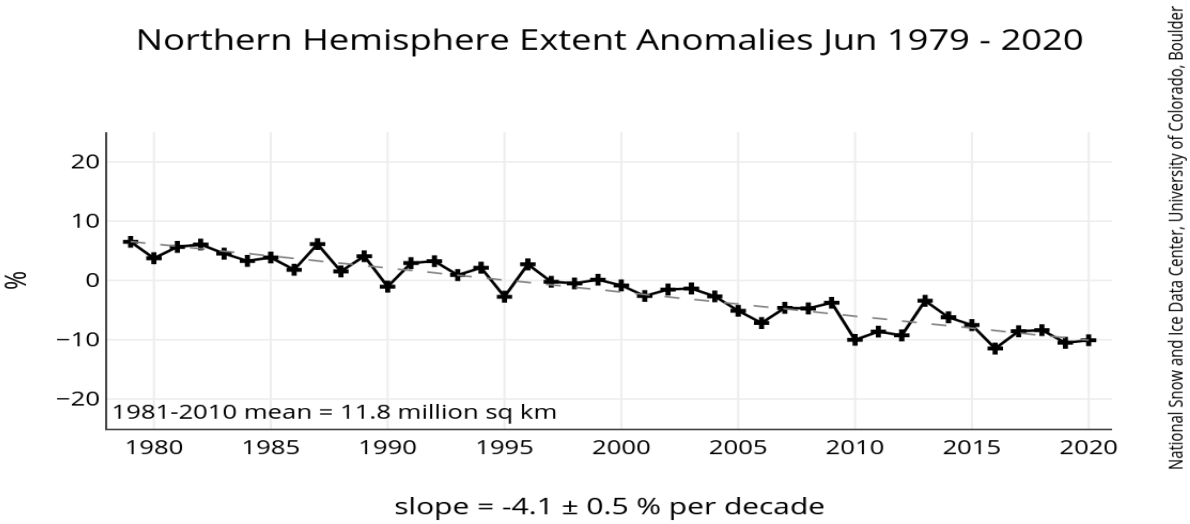

Fig. 4: Monthly Sea Ice Extent Anomaly https://nsidc.org/data/seaice_index/ (Credit: NOAA/NSIDC Team with funding from NOAA and with assistance from the NSIDC NASA GES).

These changes have profound effects on the Arctic environment and communities, such as the loss of ice sheets in Greenland, large increase of incidence of wildfires in the Arctic and sub-Arctic, altered atmosphere and oceanic circulation patterns, ongoing thawing permafrost causing problems for oil pipes, roads and buildings, and the changing ocean ecosystem impacting fisheries as well as the hunting patterns. It is critical to ensure that the changing climate over the Arctic is closely monitored and well understood so that it is possible to help the local communities to mitigate risks in the near future.

Over the Arctic region, polar satellites provide multiple overlapping passes, with high spatial resolution imaging and high vertical resolution sounding information (Goldberg et al., 2018). Over most of the Arctic there are more than 60 overpasses per day, occurring every 20 -30 minutes. The high temporal and spatial coverage of polar satellites provide much needed observations to monitor the Arctic environment.

For this specific geographical region, this study conducted the analysis of the methane products derived from CrIS and AIRS. The results over the Arctic region will be compared with the in-situ observations in the arctic regions.

In this Chapter, the state of global methane emissions, its source and sinks, and the changes in emissions, and the strong need for satellite products to continuously monitor CH_4 for climate and necessary mitigations were reviewed and described. The objective of the study, the scientific questions to be answered, and the selected application areas are explained. The next Chapter describes the measurement approaches, including both the satellite and ground observation networks, and the theoretical bases of the retrieval algorithms and validations. Chapter 3 shows the 20 years of global climatology of CH_4 revealed from hyperspectral infrared sounders. Chapter 4 provides detailed descriptions of the trends and latitudinal changes of the CH_4 products. Chapter 5 demonstrates the results of satellite retrieved CH_4 with a geographical regional focus on, such as South America and the Arctic. Chapter 6 provides a summary and conclusions of this work. Lastly, future study areas are outlined in Chapter 7.

Chapter 2: Data Used and Methodology

2.1 Observations Used in this Study

Measurements of atmospheric CH_4 concentrations and their spatiotemporal variation provide valuable information about CH_4 emissions and removals. Whereas bottom-up inventories provide specific information about known emission sources, top-down methods based on atmospheric measurements provide an integrated constraint on the net amount that is exchanged between the surface and the atmosphere by natural and anthropogenic processes. Accurate atmospheric CH_4 measurements can therefore provide additional information for bottom-up inventories and a complementary approach for assessing nationally determined contributions (NDCs). In this section we will discuss Ground-based (in-situ) observation approaches and Space-based (satellite remote sensing) measurements.

2.1.1 Ground-based Measurements

The NOAA Global Monitoring Laboratory (GML) has measured CH_4 since 1983 at a globally distributed network of air sampling sites (Dlugokencky et al., 1994). The distribution of the network is shown in Fig. 5. These measurements are highly accurate and provide invaluable information for global CH_4 monitoring (WMO 2009, 2011). GML profile observations have been used as the truth for the validation of the NUCAPS CH_4 profile retrievals (Nalli et al. 2020). On the other hand, this network does not provide the spatial coverage needed for those areas that have challenges for physical access due to the environmental or political reasons. The network is particularly sparse in the Tropics, Arctic, and boreal regions and over the ocean, as shown in the map of stations in Fig. 5. In this study, the long-term GML measurements were used in our analysis

of satellite CH_4 for comparison purposes. Since the GML data are observed near the surface and thermal IR retrievals are mostly sensitive to the middle to upper troposphere, direct comparisons are not possible. Nevertheless, the differences between the GML and the satellite retrievals provide insights into vertical contrasts due to transport.

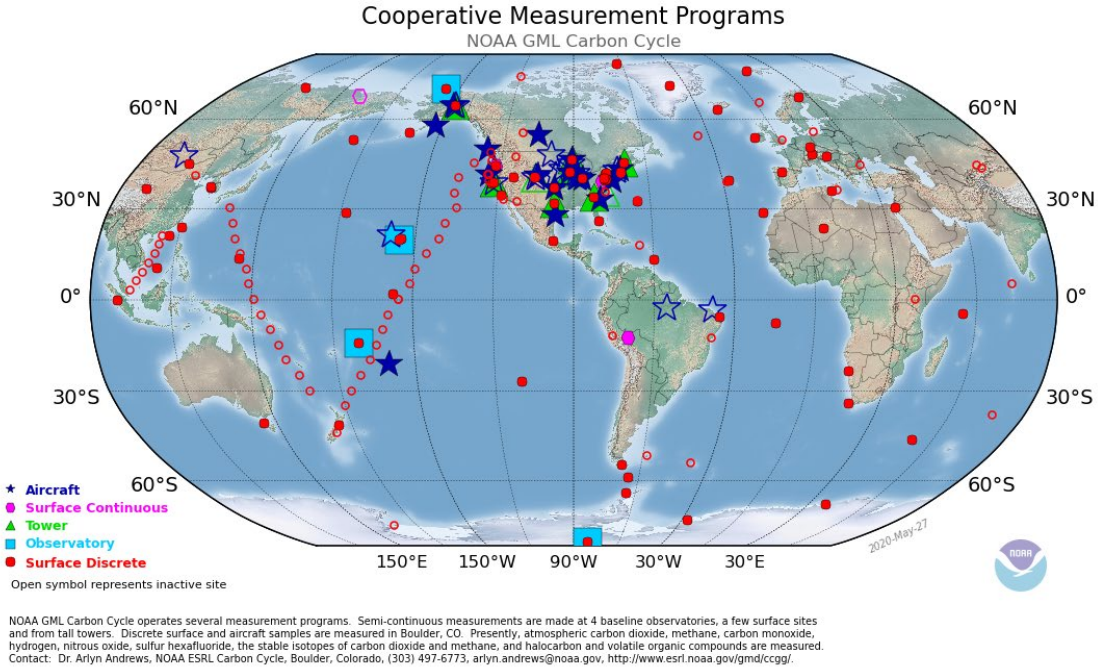

Fig. 5: The distribution of the Global Greenhouse Gas Reference Network, a part of NOAA's Global Monitoring laboratory in Boulder, Colorado. https://gml.noaa.gov/ccgg/about.html

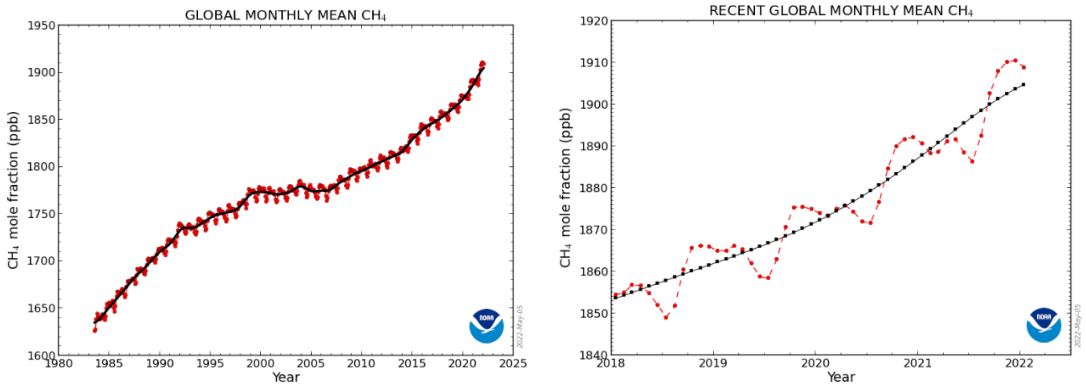

Fig. 6: Globally averaged, monthly mean atmospheric CH_4 abundance determined from marine surface sites. The left graph shows monthly means for the last four years plus the current year, and the right graph shows the full NOAA time-

series starting in 1983. Values for the last year are preliminary, pending recalibrations of standard gases and other quality control steps (Ed Dlugokencky, NOAA/GML, www.esrl.noaa.gov/gmd/ccgg/trends_ch4/).

Figure 6 shows atmospheric CH_4 abundance determined from marine surface sites (http://www.esrl.noaa.gov/gmd/ccgg/trends_ch4/). The red lines with circles are values centered in the middle of each month. The black lines with squares show the long-term trend (in principle, similar to a 12-month running mean) where the average seasonal cycle has been removed. The figure on the left shows the full NOAA time-series starting in 1983, and the graph on the right shows monthly means for the last four years plus the current year. Values for the last year are preliminary, pending recalibrations of standard gases and other quality control steps. After a hiatus in the growth of its atmospheric burden from 1999 to 2006, CH_4 began increasing in 2007, as seen in the right panel of Fig. 13. Renewed growth in globally averaged CH_4 since 2007 was attributed to a combination of increased tropical natural emissions and emissions from fossil fuel production, agriculture, and waste (Saunios, et al 2017, Rigby et al 2017).

2.1.2 Space-based Measurements

The advancements of space-based remote sensing approaches in recent years have provided new opportunities to augment the spatial and temporal resolution and coverage of the ground-based CH_4 measurement network. Satellite remote sensing observations have enabled continuous measurements of CH_4 concentration and distribution in the atmosphere globally. There have been mainly two types of satellite sensors that can provide the CH_4 concentration estimates: 1) Shortwave Infrared (SWIR) instruments and laser approaches measure a total column average from high spectral resolution observations of reflected sunlight; the measurement is a mixture of surface and column atmospheric contribution; and 2) Thermal Infrared (TIR) instruments that measure the radiances emitted from thermal infrared spectral bands that are sensitive to mid-

tropospheric column CH_4. The main characteristics of these two different types of instruments are summarized in the table below and a plot of the averaging kernels is shown in Fig. 7.

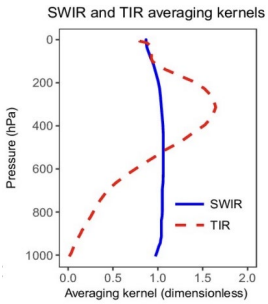

	Passive-Thermal	Passive-Solar	Active
Source Function	Planck Function	Sun	LASER
Measures	Mid-trop column	Total Column	Total Column/Profile
Sampling	Global, Day & Night	Global, Daytime	TBD
Interference	Strong interaction with T(p), q(p)	Weak interaction with T(p), q(p)	Very weak interference
Data availability	20+ years, launch almost guaranteed	Research grade, 2-3 mission, no follow-on	Future missions

Fig. 7: left - sketch of the SWIR and TIR averaging kernels; right - table summarizes the different features of the SWIR vs TIR instruments.

A series of satellite sensors to retrieve atmospheric CH_4 and other GHG concentrations have been launched during the past several decades by space agencies worldwide. The Scanning Imaging Absorption SpectroMeter for Atmospheric CHartographY (SCIAMACHY) onboard the European Space Agency (ESA) ENVISAT (2003–2012), operating in the UV, visible and near infrared spectral regions has delivered annual global distribution of CH_4 (Frankenberg et al., 2011). It was followed by the Thermal and Near-infrared Sensor for carbon Observation (TANSO) onboard Japan Aerospace Exploration Agency (JAXA) / the National Institute for Environmental Studies (NIES) / the Ministry of the Environment (MOE) Greenhouse gases Observing SATellite (GOSAT) which has been in operation since 2009 (Yokota et al., 2009). These pioneering SWIR sensors were recently joined by the Chinese FengYun-3D (FY-3D), launched on November 14, 2017. Greenhouse gases Absorption Spectrometer (GAS) and Gaofen-5 (launched in May 2018) Greenhouse-gases Monitoring instrument (GMI) sensors (Zhang et al., 2020), as well as by the TROPOspheric Monitoring Instrument (TROPOMI) onboard the Copernicus Sentinel-5 Precursor (S5P) satellite launched on October 13, 2017 (Lorente et al., 2021).

2.1.2.1 Hyperspectral Infrared Instruments

In addition to these sensors that utilize the SWIR radiation scattered and absorbed by CH_4, thermal emission spectra from hyperspectral infrared (IR) sounders onboard the polar orbiting environmental satellites can also be used to derive CH_4 concentration with near 7.66 μm absorption band. Hyperspectral IR sounders including the Atmospheric Infrared Sounder (AIRS) onboard the National Aeronautics and Space Administration (NASA) Earth Observing System (EOS)/Aqua (Aumann et al., 2003), the Cross-track Infrared Sounder (CrIS) onboard the Suomi National Polar orbiting Partnership (SNPP) and Joint Polar Satellite System (JPSS)-1 (renamed NOAA-20 after launch) (Goldberg et al., 2013), and the Infrared Atmospheric Sounding Interferometer operating on MetOp satellites (Hilton el al., 2012; Crevoisier et al., 2009, 2013; Razavi et al., 2009). Continuous global CH_4 environmental data records (EDRs) have been generated using these hyperspectral thermal IR sensors for the past two decades. The current operating hyperspectral thermal IR sounders, and planned hyperspectral thermal IR sounders for future, are listed in Table 2 (Crisp et al., 2018).

The accuracy of retrievals from hyperspectral IR sounders have greatly improved in the past several years. For example, the CrIS instrument is Fourier Transform Spectrometers (FTS) instrument with channels in three bands covering longwave IR (LWIR, 655–1095 cm^{-1}), mid-wave IR (MWIR, 1210–1750 cm^{-1}), and shortwave (SWIR (2155–2550 cm^{-1}) bands (Lee et al., 2009). The CrIS instrument instantaneously observes nine fields of- views (FOVs), with each FOV at a spatial resolution of 14 km at nadir, and the Level 2 products are provided in a $3^o \times 3^o$ array known as a Field-of-Regard (FOR). The instrument provides 30 FORs for each scan line of observations. Four scan lines constitute a "granule," and a full day of data contains approximately 2700 granules of CrIS observations. In this work, the CrIS data starting December 4, 2014, is used, when the S-

NPP CrIS instrument was operating in full spectral resolution mode with a spectral resolution of 0.625cm^{-1} in all three bands, and a total of 2211 channels (Zou, et al., 2020). The full spectral resolution coupled with low noise in all three bands enables retrievals of carbon trace gasses including CO, CO_2, CH_4, and other species. Details of these instruments and their channel characteristics have been published previously (Han et al., 2013, 2018; Sanchez et al, 2021).

AIRS is an infrared IR grating spectrometer that has been onboard NASA EOS/Aqua satellite from May 2002 to now (Pagano et al., 2003; Chahine, et al., 2006). AIRS has 2378 spectral channels in the spectral ranges 649 – 1136, 1217 – 1613 and 2169 – 2674 cm^{-1} at a spectral resolution of ~1200 (Aumann et al., 2003), with radiometric accuracy < 0.3°K for a 250°K brightness temperature target (Pagano et al., 2003). AIRS has demonstrated stability at an estimate of ~4 mK/year (Aumann and Pagano, 2008). The recent estimate of the radiometric stability of the AIRS radiances was done by comparing the minor-gas anomalies to the NOAA Global Monitoring Laboratory (GML) in situ measurements. These estimates strongly suggest that many AIRS channels are stable to better than 0.02 to 0.03 K per decade, well below climate trend levels (Strow and DeSouza-Machado, 2020).

IASI has been operating on MetOp satellites since 2007 (Hilton el al., 2012; Crevoisier et al., 2009; Razavi et al., 2009). For IASI, the CH_4 estimates improved to 8 ppb on daily time scales at single sounding resolution (Crevoisier et al., 2018). In recent years, IASI CH_4 products were used to estimate fluxes at monthly intervals at regional to hemispheric scales (Nassar et al., 2011; Cressot et al., 2014). The products were also used in data assimilation experiments to provide CH_4 forecasts in the framework of the Copernicus Atmosphere Monitoring Service (Massart et al., 2014).

The spectral coverage and NEdT noise performance for these hyperspectral infrared sounders are shown in Fig. 8.

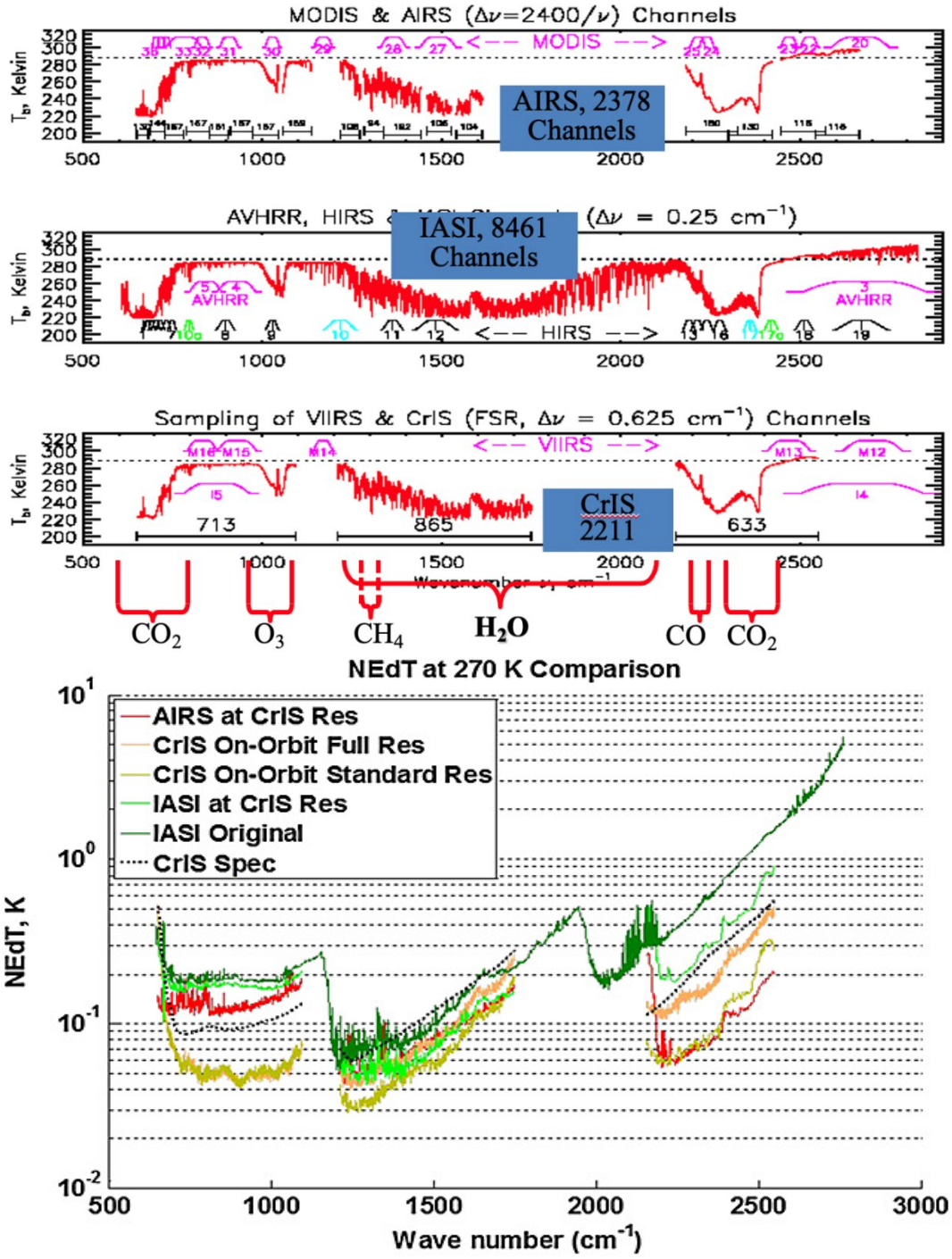

Fig. 8: CrIS Spectral Coverage (top); and NedT performance (bottom). CrIS on-orbit nominal NEdT is compared with AIRS (at CrIS spectral resolution) and IASI NEdT estimated at IASI original and CrIS-like spectral resolution. The black curve depicts CrIS specification requirements. (Zavyalov, et al., 2013)

In this study, we focus on the analyses of the changes and distributions of the CH_4 concentration derived from AIRS and CrIS flown in the same 01:30/13:30 local equator crossing time orbits (i.e., CrIS and AIRS), as shown in Table 2. The AIRS physical retrieval algorithm is currently used as a heritage algorithm for CrIS (with ongoing updates and improvements), hence, providing consistent atmospheric vertical profile products from 2002 to the present. Since CrIS is in the technical baseline for JPSS program satellites, the same hyperspectral products are expected to extend to the JPSS-4 timeframe in the 2040s, therefore, there is a great opportunity to produce long term, continuous data records from these instruments.

Table 2: Current and Planned Hyperspectral Thermal IR Sounders on Operational Meteorological Satellites (Crisp et al., 2018).

Satellite	Instruments	Local Equator Crossing Time	Launch dates	Satellite
Aqua	AIRS	01:30/13:30	2002	Aqua
Metop-A, B, C	IASI	09:30/21:30	2006, 2012, 2018	Metop-A, B, C
SNPP, JPSS-1,2,3,4	CrIS	01:30/13:30	2011, 2017, 2022, 2027, 2032	SNPP, JPSS-1, 2, 3, 4
Metop-SG-A1,2,3	IASI-NG	09:30/21:30	2024, 2031, 2037	Metop-SG-A1, 2, 3

2.1.2.2 Radiative Transfer and Retrieval Equations in the Infrared

The radiances measured by hyperspectral infrared sensors can be separated into the following components: surface radiance, atmospheric radiance, down-welling reflected radiance, and reflected solar radiance (Barnet, 2006). The observed radiance can be expressed as:

$$R_n^{obs} \simeq R_n(\hat{X}) + \epsilon \quad (1)$$

where R_n^{obs} is the measured radiances, and R_n is the forward model calculated radiances. The solution of Eq. (1) (i.e., retrieval equation) can be linearized by the retrieval X_j^i about the 'truth' state X_j^A:

$$\hat{X}_j^i = X_j^A + \left[\hat{K}_{j,n}^T \cdot N_{n,n}^{-1} \cdot \hat{K}_{n,j} + C_{j,j}^{-1}\right]^{-1} \cdot \hat{K}_{j,n}^T \cdot N_{n,n}^{-1} \cdot \left[\epsilon + \hat{K}_{n,j} \cdot \left(\hat{X} - X_j^A\right)\right] \quad (2)$$

$$\hat{K}_{n,j} \equiv \frac{\partial R_n\left(\vec{X}\right)}{\partial X_j}\Big|_{\hat{X}} \simeq K_{n,j} \quad (3)$$

Here $\hat{K}_{n,j}$ is the Jacobian matrix that describes the sensitivity of the forward model calculated radiances to the target variable (e.g., CH_4). $N_{n,n}^{-1}$ is the observational covariance. $C_{j,j}^{-1}$ is the error covariance of the a priori. X is the true state and X^a can be a priori state or the states from the previous retrieval iteration. To simplify it, we replace the term highlighted in the blue frame above with the variable G (the gain matrix):

$$\begin{aligned} \boldsymbol{X}_j^i - \boldsymbol{X}_j^A &= \boldsymbol{G}_{j,n} \cdot \left[\boldsymbol{\epsilon}_n + \boldsymbol{K}_{n,j} \cdot \left(\hat{\boldsymbol{X}} - \boldsymbol{X}_j^A\right)\right] \\ &= \boldsymbol{A}_{j,j} \cdot \left(\hat{\boldsymbol{X}}_j - \boldsymbol{X}_j^A\right) + \boldsymbol{G}_{j,n} \cdot \boldsymbol{\epsilon} \end{aligned} \quad (4)$$

$$\begin{aligned} \boldsymbol{A}_{j,j} &\equiv \boldsymbol{G}_{j,n} \cdot \boldsymbol{K}_{n,j} \\ \boldsymbol{A}_{j,j} &\equiv \left[\boldsymbol{K}_{j,n}^T \cdot \boldsymbol{N}_{n,n}^{-1} \cdot \boldsymbol{K}_{n,j} + \boldsymbol{C}_{j,j}^{-1}\right]^{-1} \cdot \boldsymbol{K}_{j,n}^T \cdot \boldsymbol{N}_{n,n}^{-1} \cdot \boldsymbol{K}_{n,j} \end{aligned} \quad (5)$$

The averaging kernel ($A_{j,j}$) is a linear representation of the vertical weighting of retrievals (Backus and Gilbert 1970, Conrath 1972). It represents the sensitivity of the retrieved variable to its true state and is related to the amount of information determined from the radiances vs. from a priori or first guess. Then I-A is the amount that came from the a priori:

$$\boldsymbol{I_{j,j} - A_{j,j} = \left[K^{T}_{j,n} \cdot N^{-1}_{n,n} \cdot K_{n,j} + C^{-1}_{j,j}\right]^{-1} \cdot C^{-1}_{j,j}} \quad (6)$$

Where $I_{j,j}$ represent the identity matrix. The closer the matrix A is to the identify matrix I, the better the retrieved state represents the true state. Certain components of the equation, e.g., a priori, Jacobian, and averaging kernels, will be discussed later in this chapter. **Jaco**

2.2 The NOAA Unique Combined Atmospheric Processing System (NUCAPS)

Susskind et al. (2003) describe the AIRS science team retrieval algorithm, which includes calibration, microwave retrieval, cloud-clearing, initial first guess IR retrieval, and a final IR physical retrieval. The cloud-clearing step uniquely allows the physical retrieval algorithm to retrieve profiles under clear and partially cloudy conditions. Continuous validation and improvements of AIRS retrievals have been described by Fetzer et al. (2003), Tobin et al. (2006), Divakarla et al. (2006), Chahine et al. (2006), Susskind et al. (2011). Due to the AMSU-A2 instrument failure, AIRS products using both IR and microwave stopped after September 24th, 2016. Thus, for a consistent data record, we use exclusively AIRS Version 7 thermal IR-only retrievals for the entire record from NASA at Goddard Earth Sciences (GES) Data and Information Services Center (DISC) (https://disc.gsfc.nasa.gov) (Yue et al., 2020).

2.2.1 NUCAPS Algorithms

The NOAA Unique Combined Atmospheric Processing System (NUCAPS) uses CrIS observations combined with ATMS to derive sounding products (Gambacorta et al., 2012, 2013, 2014; Smith and Barnet, 2019; Kalluri et al., 2020; Warner et al., 2022). NUCAPS system follows the AIRS science team algorithm (Susskind et al., 2003, 2011) and emerged as a sensor-agnostic enterprise system leveraging experiences from many contributors across different agencies. The enterprise nature of the NUCAPS framework allows running the code for different hyper-spectral and microwave combinations of radiances. The NUCAPS algorithm is operationally generating products, such as temperature, water vapor, ozone sounding, OLR, and trace gas products (CO, CH_4, and CO_2, see Table 3 for the full list) from SNPP and NOAA-20. The NUCAPS data products are available to the public through The NOAA Comprehensive Large Array-data Stewardship System (CLASS, https://www.avl.class.noaa.gov/saa/products/welcome). The NUCAPS algorithm has been adapted as an enterprise solution to work on CrIS/ATMS, AIRS/AMSU-A, and IASI/AMSU-A/B) instruments.

The NUCAPS retrieval algorithm is composed of the following steps:

1). A microwave retrieval module (MIT maximum likelihood algorithm) which computes Temperature, water vapor, cloud liquid water, and microwave surface emissivity uncertainty (Rosenkranz, 2000).

2). A fast eigenvector statistical regression retrieval computes temperature and water vapor, which is trained against ECMWF and all sky (cloudy) radiances (Goldberg et al., 2003).

3). A cloud clearing module that uses a set of microwave and IR channels to produce the cloud-cleared IR radiance product and reject those cases violating the cloud-clearing requirements (Chahine, 1974).

4). A second fast eigenvector regression retrieval that is trained against ECMWF analysis and cloud cleared radiances (Goldberg et al., 2003).

5). The final infrared physical retrieval that uses an iterated regularized least squared minimization. We start with the temperature retrieval, because it is the most linear component of the RTA equation, followed by water vapor, O_3, CO, CH_4, CO_2, SO_2, HNO_3, N_2O, etc. (Susskind, et. al., 2003).

Whereas the NUCAPS was designed to run for different infrared sounders, there are differences between the AIRS and the CrIS level 2 algorithms arising from specific differences in the two instrument characteristics. These differences involve the following modules:

- Rapid Transmittance Algorithm (RTA)
- Regression coefficient set
- Microwave and Infrared tuning coefficients
- Modeling of RTA noise
- Cloud coefficient table
- Channel selection for the core and trace gas retrieval
- A priori
- Quality flags

These differences need to be considered when compare the products derived from AIRS and CrIS.

The NUCAPS products have gone through a thorough validation process (Zhou et al., 2016, 2019; Nalli et al., 2018a, 2018b, 2020). The temperature, moisture, ozone, OLR, CO, and CH_4 products have all passed the validated maturity by April 2020, which means that the products have been fully validated and met the requirements seasonally and globally. For the carbon trace

gases from AIRS, IASI, and CrIS, even though these products have been generated from NUCAPS in operation and made available to the public for the past decade, this is the first time that NOAA operational trace gases products reached this stage of the validation maturity.

Before reaching the validated maturity in April 2020, the trace gas products were generated from an older version of the NUCAPS algorithms that were problematic for CH_4. Although the NOAA marked certain products as un-validated on its website, the un-validated CH_4 products were still being used in many conference presentations and publications. The premature results shown from these studies could mislead the public that the catastrophic climate changes were already happening due to a drastic CH_4 increase in the Arctic regions, which differs from the results analyzed by the NOAA's Global Greenhouse Gas Reference Network (GGGRN) ground observations (http://www.esrl.noaa.gov/gmd/ccgg/) (Bergamaschi et al., 2013; Bruhwiler et al., 2014; Sweeney, 2019). Studies from NOAA GML ground measurements reported no abnormal increase in the rate of methane emission in the Arctic. The uses of the premature retrieval results generated serious concerns from the community about NOAA satellite carbon products. During the past few years, the NUCAPS science team focused on these issues while working with the science community and the users to address the algorithms and validation in the arctic region (Warner et al., 2022). With the improved algorithms, quality control, and validation, it is now a better time to start utilizing the improved trace gas products to analyze the environmental changes and gain better understanding of the spatiotemporal variabilities of the CH_4 concentrations.

Table 3: Spectral ranges, precision, and sensitivity of the NUCAPS retrievals of trace gases. (Alvarado et al., 2015).

	Spectral Range (cm^{-1})	Retrieval Precision	d.o.f.	Interfering Signals	Sensitivity
H_2O	1200-1600	15%	4-6	CH_4, HNO_3	Surf. to 300 mb
O_3	1025-1050	10%	1+	H_2O, surface emissivity	Lower strat.
CO	2080-2200	15%	≈ 1	H_2O, N_2O	Mid-trop
CH_4	1250-1370	1.5%	≈ 1	H_2O, HNO_3, N_2O	Mid-trop
CO_2	680-795	0.5%	≈ 1	H_2O, O_3	Mid-trop
	2375-2395			T(p)	
Volcanic SO_2	1340-1380	50% ??	< 1	H_2O, HNO_3	Detection Flag
HNO_3	860-920	50% ??	< 1	emissivity	Upper trop
	1320-1330			H_2O, CH_4, N_2O	
N_2O	1250-1315	5% ??	< 1	H_2O	Mid-trop
	2180-2250			H_2O, CO	

2.2.2 CH_4 Sensitivities of Hyperspectral Infrared Sensors and Retrievals

To retrieve the atmospheric trace gases, it requires unprecedented instrument specifications. First, it requires large spectral coverage with high resolution to increase the number of unique information to remove the cloud and aerosol effects, and allow simultaneous retrievals of temperature, moisture, ozone, and trace gas profiles. AIRS has 2378 spectral channels; CrIS full spectral resolution has 2211 channels; and IASI has 8461 channels, all requiring excellent noise performance. These instruments are well calibrated sensors with very low NEdT, as shown in Fig. 8.

AIRS, IASI, and CrIS retrieval algorithms use the channels near 7.66 micrometer to retrieve the atmospheric CH_4. The choice of these CH_4 channels is based on their kernel functions

and the sensitivity to CH_4. To reduce the interference from other atmospheric compositions, the channels overlapping with absorptions by other species, e.g., water vapor and HNO_3, are minimized. Fig. 9 shows the channel sensitivities near CH_4 spectral bands perturbed to 5% CH_4, along with perturbations of water vapor and N_2O for a given trace gases profile. Here, red stars are CrIS channels, and circle ones are the AIRS channels, used for CH_4 retrievals. It is important to select channels with highest information content and lowest noise and with least interference by other species.

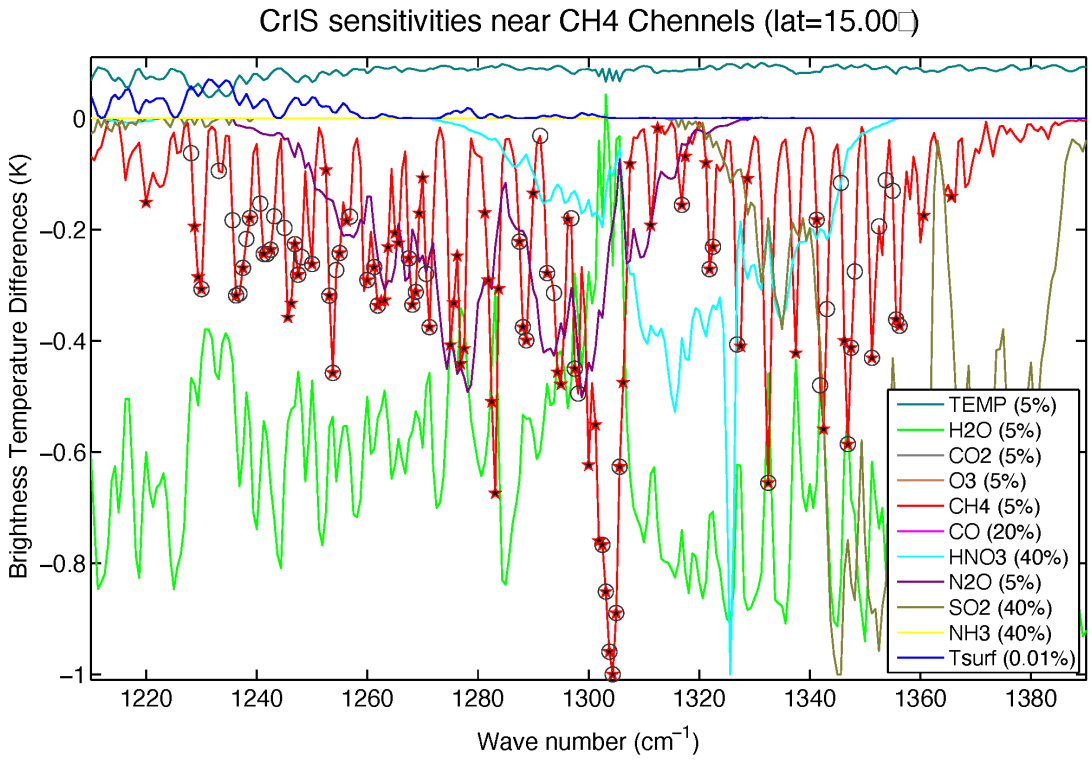

Fig. 9: Channel sensitivities near CH_4 Channels using the standard atmospheric profile for 15° latitude

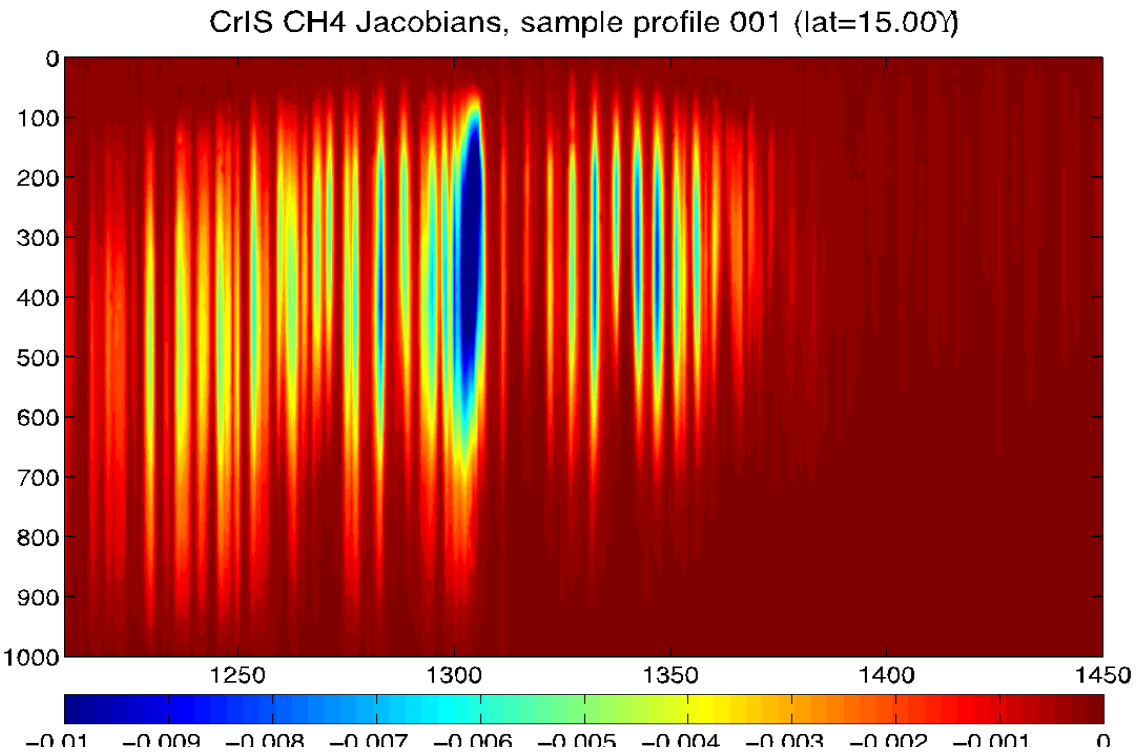

Fig. 10: CH_4 Jacobians for CrIS using the standard atmospheric profile for 15° latitude (Credit: Juying Warner/NUCAPS, UMD/ESSIC).

The CH_4 weighting function, or Jacobian matrix, K, as introduced in section 2.1.2.2, describes the portion of the CH_4 profile represented by each radiance measurement (Rodgers, 1976). Fig. 10 shows an example of the CrIS CH_4 Jacobian matrix calculated with the fast forward model, i.e., Standalone AIRS Radiative Transfer Algorithm (SARTA, see algorithm description in Strow et al., 2003), using the standard atmospheric profile for 15° latitude. The most CH_4 sensitive region for hyperspectral thermal IR sounders, depicted in the non-red color shades, is in the middle

and upper troposphere (i.e., ~200 - 600 hPa), and the peak of the sensitivity can be higher or lower depending on the local scenario of CH_4 profiles.

The NUCAPS retrieval sensitivity to state profile parameters (e.g., trace gas concentration) can be inferred from the retrieval Averaging Kernels (AKs) (Conrath, 1972; Rodgers, 1990; Maddy and Barnet, 2008). Averaging Kernels are linear representations of the vertical weighting of retrievals that explain where and how much of the observed information contributes to each retrieval level (Rodgers, 1976). Fig. 11 shows zonal-mean NUCAPS effective AKs for different latitude bands: 90-60°S (top left); 60-30°S (top middle); 30-0° (top right); 60-90°N (lower left); 30-60°N (lower middle), and 0-30°N (lower right). The averaging kernels of thermal sensors are broad and exhibit significant overlap, indicating that the retrieved amounts of CH_4 at different layers are not independent. The peaks of the CH_4 AKs are centered from about 400 hPa in the mid- to high- latitude zones, to 150 hPa in the tropical zones. Both Figs. 10 and 11 show that the CH_4

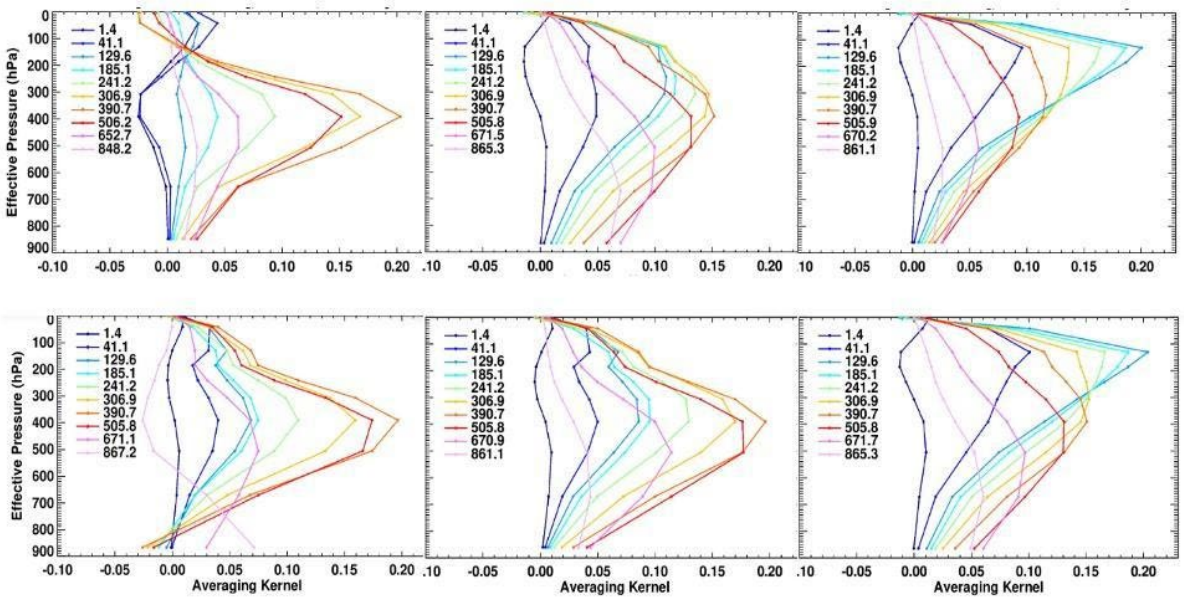

Fig. 11: CH_4 averaging kernel for different latitude bands. (upper left) 90 - 60°S (upper middle) 60 - 30°S (upper right) 30 - 0° (lower left) 60 - 90°N (lower middle) 30-60°N (lower right) 0-30°N.

sensitivities are in the free troposphere and these thermal sensors are not sensitive to CH_4 in the lower troposphere, i.e., below 650 hPa.

Before the CH_4 is retrieved in the retrieval system, the atmospheric temperature profiles, water profiles, surface temperatures and emissivity were retrieved using different channels. This data, as well as the first guess profiles of CH_4, are used as inputs into the fast forward model – SARTA, to compute the radiance for the CH_4 channels. The differences between the observed radiances and the computed radiances are minimized to construct an error covariance matrix, from which the change of CH_4 (δCH_4) is derived using an eigenvector transformation and damping. The final profile of CH_4 is usually obtained through several iterations. See Susskind et al. (2003) for the details of AIRS retrieval method, see Warner et al. (2022) and Xiong et al. (2008) for the details of the CH_4 first guess and channel selections.

2.3 Improvements of the NUCAPS CH_4 Products with CrIS

The same retrieval methodology in NUCAPS has been applied to the AIRS, IASI, and CrIS hyperspectral sounding instruments, and hence, produce consistent observational data records from 2002 to the present, and is expected to extend to 2040 timeframes. The retrieval methodology for CrIS and IASI is also described in detail in the NUCAPS Algorithm Theoretical Basis Document (ATBD) (2021).

For the CH_4 retrievals from SNPP and NOAA-20 CrIS, the products went through a rigid validation process, as described by Nalli et al. (2020). The retrieval algorithms have been improved throughout the validation process. The major changes to improve the CH_4 retrievals include the updates of the CH_4/N_2O a priori, the quality control updates for CH_4 products, and the refinements of the CH_4 channel selection, etc. There were also other NUCAPS algorithm improvements, such

as the updated microwave a priori, and the IR tuning, which advanced the performance of the overall NUCAPS retrievals that impacted positively to the CH_4 products.

In the AIRS Version 7 retrieval, the 100-layer CH_4 prior profile is a function of latitude and altitude that varies smoothly from NH to SH. There is no temporal or longitudinal variation. An analytical function was derived via a non-linear polynomial fit to in situ aircraft measurements and model data (Xiong, et al., 2008). The CrIS a priori profiles are based on in situ measurements from HIAPER Pole-to-Pole Observations (HIPPO, 2009 - 2011, Wofsy et al., 2017) and Atmospheric Tomography Mission (Atom, 2016 - 2018, Wofsy et al., 2018) field campaigns (see NUCAPS ATBD; and Warner et al., 2022). The AIRS a priori profiles only used HIPPO measurements. Latitudinal variations are included in the methane a-priori but do not contain any seasonal or interannual variability. Fig. 12 shows the CH_4 a priori difference between AIRS and

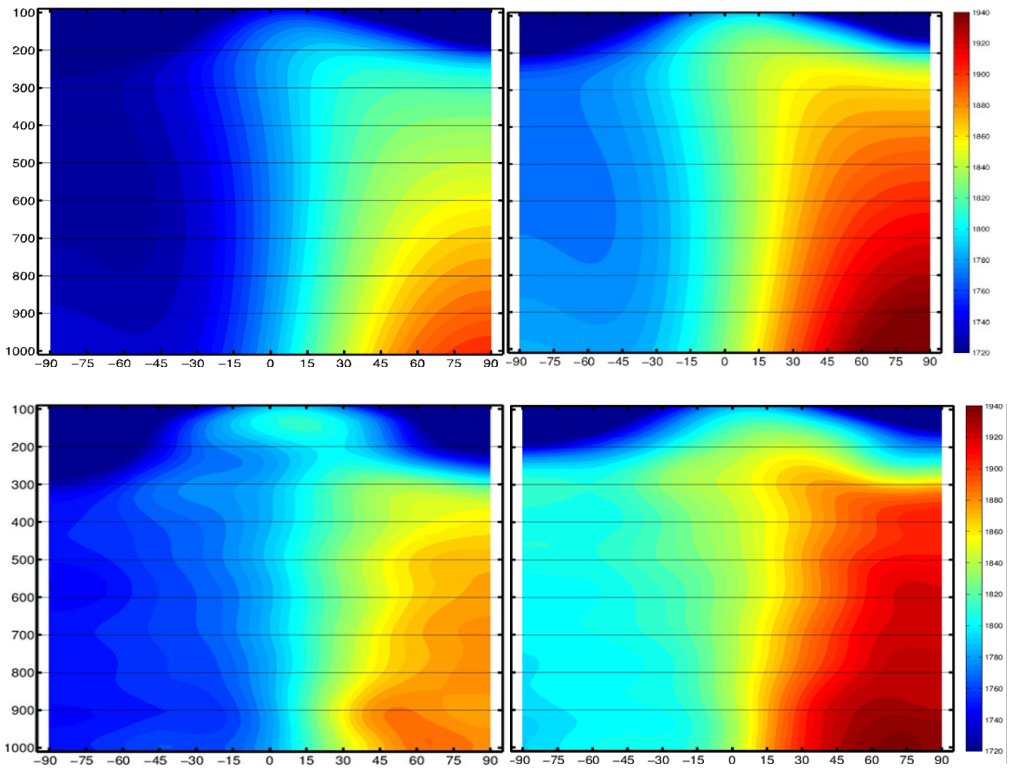

Fig. 12: The updated NUCAPS CH_4 a priori for SNPP CrIS (upper right), which is based on ATom (2016 - 2018) (lower right), in comparison with the a priori for AIRS (upper left), which is based on HIPPO (2009 - 2011) (lower left).

CrIS. AIRS CH_4 a priori represent the HIPPO timeframe, while CrIS CH_4 a priori is improved with updated measurements from Atom. Note that static a priori is used for both AIRS V7 and CrIS, therefore, the trending derived from the products are not from a priori but from the measurements (Warner et al., 2022).

2.4 NUCAPS CH_4 Retrieval Validation

2.4.1 Global Validation Using the Truth Data Sets

A detailed description of the validation approaches and results for the JPSS data products are published in Zhou et al. 2019 (Appendix B) and Nalli et al. (2020). Whereas the same retrieval methodology has been applied to the AIRS, IASI, and CrIS hyperspectral sounding instruments, the NUCAPS CrIS CH_4 products have been fully validated by performing cross-validation with the CH_4 products from different sensors, and aircraft campaigns such as the Total Carbon Column Observing Network (TCCON). In this study we would leverage any existing validation efforts.

2.4.2 Intercomparisons of CH_4 retrieved between satellites:

Performing intercomparisons of the CH_4 retrievals with those from other platforms (e.g., Aqua/AIRS and S5P/TROPOMI) helps to demonstrate the NUCAPS products quality and consistency with other sensors. Fig. 13 shows the monthly-mean column averaged CH_4 (xCH_4 = total column / dry air column) retrieved from CrIS onboard SNPP (top left) and NOAA-20 (top right), AIRS (bottom left), and TROPOMI (bottom right) for August 2018. Note that TROPOMI shows higher CH_4 owing to its true column measurements using solar radiation that includes the lower atmosphere CH_4 contributions, while the hyperspectral thermal sensors are mostly sensitive to the middle to upper troposphere CH_4. Also note that TROPOMI product is for land only. Jointly studying CrIS CH_4 retrievals with those of TROPOMI will reveal lower tropospheric CH_4 closer

to the emission sources. However, the polar coverage in TROPOMI is relatively low due to the limited time when solar radiation is available. Another way to validate the retrieval is to examine the vertical structure of CH_4, as shown in Fig. 14. The upper panel of Fig. 14 shows CH_4 curtain plots of measurements from four Atom aircraft campaigns taken during four different time periods, the lower panels are the corresponding SNPP CrIS zonal mean retrievals. It shows that the CrIS retrieved CH_4 is in good agreement with the Atom aircraft measurements.

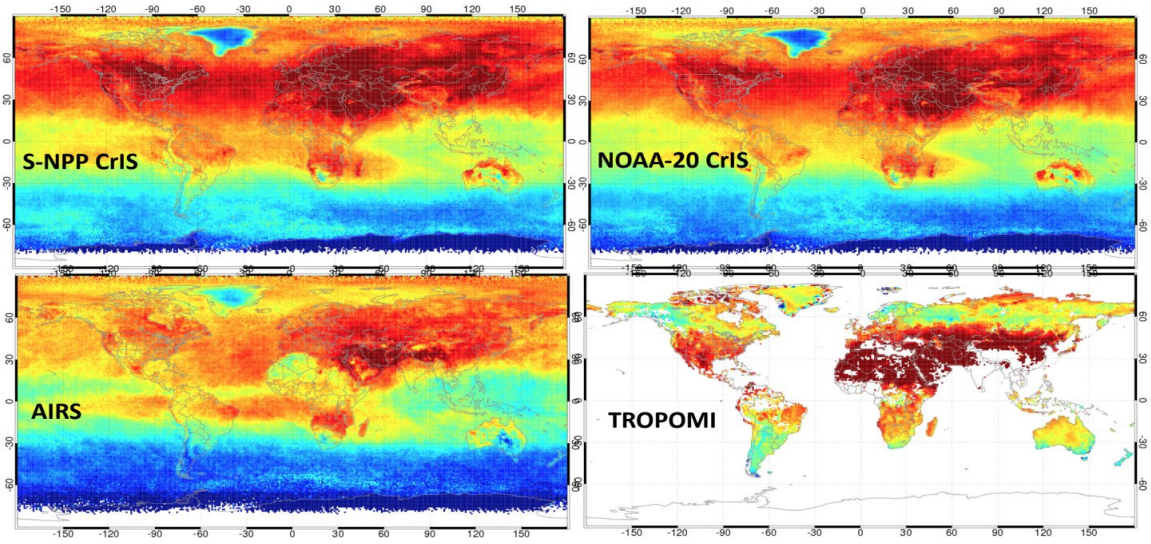

Fig. 13: NUCAPS xCH₄ v2.7.2 Compared to AIRS and TROPOMI August 2018 Monthly Mean. CrIS CH₄ is slightly higher than AIRS; but agrees with TROPOMI mid- and low- latitudes better. (Credit: Juying Warner/NUCAPS, UMD/ESSIC)

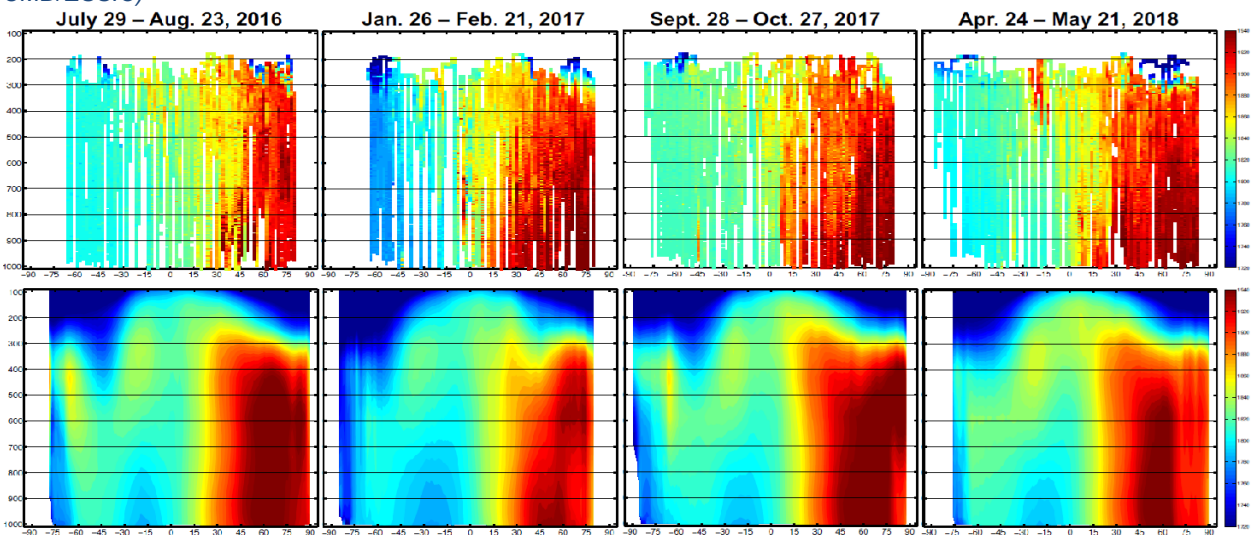

Fig. 14: NUCAPS SNPP Zonal Mean CH₄ Retrievals (lower panel) against ATom1–4 Curtains (upper panel)

2.5 Summary and Conclusions

Chapter 2 described the measurement approaches of atmospheric CH_4, including both the ground measurements and the satellite measurements. The hyperspectral sounders (e.g., AIRS, and CrIS), their sensitivities to atmospheric CH_4, and the analysis of the weighting functions and averaging kernel functions were also introduced. The chapter further demonstrated the corresponding retrieval algorithms and the NUCAPS processing system and the upgrades done for CrIS full spectral resolution observations. In addition, chapter 2 summarized the validation results of the NUCAPS, specifically the results for atmospheric CH_4 retrievals in comparison to the retrievals from other satellites and the in-situ observations. Based on the analysis presented in this chapter, it is concluded that the hyperspectral infrared sounders are sensitive to the atmospheric CH_4 in the middle to upper troposphere. The NUCAPS system has been updated for CrIS observations. The accuracy and precision of the CH_4 products have been validated and more details can be found in multiple published papers (Zhou et al., 2019, Nalli et. al., 2020, Kalluri et al., 2022, Warner et al., 2022).

Chapter 3: Global Distribution of CH_4 and Their Seasonal Variations Observed from Hyperspectral Infrared Sounders

3.1 Global distribution of CH_4

The atmospheric CH_4 time series from 18-years (2003-2020) of AIRS Version 7 retrievals (Kahn et al., 2014; Susskind et al., 2014; Worden et al., 2017; Ding et al., 2020) were analyzed in this study. Fig. 15 shows annual mean global maps of CH_4 at 400 hPa of 2003 and 2020, respectively. The maps show common characteristics of the global CH_4 concentrations, such as higher values over the northern hemisphere (NH) compared to the southern hemisphere (SH), the transported plumes from biomass burning over Africa and South America, and rice field emissions over Asia. For the SH, due to the lack of source of emissions, the patterns of the distribution are mostly determined by the transport, and OH distribution, which depends on solar irradiance, temperature, and moisture, etc. (Lelieveld et al., 2016). Global CH_4 concentrations increased significantly from 2003 to 2020, with the annual average in 2003 at ~1754 parts per billion by volume (ppbv), and ~1839 ppbv in 2020. The total increase during this time period was approximately 85 ppbv which represents a ~4.8% increase from 2003 to 2020. For the same timeframe, the observed annual average of CH_4 concentrations from the GML ground observations

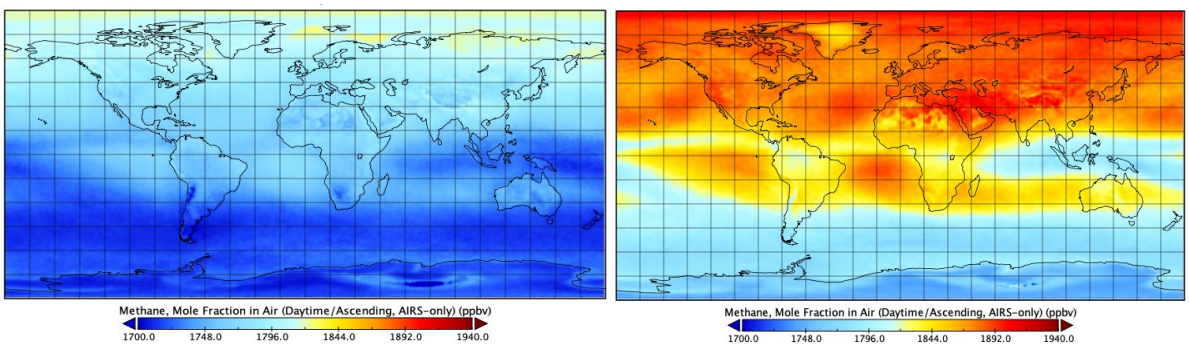

Fig. 15: Annual mean AIRS retrieved atmospheric CH_4 at 400 hPb from the years of 2003 (left) and 2020 (right), plotted using the same color scale (Data processed and downloaded from NASA GES Giovanni, and plotted with Panoply).

is ~1777ppbv in 2003, and ~1879 ppbv in 2020 which is roughly a 5.7% increase. The CH_4 concentrations at the 400 hPa layer from satellites are lower than those from GML measurements. This is expected, due to the GML measurements being closer to the surface where the emission sources are located.

3.2 CH_4 Seasonality Variation

The measurements from AIRS, IASI, and CrIS have provided global continuous CH_4 concentration since 2002 and monitor 3-dimensional spatial and time variations. Fig. 16 shows maps of global seasonal climatology for 300 hPa CH_4 derived from AIRS V7 retrievals, for the period from 2002 to 2020. It shows that the retrieved CH_4 captured strong seasonal variation, especially in the NH. The CH_4 concentration is overall higher in the NH. It is relatively lower in the springtime (global mean 1815.8 ppbv), rises in the summer (global mean 1824.9 ppbv), reaches the highest in the fall (global mean 1839.6 ppbv), and decreases in the winter season (1822.8 ppbv).

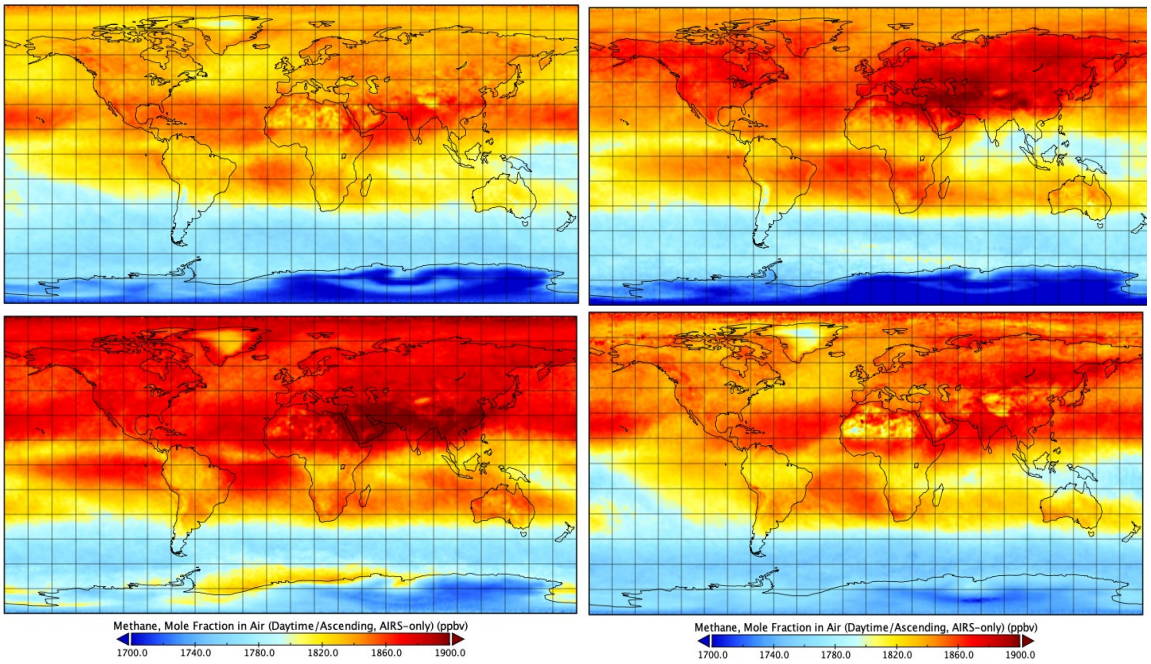

Fig. 16: CH_4 climatology averaged from AIRS from Sept 2002 to Apr 2020 at 300 hPa for Spring (March, April, May, at upper left), Summer (June, July, August, at upper right), Fall (September, October, November, at lower left), and Winter (December, January, February, at lower right). (Data processed and downloaded from NASA GES Giovanni, and plotted with Panoply).

The time series of CH_4 in Fig. 17 shows the changes of CH_4 at 300 hPa over the period from September 2003 to April 2020, for different latitudes. The CH_4 retrieval results demonstrated that there is a strong annual cycle, and overall, the CH_4 concentration at this level has been increasing across all latitudes. The increase is especially strong in the NH and reached highest over the north pole regions. Moreover, Fig. 17 shows that not only have the CH_4 amounts been increasing globally, but also the band of higher CH_4 values has been extended to be broader, from higher latitudes toward lower latitudes and even extended to the southern hemisphere. The global average of CH_4 for different altitudes shown in Fig. 17 right panel, which further reveals that the increase of higher CH_4 values in the past decades extends from the surface extends to higher altitudes.

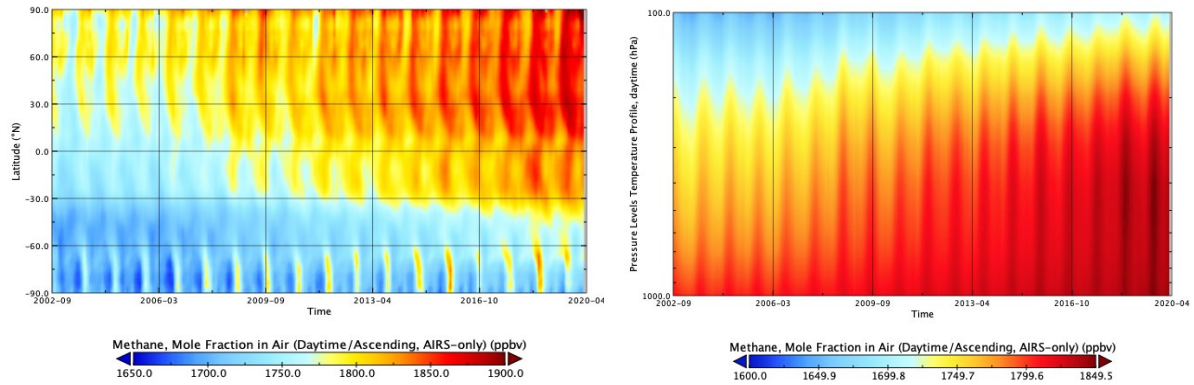

Fig. 17: CH_4 climatology derived from AIRS at 300 hPb over time and for different latitudes (left), and along the altitudes (right). (Data processed and downloaded from NASA GES Giovanni and plotted with Panoply).

Figure 18 shows the changes of CH_4 along with latitude for different pressure levels for 2003 - 2007 (upper left), 2008 - 2012 (upper right), 2013 - 2017 (lower left), and 2018 - 2022 (lower right, only until Mar 2022 due to data availability), respectively. All four plots show the concentrations of CH_4 decrease with height both in troposphere and stratosphere. The decreases with altitudes are much greater in the NH than the SH. In the SH the CH4 concentrations are almost constant throughout the troposphere. While in the SH, the CH_4 concentrations decrease from the

surface to the stratosphere uniformly, in more recent years (2013 - 2017, and 2018 - 2022) though, over the SH sub-tropic region, the CH_4 in mid- to upper troposphere showed higher values than those in the lower troposphere. The amounts of the last few years are in general higher than those from 2003 - 2007, especially for the lower to middle troposphere in the high latitudes of the NH.

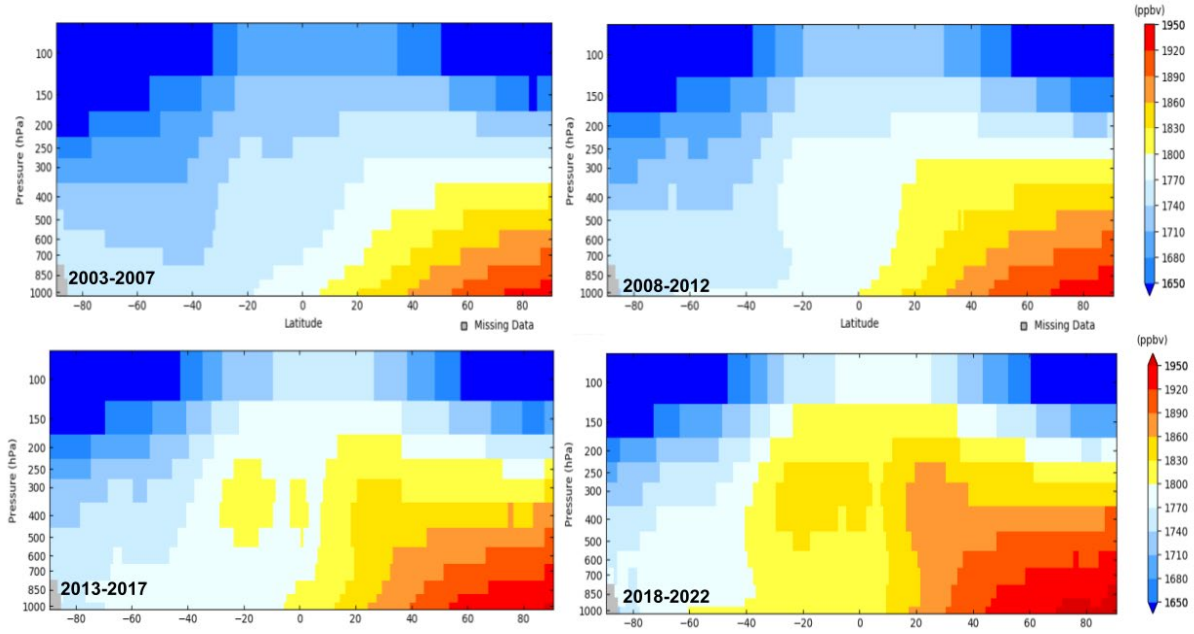

Fig. 18: Changes of CH4 along with latitude for different pressure levels, for the years of 2003 - 2007 (upper left), 2008 - 2012 (upper right), 2013 - 2017 (lower left), and 2018 - 2022 (lower right, till March 2022 due to data availability), respectively. (Data processed and downloaded from NASA GES Giovanni and plotted with Panoply).

3.3 Rate of Changes of CH_4 Concentration

The global mean growth rate of CH_4 concentration in the atmosphere is an important quantity that has been changing over the last three decades (Dlugokencky et al., 2003). The global CH_4 growth rate based on GML in situ measurements was 11.9 ± 0.9 ppbv yr^{-1} during 1984 to 1989. It declined to 6.8 ± 4.2 ppbv yr^{-1} during 1990 to 1998, and then reached a nearly constant state (0.5 ± 3.3 ppbv yr^{-1}) during 1999 to 2005 (Dlugokencky et al., 2009; Steele et al., 1992, Chandra et al., 2021). A renewed and strong CH_4 growth that began in 2007 has also been reported

from assessments using the in-situ measurements (Nisbet et al., 2016, 2019, 2020). The CH_4 growth rate resumed to 6.4 ± 2.9 ppbv yr^{-1} from 2008 to 2014, and further increased to 9.7 ± 3.3 ppbv yr^{-1} from 2015 to 2020 (Nisbet et al., 2019). The annual CH_4 increases in 2020 was 15.85 ± 0.47 ppbv yr^{-1} (https://gml.noaa.gov/ccgg/trends_CH4/), the largest annual increase recorded since 1983 when NOAA's ongoing measurements first began (Butler and Montzka, 2021).

We attempted to examine the same quantity above using global satellite measurements spanning the last several decades. We followed the fitting methods of Nisbet et al. (2016) as shown below:

The monthly averaged CH_4 at each latitude formed a time series. The time series is then fitted with a 2nd degree of polynomial and 4 periods of sine and cosine series,

$$y(t) = y_p(t) + y_s(t) + \mathrm{E}(t) \tag{7}$$

where $t = \frac{month-0.5}{12} + year$ represents middle point in each month. $y_p(t)$ represents trend signal

$$y_p(t) = p_0 + p_1 t + p_2 t^2 \tag{8}$$

and $y_s(t)$ represents seasonal signals,

$$y_s(t) = \sum_{k=1}^{4} [A_k \sin(2\pi kt) + B_k \cos(2\pi kt)] \tag{9}$$

K=1, 2, 3, 4 represents the 1-year, 1/2-year, 1/3-year and 1/4-year periods. $\mathrm{E}(t)$ represents the fitting residuals, it will be filtered by a low pass filter, i.e., at roughly 2 years,

$$\mathrm{E}(t) = \mathrm{E}_{low}(t) + \varepsilon \tag{10}$$

where $\mathrm{E}_{low}(t)$ denoted the signal passed by low band filter, and ε was the high frequency noise. y_p came with the $\mathrm{E}_{low}(t)$ to form the non-seasonal portion of CH_4 monthly mean, i.e.

$$y_n(t) = y_p(t) + \mathrm{E}_{low}(t) \tag{11}$$

Then the annual CH_4 rate at each month can be calculated,

$$R(t) = \frac{dy_n(t)}{dt} = \frac{dy_p(t) + d\mathrm{E}_{low}(t)}{dt} \tag{12}$$

The CH_4 latitudinal distributions with time are shown in the upper panels of Fig. 22 where the top left panel shows AIRS measurements, and the top right panel is the same measurements but fit through modeling, as described above. As shows in Fig. 19, the fitted values represent the measurements very well. While globally the CH_4 increased at all latitudes, stronger increases were observed in the NH in the earlier years. From 2008, higher values, i.e., over 1800 ppbv, are seen in the SH and the Arctic region.

The lower panels of Fig. 19 show the rate of change calculated from AIRS and CrIS observations with the bottom left as the de-seasoned growth rate of AIRS, and the bottom right is the de-seasoned growth rate of CrIS. The rate of change from AIRS also demonstrated the overall increase of CH_4 after 2008, especially the higher values have been expended toward the SH and polar region. The results from CrIS are for 2015 to 2020 showing overall agreement with results from AIRS for the same period.

Since it takes approximately one year for CH4 mixed from surface throughout the troposphere (Dlugokencky et al., 2011), the years with strong regional growth usually followed by declines to the global background (Dlugokencky et al., 2011, 1994; Nisbet et al., 2016). This pattern can be seen clearly from the early 2000s. After 2014, the period of decline became less well defined and more dominant as seen by the overall positive increase rates. The results in this study are also generally consistent with those derived from the in-situ measurements (Nisbet et al., 2019, Lan et al., 2021).

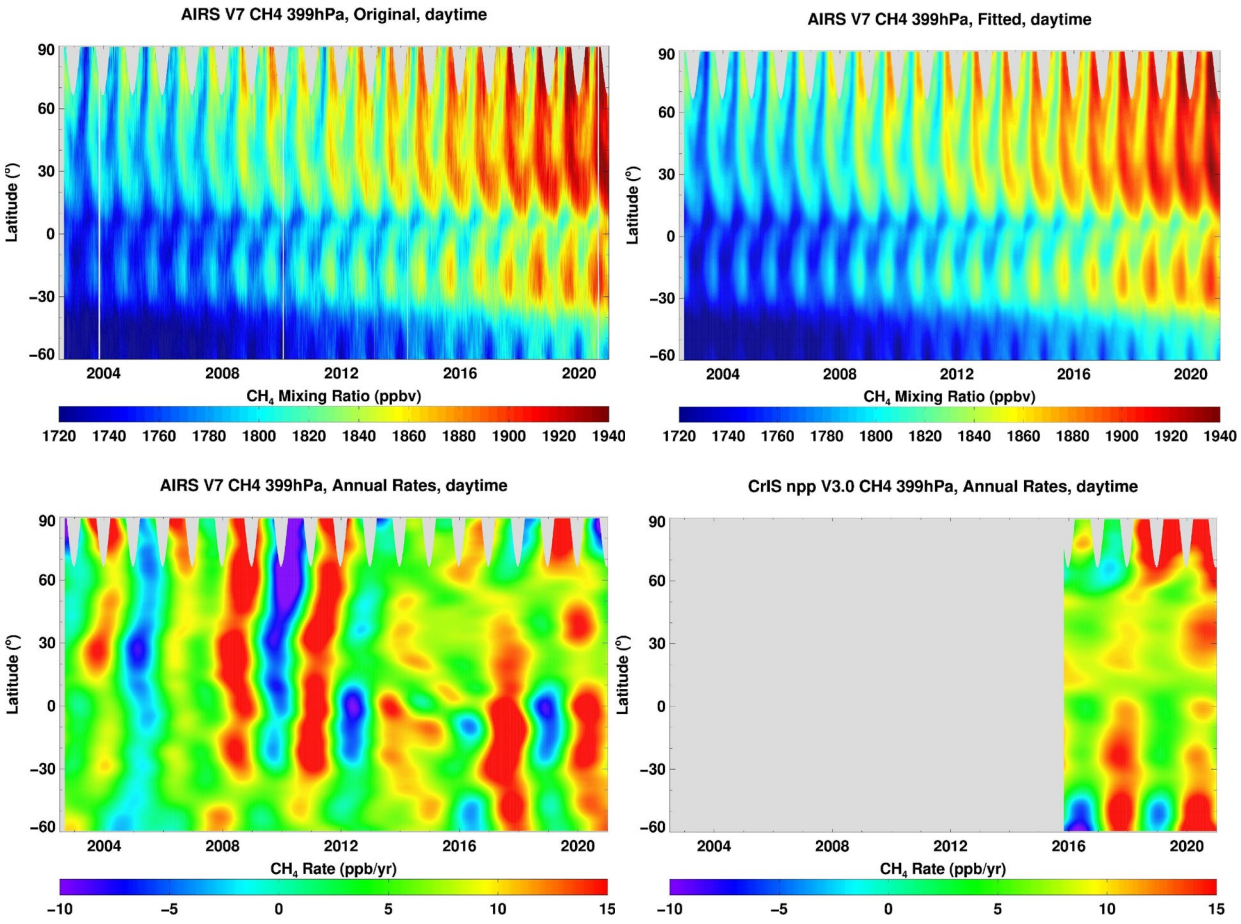

Fig. 19: CH_4 latitudinal distributions with time (upper panel); AIRS original (left upper pane); and AIRS fitted (right upper panel); and the corresponding rate of change from AIRS (lower left), and CrIS (lower right).

3.4 Summary and Conclusions

In Chapter 3 it was described the global climatology of CH_4 concentration derived from nearly 20 years of atmospheric methane from thermal infrared sounders. The global distribution of the atmospheric methane and its changes with seasons were presented. The zonal distribution and vertical distribution with time were also analyzed. More importantly, the rate of changes was derived from satellite measurements, i.e., AIRS vs CrIS, which has not been done prior to this study. The conclusions from this chapters are as follows:

- The global mean of the atmospheric methane at 400 hPa, change from 2003 at 1754.0 ppbv to 2020 at 1838.9 ppbv, representing a total increase of 4.8% during this 18 year period.
- The zonal distribution varied with time. The variation in the tropics was smaller than the NH and SH mid-latitudes.
- Growth rates calculated from AIRS are higher than those from the CrIS and GML.
- The satellite retrieved growth rates also confirmed that atmospheric methane resumed an increases after the 2007 timeframe and kept a trend of sustained increase from 2014 to present.

The key findings have been included in a paper that completed reviews in April 2022 (Zhou, Warner, et al., 2022).

Chapter 4: Methane Trends Over Two Decades

The global monthly mean CH_4 from AIRS, CrIS, and GML measurements are shown in Fig. 20. It is clear that CrIS(blue) and AIRS v7 (red) CH_4 trends at 400 hPa agree very well with GML measurements (green). Whereas the GML measurements showed a sudden increase in 2008, it happened a year later, in 2009, for AIRS. Fig. 20 also shows that the CrIS CH_4 trend is in better agreement with GML, than AIRS. In this chapter, we will present the trends results in detail, e.g., for different latitudinal zones and inter-polar differences.

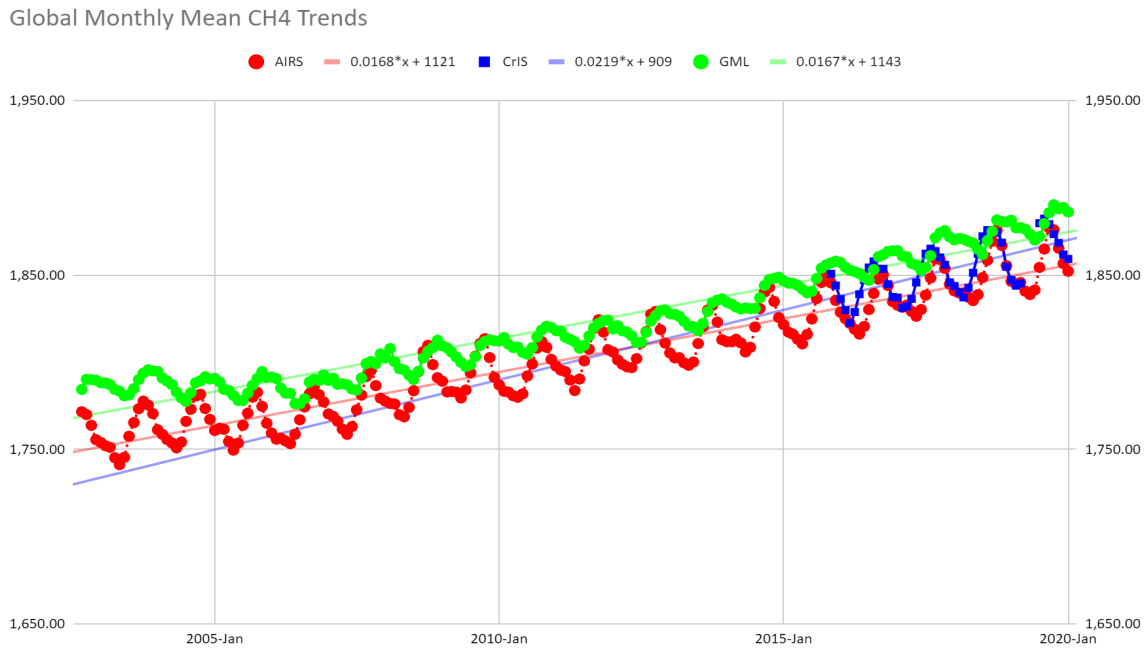

Fig. 20: Time series of Global Monthly Mean of CH_4 at 400hPa from AIRS V7 (red) and CrIS (blue), and the GML measurements (green)

4.1 Latitudinal Variations and Inter-Polar CH_4 Differences

The latitudinal variations in atmospheric CH_4 have been discussed in previous studies (C. Kroeze, 1992; Nisbet, 2016, 2019). The thick blue curve in Fig. 21 shows the averaged zonal mean

variations from 18 years of AIRS CH_4 data at 400 hPa (2003-2020). The lowest value (~1730 ppbv) is over the Antarctic region, and the highest value (~1858 ppbv) is over the Arctic region. The zonal mean each year from 2003 to 2021 is also shown in Fig. 21. It is clear that CH_4 concentrations in general are higher in the NH than in the SH due to emission sources, which are predominantly from land surface and located in the NH. The increase in CH_4 in the south pole region is the smallest, compared to increases in the other latitudes. The two largest picks of the increases in Fig. 21 in the north and south sup-tropical zones.

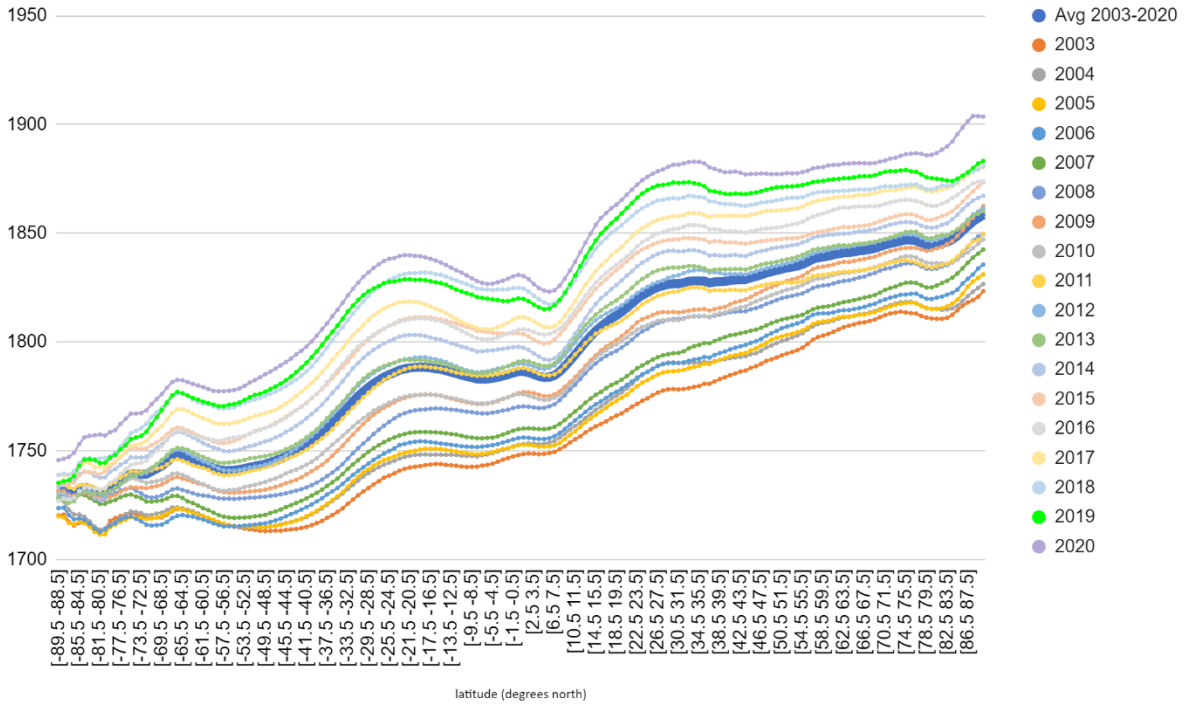

Fig. 21: Zonal Mean of AIRS V7 CH_4 at 400 hPa, averaged using 18 years of AIRS data from 2003 to 2020 (thick line), along with zonal means of each year from 2003 to 2020.

The Inter Polar Difference (IPD) is defined as the calculated annual pole-to-pole difference amounts (Steele et al., 1987; Dlugokencky et al., 2003). It is used as a sensitive indicator of the CH_4 emission in the Arctic (O. B. Dimdore-Miles et al., 2018, Bruhwiler, et al., 2021). Earlier studies found that CH_4 concentrations was 10% higher in the Arctic as compared to the Antarctic

(Rasmussen and Khalil, 1984). They also concluded that this finding is consistent with the expected ratio of about 1.07 - 1.11 obtained from a global mass balance model. The absolute CH_4 IPDs are calculated as the differences between zonal averages for 53-90N and 53-90S, AIRS V7 CH_4 products at the level centered at 400 hPa. The mean IPD for the period from 2003 to 2021 is approximately 106 ppbv, the minimum value is 91 ppbv in 2003, and maximum is 118 ppbv occurred in 2020. The time series of the IPD and the ratio derived from AIRS V7 CH_4 products are shown in Fig. 22. While the IPD has been stable in the past two decades, there are inter-annual variations that has been steadily increasing. This is consistent with the zonal mean plot which shows that the CH_4 increase in the NH polar region is larger than that of the SH polar region. It indicated that the increase of the CH_4 concentration resulted in an increase of the pole-to-pole difference. The ratio, on the other hand, has been approximately constant with a mean of 1.061, range from 1.053 (2003) to 1.067 (2016). These values are very similar to the previous model studies.

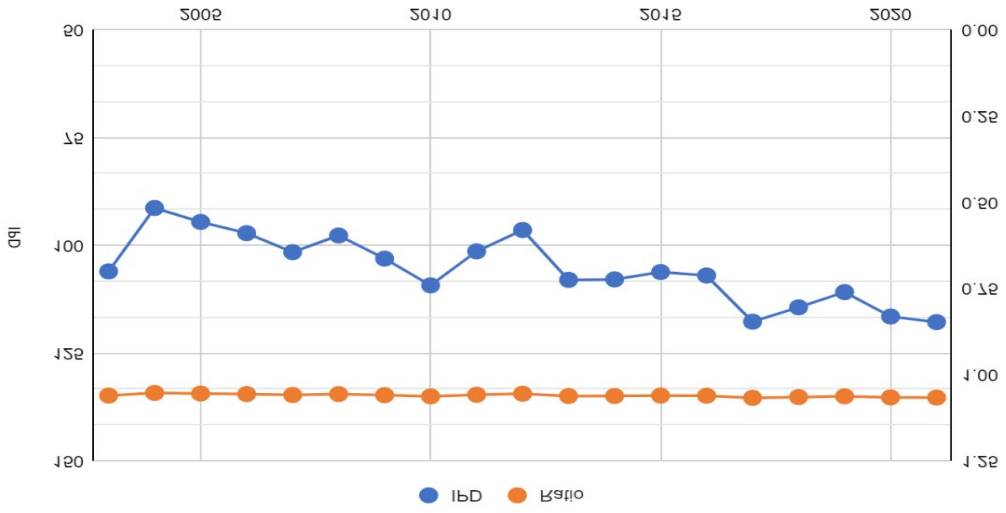

Fig. 22: Time series of IPD and ratio derived from AIRS V7 CH_4 concentration at 400 hPa

To further understand the spatial variation of the atmospheric CH_4, we examined the time series of AIRS and CrIS CH_4 at 400 hPa over different latitudinal zones, and compared with those from the GML. Fig. 23 shows the CH_4 time series at 400 hPa for latitude ranges of 60 - 90°N (top panel), 30 - 60°N (2nd panel), 0 - 30°N (3rd panel), and 90°S - 0 (4th panel), respectively. The CH_4 retrievals from AIRS (blue lines, 2003 - 2020) and CrIS (orange lines, 2015 - 2020) are in good agreement and both show that the overall atmospheric CH_4 concentrations at 400 hPa have been increasing across all latitudinal zones. The trends are similar to those of the GML observations (green lines, 2003 - 2020), even though the magnitudes of the CH_4 concentrations between the satellite products of the free troposphere and the near surface in situ measurements are expected to be different.

The CH_4 concentrations show annual cycles that are different for different latitudes. As shown in Fig. 23, the amplitudes of the annual cycle are higher for the mid- and high- latitudes in the NH, compared to those from tropical regions owing to the CH_4 sources being mostly located in the NH mid- to high- latitudes. Since the GML in situ observations are from the near surface stations, they represent the CH_4 concentrations near the emission sources. Fig. 23 clearly shows that the retrieved CH_4 concentrations from AIRS and CrIS at 400 hPa have an overall negative bias compared to those from GML in the NH. This indicates that the CH_4 concentration is higher at the surface and decreases in the free troposphere.

The highest difference between the GML and AIRS CH_4 is 105 ppbv for 60 - 90°N, and 122 ppbv for 30 - 60°N; and 56 ppbv for 0 - 30°N. On the contrary, the CH_4 retrievals at 400 hPa are higher than or similar as those from the surface observations in the SH. On average, the AIRS CH_4 is 4 ppbv higher than those from GML in the SH, and 0.5 ppbv for CrIS. Judging from the differences between CH_4 concentrations at 400 hPa and the surface, we concluded that the vertical

gradients in the mid- to high- latitudes are much higher than those in the tropics and SH. Also note that while the similar magnitudes in seasonal variations are found in GML and CrIS CH_4, the magnitudes of the seasonal variations are smaller than those with AIRS, which are likely due to the differences in the algorithms as discussed in Section 2.3.

Figure 23 also shows a significant phase shift in the annual cycles of satellite products and the situ measurements, especially in the mid- to high latitudes in the NH. Such a phase shift is not obvious in the tropical zones nor in the SH. In the latitude zone 60 to 90ºN, the CH_4 concentrations at 400 hPa retrieved from AIRS and CrIS show about 7 – 8 months of lag to the in-situ concentrations. Similar phase shifts are observed in the mid-latitudes of 30 – 60ºN, with the lags about 4-5 months. The lags are minimal for the tropical and the SH regions. The cause of it for this shift is studied with model simulations.

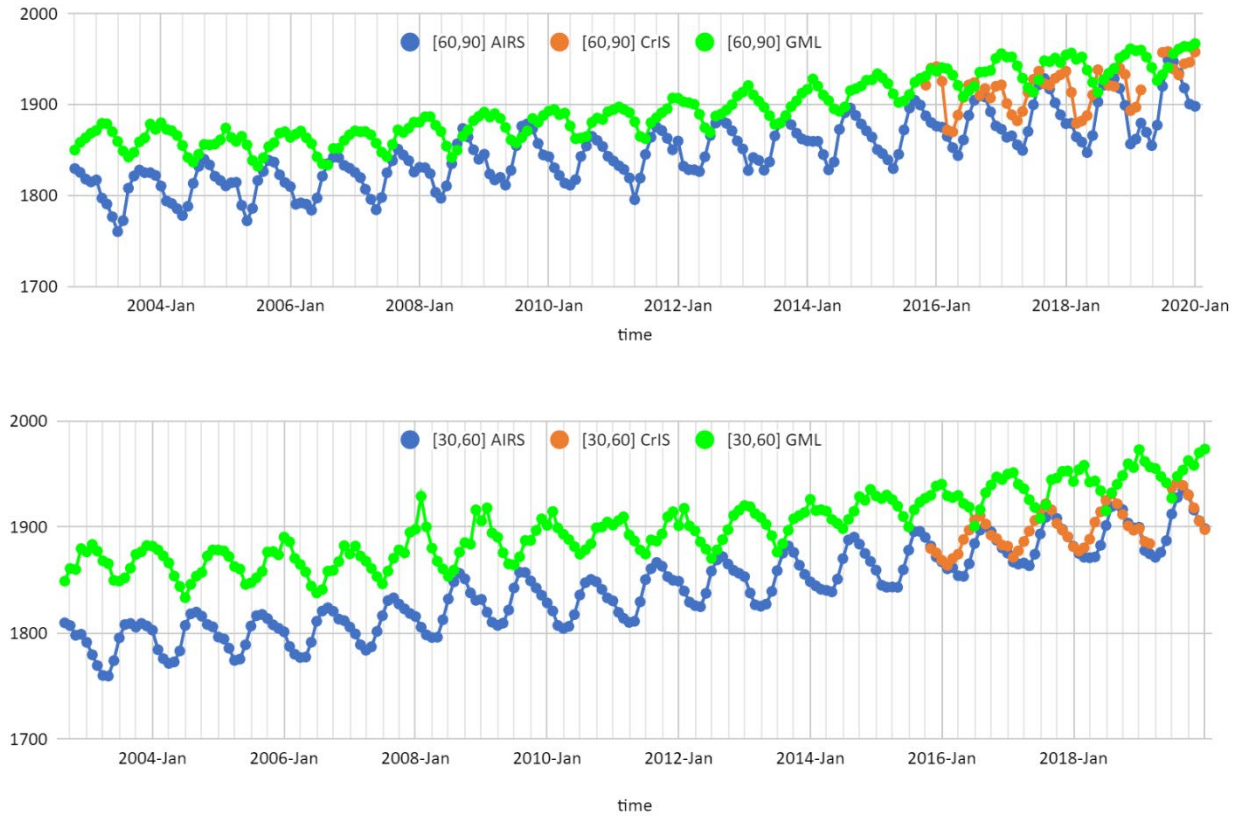

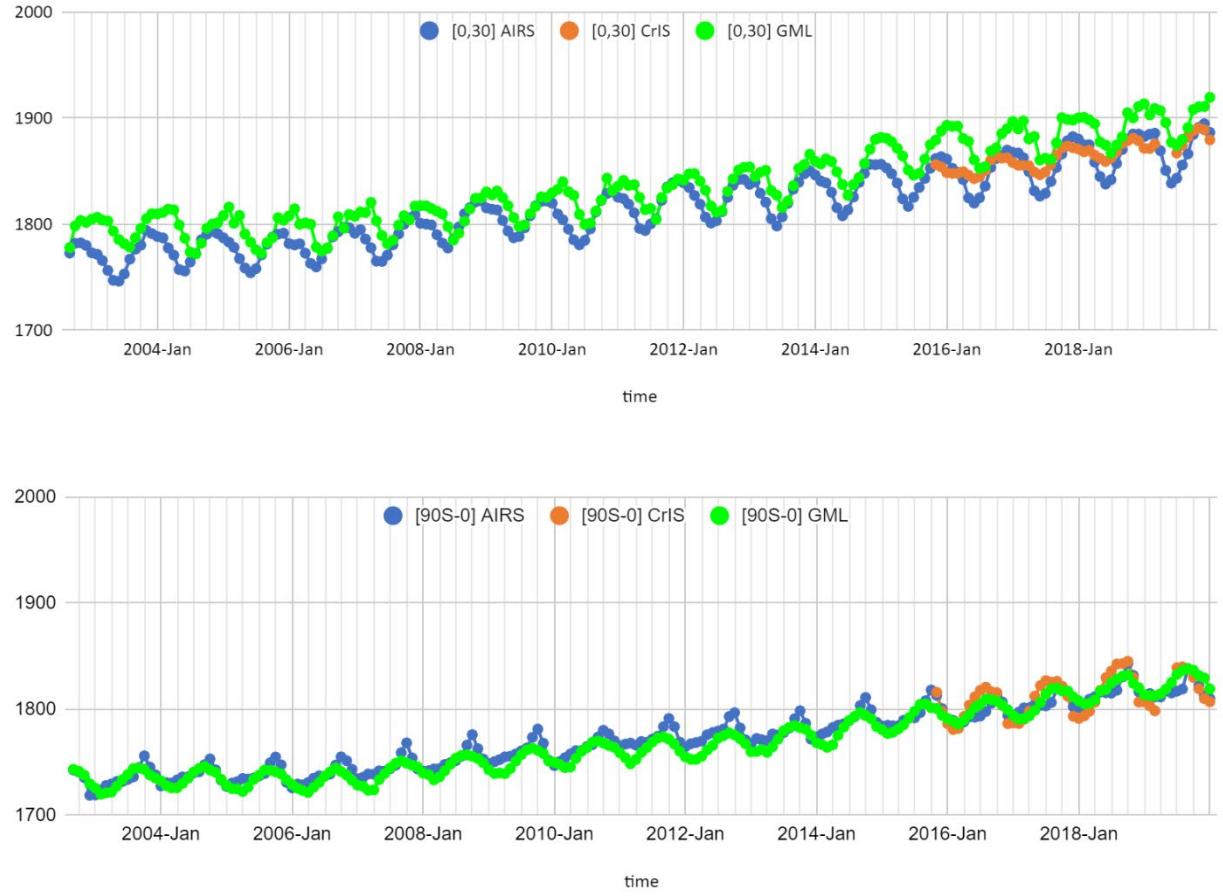

Fig. 23: Time series of CH_4 retrieved from AIRS, CrIS at 400 hPa vs. the measurements from NOAA GML; for different latitudinal bands: [60 – 90°N]; [30 – 60°N]; [0 - 30°N]; [90°S - 0].

4.2 Understanding the Seasonal Phase Shift Using Model Analysis

To better understand CH_4 seasonality, we further examined the results from The Community Atmosphere Model (CAM) with Chemistry (CAM-chem). CAM-chem is an extension of the CAM and a component of the NCAR Community Earth System Model (CESM). It is used for simulations of global tropospheric and stratospheric atmospheric composition. Chemistry in CAM-chem is based on the Model for Ozone and Related chemical Tracers (MOZART) family of chemical mechanisms, with various choices of complexity for tropospheric and stratospheric

chemistry (Emmons et al., 2010). The first version of CAM-chem is described in Lamarque et al. (2012). CAM-chem in CESM1.2 is described in Tilmes et al., (2015). The current version is CAM6-chem in CESM2, based on version 6 of the Community Atmosphere Model (CAM6).

In this study, we exploited six years (2015 - 2021) of global simulations performed with the CAM6-Chem model on 0.9º x 1.25º resolution (latitude by longitude) horizontal resolution with 32 vertical layers reaching up to about 1 hPa (40 km) (Tilmes et al., 2019; Buchholz et al. 2019). Meteorology is driven by specified dynamics, by nudging with 50h relaxation (1%) to Modern-Era Retrospective analysis for Research and Applications (MERRA2) fields of temperature, horizontal winds, and surface fluxes (Molod et al., 2015). Chemistry is the MOZART-T1 mechanism, described in Emmons et al., (2020). Anthropogenic emissions are from the Climate Model Intercomparison Project round 6 (CMIP6), CMIP6 2014 anthropogenic emissions are repeated for dates post 2014 to 2016. Anthropogenic and other emissions were changed to the Shared Socioeconomic Pathways (SSP) 5-8.5 for 2017 onwards. Biogenic emissions were from the Model of Emissions of Gases and Aerosols from Nature version 2.1 (MEGAN 2.1), fire emissions were from Quick Fire Emissions Dataset (QFED). Below are the preliminary results from the model simulations.

The CH_4 time series for different vertical levels and different latitudinal bands from the CAM-chem runs are shown in Fig. 24. Six pressure levels are plotted from 506 hPa to 101 hPa, with 506 hPa in red, 313 hPa in cyan, and 101 hPa in dark blue. The top left panel is the time series of the zonal means for 60 - 90°N, top right is 30 - 60°N, lower left is 0 - 30°N, and lower right is 90°S - 0. A similar lower to upper troposphere and lower stratosphere phase shifting as seen by the satellite measurements described in section 3.3, can also be seen in the model results. For 60 - 90°N, while the 313 hPa (in cyan color) starts showing the phase shift, it becomes much larger in

stratospheric levels (193 hPa and 101 hPa). The CH_4 amounts are much lower in the stratosphere. Similarly, for 30 - 60°N, the phase changes can be seen between 506 hPa and 313 hPa, and reach to 4 - 5 months at the 101 hPa level in the stratosphere. For sub-tropics 0 - 30°N, the change within troposphere is small, possibly due to strong convection, and the values for the stratosphere are close to those from the lower troposphere. There is minimal phase changes between stratosphere and troposphere compared to mid-to high NH. As in the case of the tropics, there is also minimal seasonal phase shifts in the SH. The magnitude of the shifts is likely depending on the age of CH4 and transport processes.

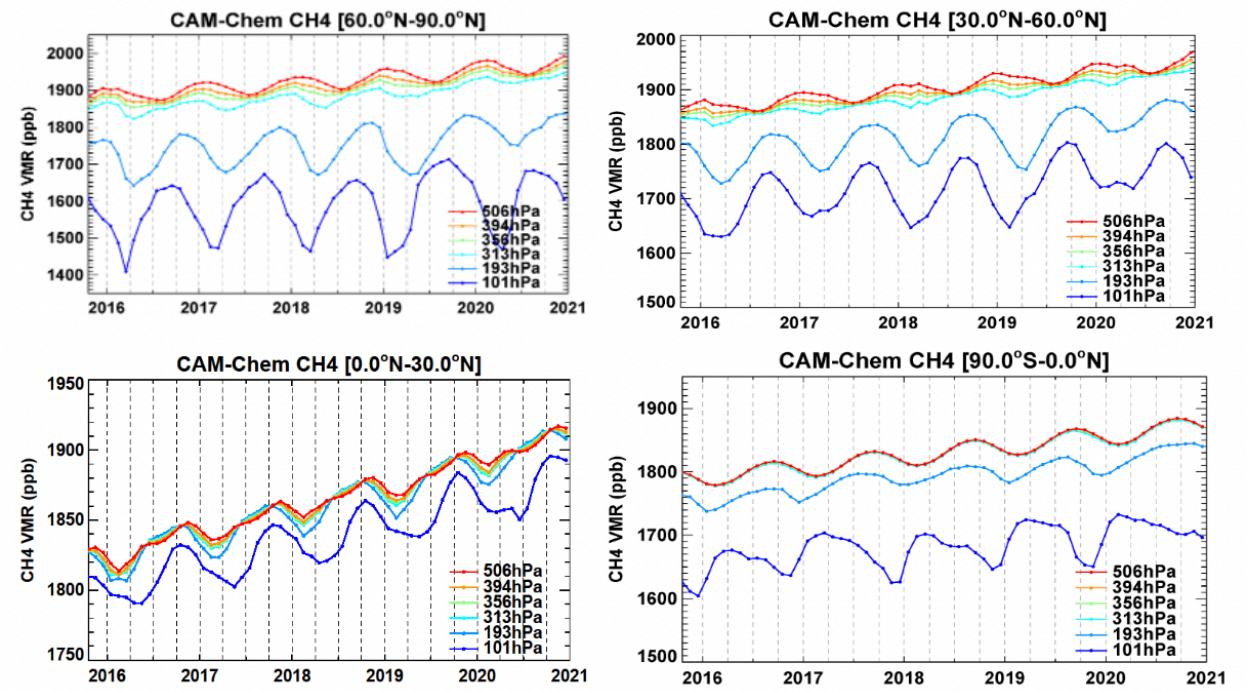

Fig. 24: Time series of the zonal averaged CH_4 from CAM-chem runs from 2015 to 2021 at 313 hPa, 356 hPa, 394 hPa, 506 hPa, and 843 hPa for different latitude bands. a) 60 - 90°N; b) 30 - 60°N; c) 0 - 30°N; d) 90°S – 0.

Figure 25 are the curtain plots showing the vertical cross sections of CH_4 over time, for different latitude bands: 60 - 90°N (top left), 30 - 60°N (top middle), 0 - 30°N (top right), 90 - 60°S (lower left), 60 - 30°S (lower middle), and 30°S - 0 (lower right). Similar phase shifts are

observed for the northern latitudes, and strong vertical gradients occur in the tropopause regions for 60 - 90°N, and 30 - 60°N latitude zones. In the SH, CH_4 concentration remain almost constant from the surface across the troposphere. This may be attributed to the lack of emission sources in the surface in the SH. From both Fig. 24 and Fig. 25, the results show that for the layer between 200 hPa and 400 hPa, where the AIRS and CrIS retrievals are most sensitive, the tropospheric retrievals maybe contaminated by stratospheric CH_4. The magnitude of the contamination varies with different latitudes, depending on factors such as tropopause heights.

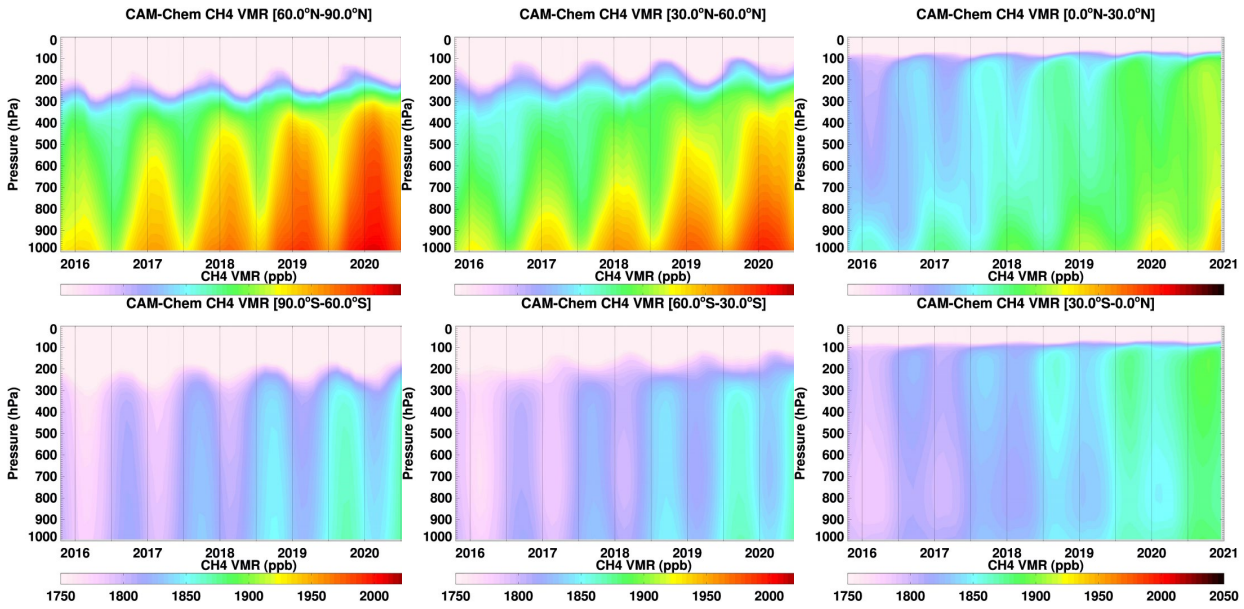

Fig. 25: Pressure-time cross section of CH_4 from CAM-chem runs from 2015 to 2021 for different latitude bands. a) 60-90°N; b) 30-60°N; c) 0-30°N; d) 90-60°S; e) 60-30°S; f) 30°S-0

4.3 CH_4 Mean Annual Cycle in NH vs. SH

To better characterize the CH_4 trends and seasonal cycle, the annual means of seasonal cycles for NH and SH derived from AIRS (2002 – 2020), CrIS (2015 – 2020) at 400 hPa, as well as GML in situ (2002 – 2020), were plotted in Fig. 26. The upper left panel shows the mean annual cycles for the NH, the upper right for the SH. The CH_4 concentration at 400 hPa from CrIS show a phase shift of ~5 months, and AIRS shows a phase shift of ~7 months. On the right the results of SH show that the phase changes are minimal, ~0 month for CrIS, and less than 2 months for AIRS. For both NH and SH, CrIS shows better agreements with GML than AIRS because CrIS algorithm was updated recently and represent more realistic values (see Chapter 2). The lower panel of Fig. 26 displays the de-seasonal trends with the seasonal cycles removed. Both SH and NH showing a steady increase trend after 2006; the trend of NH is slightly steeper than that of

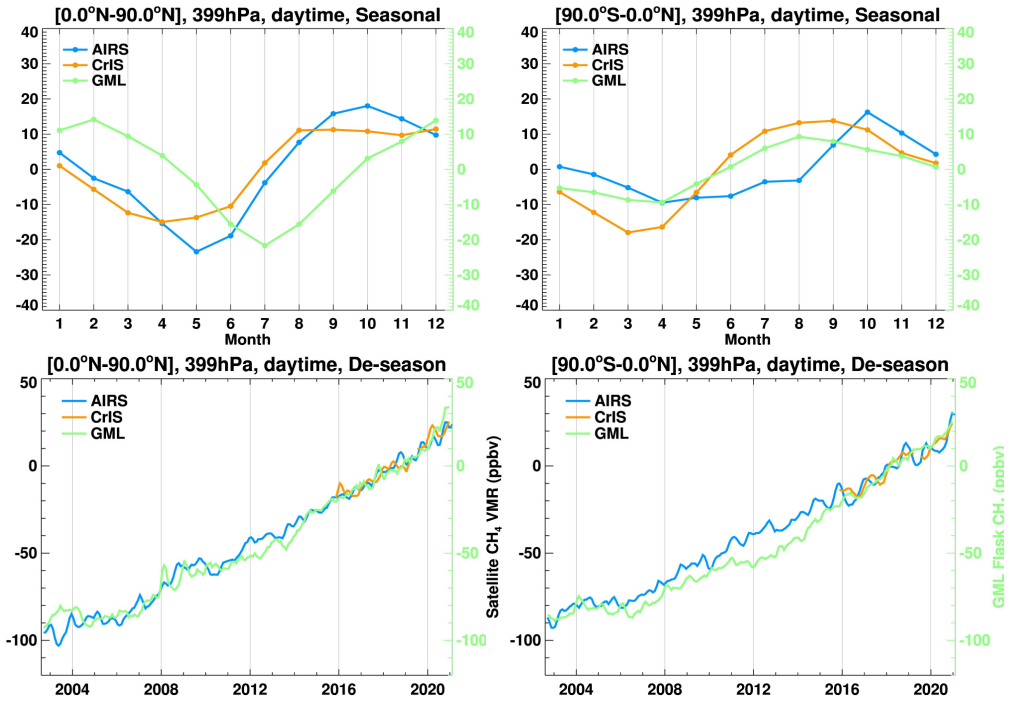

Fig. 26: Time series of annual means of CH_4 seasonal cycles from AIRS, CrIS at 400 hPa and GML observations for NH (upper left), and SH (upper right). The de-seasonal trends for NH (lower left), and for SH (lower right).

SH. These results further confirmed our findings described in the previous section that the phase shifts are much smaller in the SH than in the NH. The contaminations in the tropospheric retrievals are from the stratosphere CH_4, rather than instrument/sensor issues. (Dr. Hugo Berbery, personal communication).

4.3 Summary and Conclusion

In Chapter 4, further analysis of the latitudinal changes of atmospheric CH_4 concentration retrieved from AIRS and CrIS were presented. It started with the examination of the averaged latitudinal changes and the Inter-Polar Difference, then analyzed the time series of the atmospheric CH_4 concentration for different latitudinal zones. We discovered the phase shift of the atmospheric CH_4 concentration when compared to the in-situ observations. By analyzing the vertical distribution from the atmospheric chemistry models, we verified that the phase shift is mainly due to the contamination of the stratosphere CH_4 to the tropospheric retrievals, e.g. at 400 hPa. The results also indicated that it is important to establish consistent long term data records of atmospheric CH_4 concentration using the validated retrieval algorithms. The following conclusion can be draw for this chapter:

- Latitudinal trends of the atmospheric CH_4 concentration retrieved from AIRS and CrIS are consistent with in-situ.
- During the study it was discovered that there are seasonal phase shifts of the satellite retrieved CH_4 when compared to the ground in-situ measurements.
- By analyzing the vertical distribution from the atmospheric chemistry models, we verified that the phase shift is mainly due to the contamination of the stratospheric CH_4 to the tropospheric retrievals.

- While we found that there are stratosphere CH_4 in the tropospheric retrievals, the contamination is strongest in the NH mid and high latitudes, and decreases towards the tropics and SH.

The key findings from this work (covered in Chapter 3 and 4) have been included in a publication submitted to Remote Sensing in April 2022 (Zhou, Warner, et al., 2022)

Chapter 5: Results for Regional Studies

As introduced in Chapter 1, besides using the retrieved products to assess the global CH_4 distributions and changes, it is also important to demonstrate the applications of the CH_4 products to the selected focus areas, i.e., South America and the Arctic. The material in this Chapter is important because on the one hand they are associated with the tipping points of the climate changes due to anthropogenic activities, and on the other hand, these areas are in strong needs of the satellite products due to the lack of the ground observations.

5.1 Regional Study 1: South America

The annual averaged CH_4 maps at 400 hPa retrieved using AIRSv7 for the year of 2003 and 2020, plotted with the same color scales, clearly show that the CH_4 concentration increases in South America (Fig. 27). Whereas there were high CH_4 concentration in the northern part of the South America (Venezuela, etc.) for both 2003 and 2021, the central region of South America (Brazil, Colombia, Argentina, etc.) became another center of high CH_4 region in 2021.

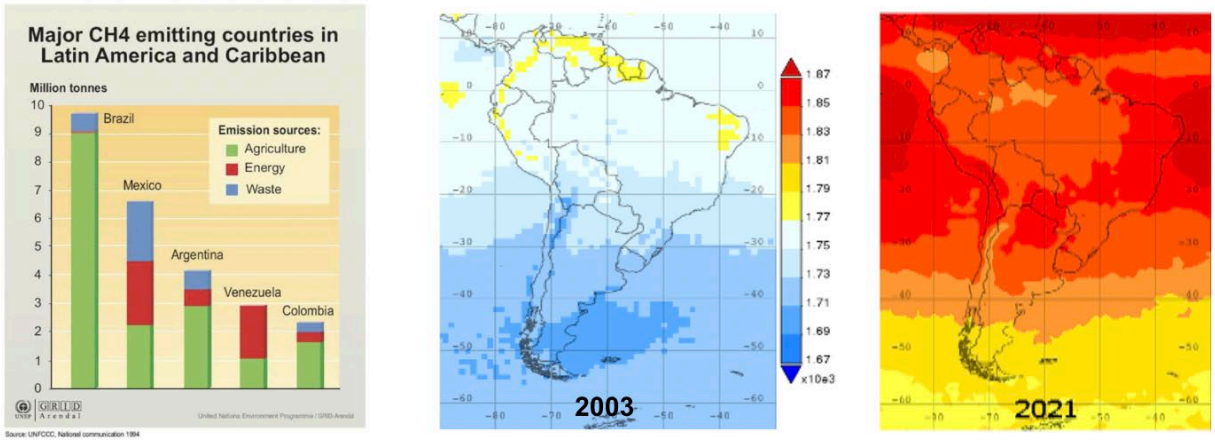

Fig. 27: Image on the left: Main CH_4 emitting countries in Latin America and Caribbean, From collection: Vital Climate Graphics Latin America and the Caribbean, Cartographer: Viktor Novikov, UNEP/GRID-Arendal; Plot in the middle: Annual averaged CH_4 at 400 hPa from AIRSv7, 2003; Plot on the right: same as the middle but plot for 2021.

To examine the changes of CH_4 concentration over time, the annual averages of CH_4 concentration maps for all the years from 2003 to 2022 were plotted in Fig. 28. It is revealed from these maps that there has been a steady rise of atmospheric CH_4 concentration over the entire South America region. As one can see from these maps, from around 2014, there was another center of the high CH_4 concentration formed in the southeast of the Amazon basin. Fig. 29 plotted the time series of CH4 concentration over the entire South America region vs the southeast Amazon region. It shows that the increase of the southeast Amazon region is faster than the overall region. There can be multiple sources contributing to this high concentration, e.g., agriculture, the fossil fuel/gas productions and transportation, biomass burning, and wetlands of Amazon.

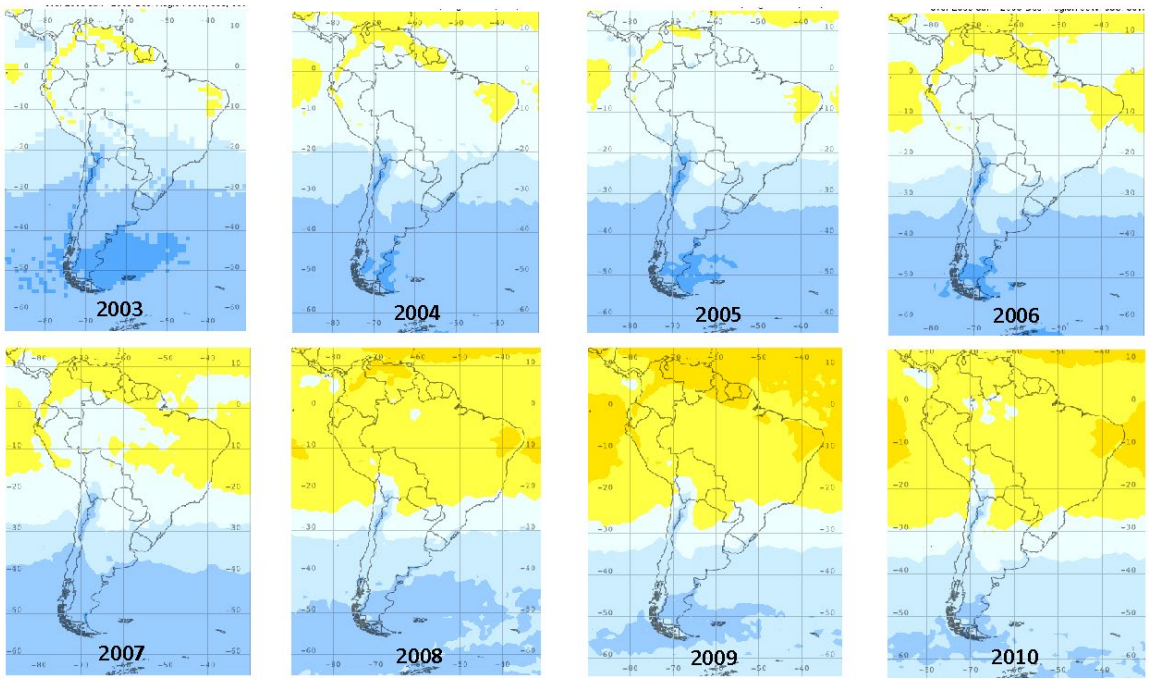

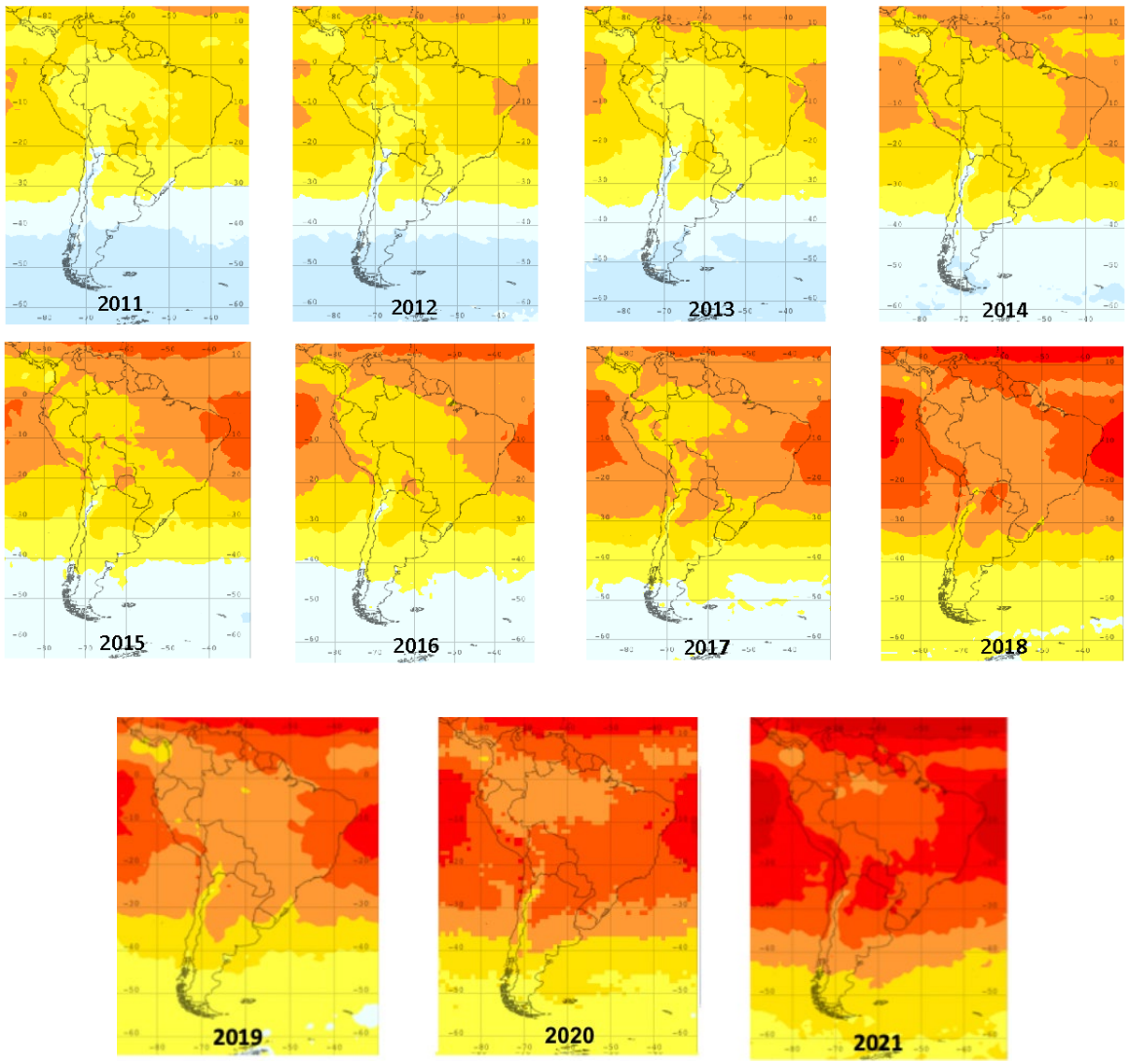

Fig. 28: Annual averaged CH_4 400 hPa maps from AIRS v7, 2003 to 2021. (Data processed and downloaded from NASA GES Giovanni and plotted with Panoply).

To further understand the increased CH_4 in the middle of South America, monthly averages of 2003 and 2020 for 3 different regions (Venezuela, Brazil, Argentina), as well as the area averaged of South America are examined (Fig. 29). The results show that there are two peaks for all three regions: one is during the wet season (Dec-March) matches the peak emissions from the wetlands of Amazon and Pantanal; there are second peaks for the dry season (July - October) which may correspond to the biomass burning etc. While the CH_4 concentrations of Venezuela are the

highest during the time, CH_4 concentrations in Brazil increased from 2003 to 2020 and showed higher values during the dry period of June to September than the other regions. More studies are needed to understand the exact reasons for these, such that it helps to define the pathways to future mitigation.

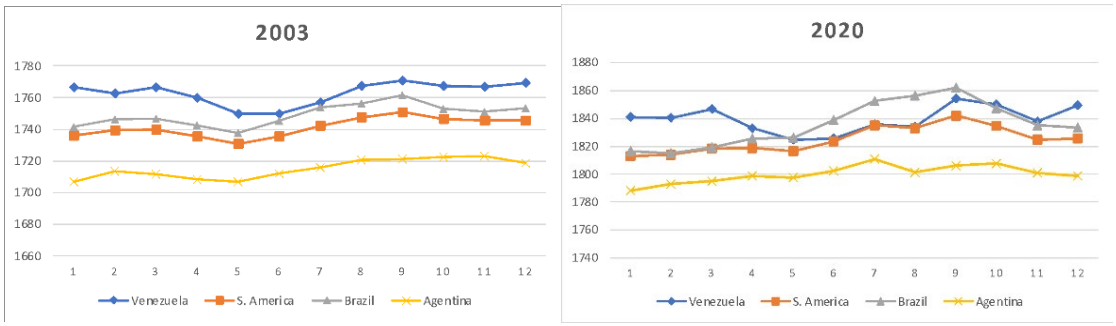

Fig. 29: Monthly mean of CH_4 at 400 hPa over Venezuela (blue), Brazil (gray), Argentina (yellow), and South America (orange), from AIRS v7, 2003 (left panel), and 2020 (right panel).

5.2 Regional Study 2: the Arctic

There are 22 atmospheric stations in the Arctic region (above 60°N) measuring CH_4 mole fractions, among which 12 sites provide continuous observations. Although sparse, these stations are well illuminated by ocean and land CH_4 emissions because of the fast-horizontal transport of air masses around the North Pole (e.g., Bousquet et al., 2011). Among these 12, we selected the following 6 stations for our studies considering the data availability for the time period of the hyperspectral sounding retrievals: 1). Alert/ALT, 2). Barrow/BAR, 3). Pallas/PAL, 4). Summit/SUM, 5). Tiksi/TIK, 6). Ny-Alesund/ZEP), as listed in Table 4. To compare the satellite retrieved CH_4 with the ground observations, we downloaded Atmospheric CH_4 Dry Air Mole Fractions data from the NOAA ESRL GMD Carbon Cycle Cooperative Global Air Sampling Network from the NOAA ESRL web page. Fig. 30 shows a map of the averaged atmospheric CH_4 concentration at ~500 hPa retrieved from CrIS, with the locations of these stations. These stations

are across the arctic region with a range of CH_4 distributions: from the low amounts over the ice-covered Summit station in Greenland, to TIK, and PAL, where the CH_4 amounts are much higher.

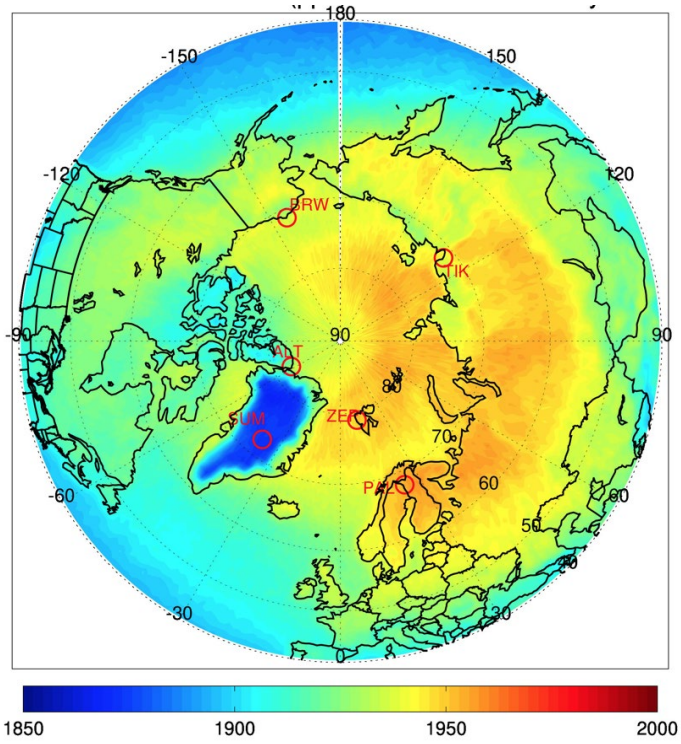

Fig. 30: CrIS CH_4 at 500 hPa, 2018 annual mean. The six GML stations are marked in red.

Table 4: List of GML Observation Stations (Dlugokencky et al., 2019)

Stations	sample_latitude	sample_longitude	sample_altitude	sample_elevation	sample_intake_height
ALT	82.50	-62.34	210.00	200.00	10.00
BRW	71.32	-156.60	14.00	11.00	3.00
PAL	67.97	24.12	570.00	565.00	5.00
SUM	72.60	-38.42	3214.54	3209.54	5.00
TIK	71.60	128.89	29.00	19.00	10.00
ZEP	78.91	11.89	479.00	474.00	5.00

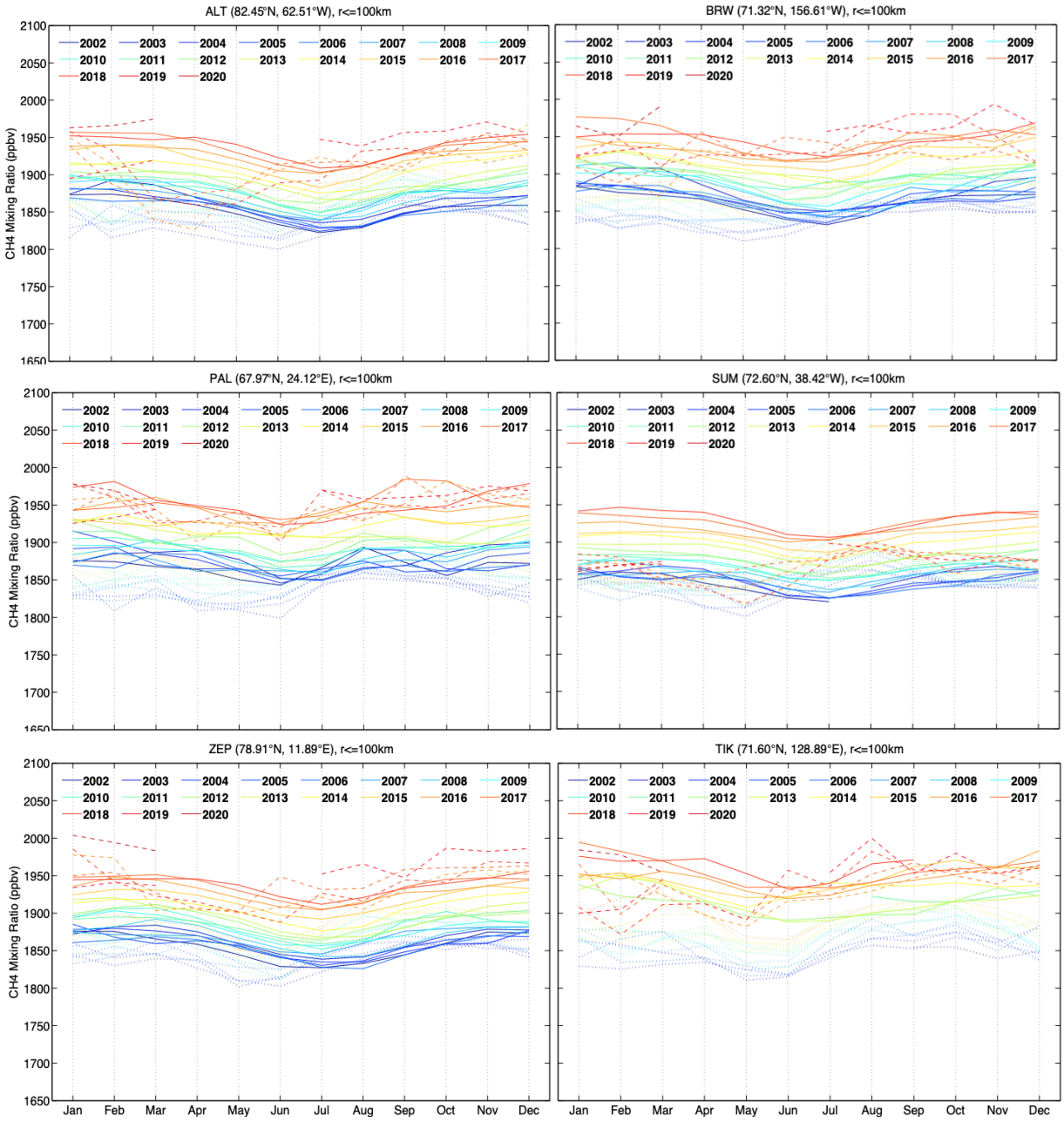

Fig. 31: a-f: Comparisons of the monthly mean atmospheric CH_4 from AIRS (dotted line), CrIS (dashed line), with GML stations (solid line) for the years of 2002 to 2020. (a. upper left) ALT; (b. upper right) BRW; (c. middle left) PAL; (d. middle right) SUM; (e. lower left) ZEP; (f. lower left) TIK.

The CH_4 derived from AIRS and CrIS data at 400 hPa level, and the in-situ station measurements showed similar trending, as showed in Fig. 31. In this Figure, the CH_4 monthly mean derived from the AIRS and CrIS for each year from 2002 through 2020, were plotted against

the in-situ measurements over the six selected stations. The interannual variability not only shows the consistent increasing trends across each month of the year, but also indicates that CH_4 retrieved are the lowest in the summer months (May, June), the highest in the fall (Sept, Oct). The time series of CH_4 products derived from AIRS, CrIS, and GML stations are shown in Figure 32. Overall CH_4 from AIRS and CrIS are consistent with GML stations. The trends clearly show steady increases of CH_4 for the past two decades. It is important to note that there is no catastrophic sudden rises in CH_4 as indicated by earlier studies. We also identified a retrieval issue over Greenland as indicated by the CH_4 over the SUM station deviating significantly from the in-situ measurements. This will be a subject of future study.

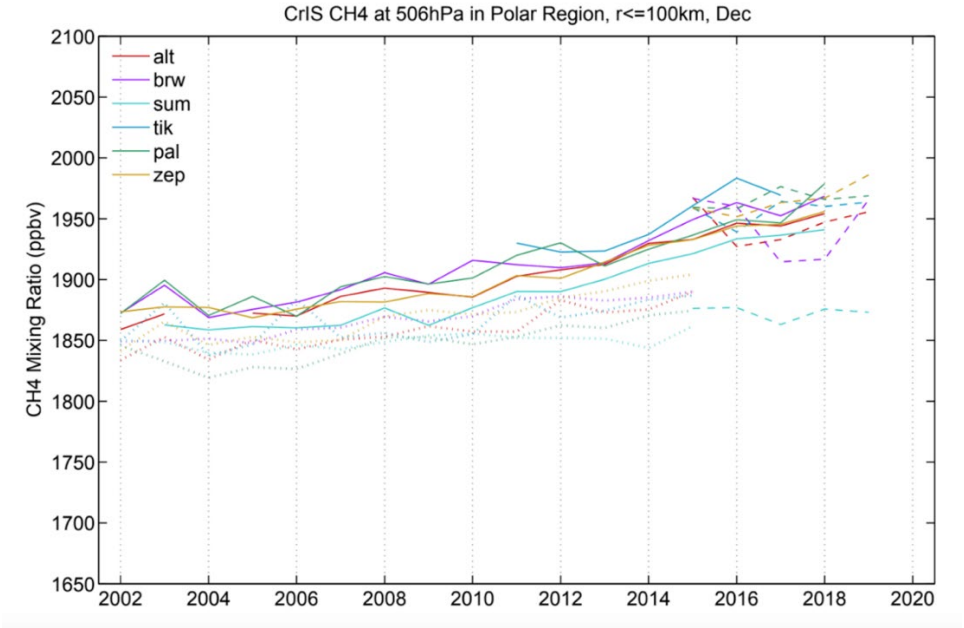

Fig. 32: Time series of CH_4 Products Derived from CrIS, AIRS, and ESRL/GML Stations

5.3 Using Radiances Signals to Assess Trends and Detect Anomalies

There are two types of errors that may impact the trends derived from the retrievals. 1). from the instrument calibration errors, and 2). from the algorithm errors. While we can use the

retrieved CH_4 products to analyze changes and trends, the hyperspectral radiance also contains signals itself for us to independently verify the trends derived from the retrievals or models. For the AIRS retrievals, among the large number of channels used, there are often popping channels included, which may impact the algorithm's performance and product quality. The advantage of using the radiance for selected channels is that one can avoid the bad channels. These inter-comparisons strongly suggest that many AIRS channels are stable to better than 0.02 to 0.03 K/Decade, well below climate trend levels, indicating that the AIRS blackbody is not drifting (Strow, 2019). High spectral resolution in the infrared provides sensitivity to nearly all climate forcing, response, and feedback terms. Specifically, the hyperspectral infrared sounders such as CrIS are sensitive to changes in CH_4, and other carbon trace gases, water vapor, aerosols, temperature, clouds, and surface characteristics. The high spectral resolution of hyperspectral IR sounders provides accurate spectral measurements to better understand the sources, sinks and distribution of trace gases, and can be used to validate weather and climate models by observing changes in the spectral signature.

The radiometric accuracy and stability of AIRS and IASI radiances have been confirmed by several fundamentally different types of comparisons, including the results of the daily measurements of sea surface temperature (SST) (Aumman et al., 2019), direct spectral radiance comparisons from aircraft observations (Tobin et al., 2006); and more recently direct inter-comparisons between IASI and AIRS, which have shown that both AIRS and IASI are highly stable and accurate. The differences between both AIRS and IASI are approximately 0.1 K with a projected stability of 0.1 K per decade (Tobin et al., 2008), (Wang et al., 2009ab). Similarly, CrIS radiance has also been fully validated and met the accuracy and precision requirements with wide margin. It has been adopted as one of the reference measurements by the Committee on Earth

Observation Satellites (CEOS) Global Space-based Inter-Calibration System (GSICS). The CrIS SDRs have also been reprocessed with the most matured algorithms and look up tables (Zou, 2020). The highly accurate radiances can be used to assess the status and viability of the spectral signature of the trace gases.

Principal Components Analysis (PCA) is a classical approach to the problem of independent information extraction. Principal component analysis has been used in sounding applications as described in Wark and Fleming (Walk and Fleming, 1966; Smith and Woolf, 1976), and for high spectral resolution infrared sounders (Huang and Antonelli, 2001; Goldberg et al., 2003). Elements of a principal component score vector are projections of the spectrum onto each of the orthogonal basis vectors, which are the eigenvectors (principal components) of the radiance covariance matrix. The total number, n, of eigenvectors is equal to the total number of channels. However, it will be shown that a much smaller set of k eigenvectors (< 100), ordered from largest to smallest eigenvalues, is sufficient to explain most of the variance in the original spectra. The covariance matrix is derived from an ensemble of AIRS normalized spectra, i.e., radiance divided by the instrument noise. The matrix of eigenvectors, E, is related to the covariance matrix, S, by:

$$S = E \Lambda E^T \tag{13}$$

where S, E and Λ are all dimensioned n x n, and Λ is a diagonal matrix of eigenvalues. The principal component scores (PCS) vector p is computed from:

$$p = E^T r \tag{14}$$

where r is the vector of centered (departure from the mean) normalized radiances. The next equation is used to reconstruct the radiances from a truncated set of k eigenvectors E* and a vector of principal component scores p*. (The symbol * indicated that the matrix or the result of a matrix operation is due to a truncated set of vectors.)

$$r^* = E^* p^* \quad (15)$$

The normalized reconstructed radiance vector is r*, E* has dimension n x k, and the vector p* has length k. To obtain the un-scaled radiance, one must add the ensemble mean normalized radiance used in generating the covariance matrix and multiply the sum by the noise used in constructing the normalized radiances.

Static PCS are very stable over time. It is useful to monitor the changes in the global environment. When an anomaly event occurs, we may see the signature of it in reconstruction scores. A case study I did for the Mt Etna volcano eruption is shown as below. On the top panel of Fig. 34 shows the reconstructed errors for using the static PCS, compared with using the dynamic PCS generated using the dependent data, vs the calibration noise. While it demonstrated the reconstructed errors are within the noise level using the dynamic PCS, the reconstructed errors for using static PCSs can pick up the anomaly caused by Mt. Erna eruption across the spectral bands. The reconstructed errors for static PCS and dynamic PCS can detect the variations of the trace gases effectively and help to narrow down the uncertainties of atmospheric CH_4 estimates.

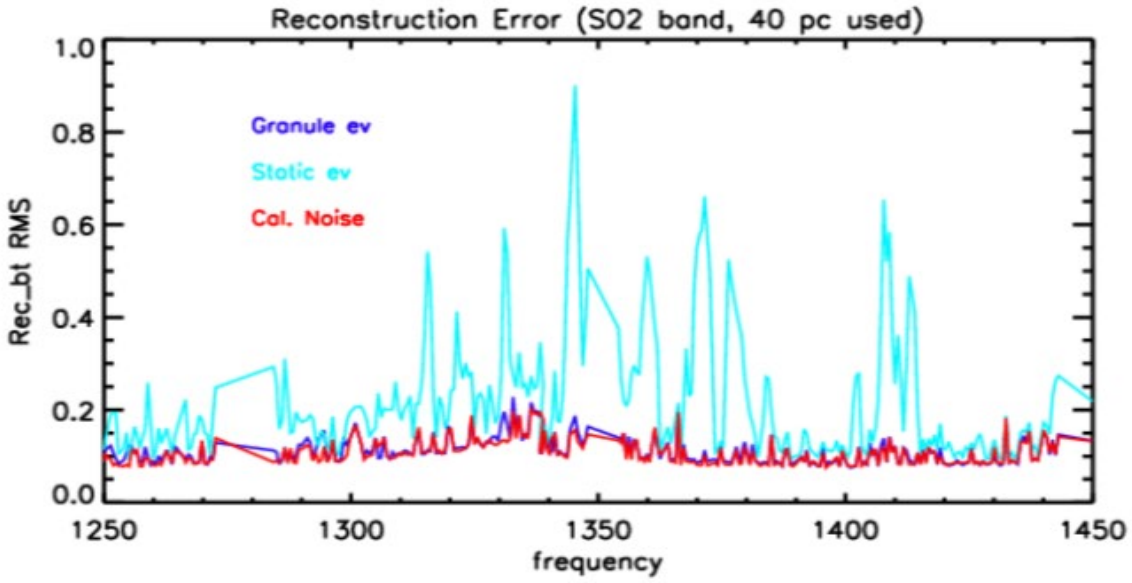

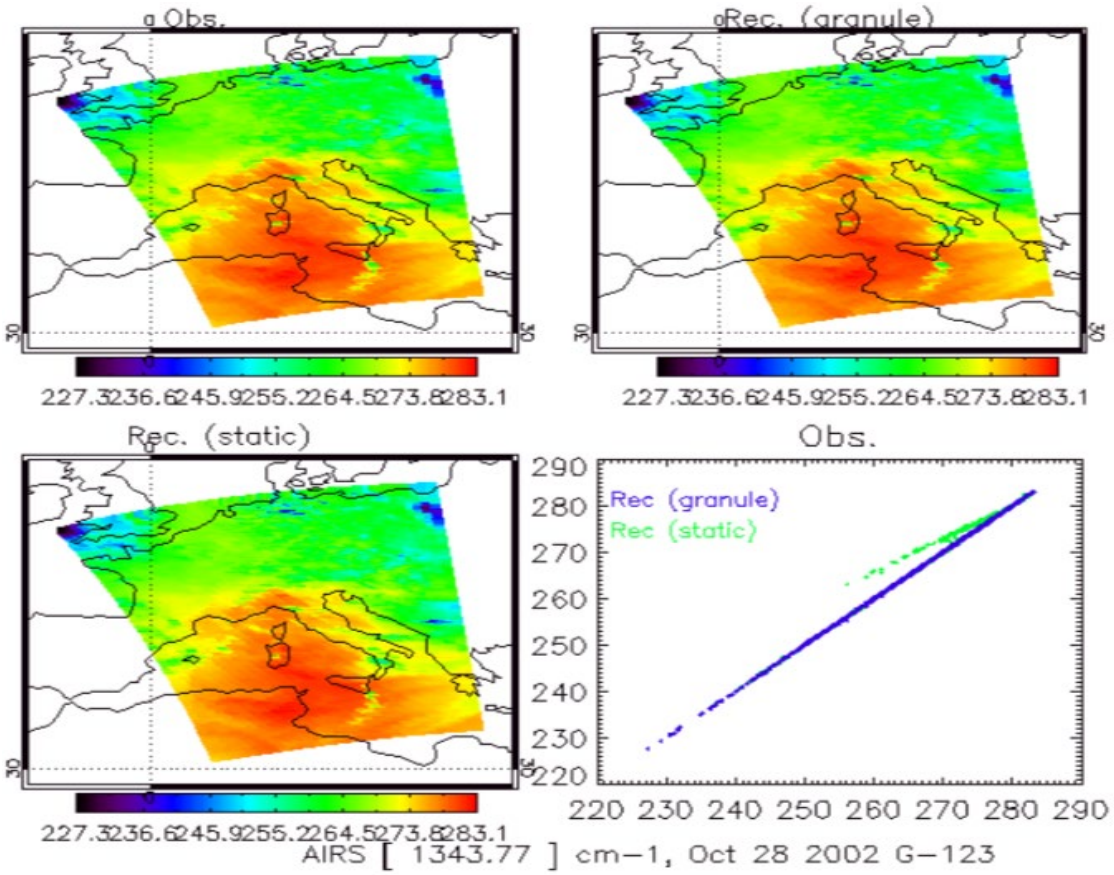

Fig. 33: Reconstructed Radiance Errors from using Granule Eigenvectors (navy), Static Eigenvectors (cyan), vs Instrument Calibration Noise (red) (top); Maps of the Observed Radiance, Reconstructed Radiance with granule eigenvector, Reconstructed Radiance with static eigenvector, and scatter plot of the reconstructed radiances vs observed radiance (bottom 4 panels).

5.4 Summary and Conclusion

In Chapter 5, the regional analysis of the atmospheric methane retrieved from AIRS and CrIS were conducted. The results for South America and the Arctic regions were analyzed, respectively. It was further presented the reason the hyperspectral infrared sounders on polar satellites are important for Arctic monitoring, and the comparison results of CH_4 retrievals compared with the in-situ measurements in the Arctic region. Lastly, the PCA technique and its applications for anomaly detection of the trace gasses such as CH_4 was also demonstrated. Here are the conclusions from this chapter:

- For South America, it is found that a pattern of distribution changed geographically during the past decades, with a new center formed surrounding Brazil region.
- From the Arctic, it was revealed that overall CH_4 from AIRS and CrIS are consistent with GML measurements. The results clearly shown steady increases of CH_4 for the past two decades. No drastic sudden CH_4 rises occurred during 2008 to 2012 as indicated by earlier studies.
- The PCA technique and its applications for anomaly detection of the trace gasses such as CH_4 was also demonstrated for Mt Etna case. It depicted the anomaly radiance signals in the spectra.

Chapter 6: Summary and Conclusions

Through this study, the following new contributions were made to the field of utilizing hyperspectral infrared sounders to monitor global atmospheric CH_4 distributions and variations:

- The global mean of the atmospheric CH_4 at 400 hPa, changed from 2003 at 1754.0 ppbv to 2020 at 1838.9 ppbv, a total of 4.8% increase during this 18-year period.
- The satellite retrieved growth rates confirmed that atmospheric CH_4 resumed the increases after the 2007 timeframe and kept a sustained increase trend from 2014 till present.
- During the study we discovered that there are seasonal phase shifts of CH_4 trends between the hyperspectral sounders CH_4 retrievals and the GML in-situ.
- By analyzing the vertical distribution from the atmospheric chemistry model CAM-Chem, we verified that the phase shifts are mainly due to the contamination of the stratosphere CH_4 to the retrievals for a tropospheric layer, i.e., 400 hPa.
- The stratospheric contamination in the tropospheric retrievals is strongest in NH mid- and high- latitudes, and decreases toward tropics and SH.
- From the Arctic, we revealed that overall CH_4 trends from AIRS and CrIS are consistent with GML measurements. The results clearly show steady increases of CH_4 for the past two decades. No drastic sudden CH_4 rises occurred as claimed by earlier studies.

Hyperspectral thermal infrared sounders provide continuous long-term global records of the mid-to-upper tropospheric CH_4. This climatology study analyzed nearly 20 years of global data on atmospheric CH_4 derived from hyperspectral thermal infrared sounders. The global distribution of the atmospheric CH_4, as well as its changes with seasons, are presented. The zonal distribution and vertical distribution with time are displayed and characterized. The rate of changes derived from AIRS and CrIS are plotted, and the results indicated that while the patterns from the two sensors are in good agreement, there are some differences that can be attributed to the differences between the sensors and/or the algorithm upgrades done for CrIS in the past few years. The rate of changes observed also confirmed that atmospheric CH_4 resumed the increases after the 2007 timeframe and kept an overall increasing trend from 2014 to the present.

The regional analysis of the atmospheric methane retrieved from AIRS and CrIS have been conducted for selected focus areas: South America and Arctic, both areas have experienced unprecedented changes during the past several decades and considered at the tipping points of the human induced climate changes. These areas are also in strong need of the remote sensing data due to the lack of the ground measurements. The changes of CH_4 distribution patters over South America was analyzed, as well as the CH_4 seasonal variations over specific countries. Comparative studies were conducted for the CH_4 derived from hyperspectral infrared sounders with the in-situ measurements of six observing stations in the Arctic region.

The analysis of the latitudinal changes of the atmospheric CH_4 concentration retrieved from AIRS and CrIS is also presented. Starting with examining the averaged latitudinal changes and the Inter-Polar Difference, then analyzing the time series of the atmospheric CH_4 concentration for different latitudinal zones, a phase shift of the atmospheric CH_4 concentration when compared to the in-situ observations was also discovered. It is further verified that the phase shift is mainly due

to the contamination of the stratosphere CH_4 in tropospheric retrievals, by analyzing the vertical distribution of the atmospheric chemistry model outputs. The results also indicated that it is important to establish consistent long term data records of atmospheric CH_4 concentration using the improved retrieval algorithms.

When comparing the retrieved CH_4 concentrations with the GML global in situ observation network, the phase shifts of the CH_4 seasonality between the two data sources were found. The phase shifts are most significant in the NH, where the surface emissions are higher. It leads to the conclusion that the CH_4 layer concentrations from satellite measurements may be including stratospheric contributions that present different seasonality from the mid- to low troposphere. More analysis is needed to fully understand the seasonality phase changes between the surface and upper tropospheric/lower stratospheric atmosphere CH_4 (e.g., more in-depth model studies and high-altitude flight observations). This will further enhance our understanding of the CH_4 transport processes and CH_4 ages. Longer-term trend studies are also important for understanding global CH_4 distributions and variations. CrIS sensors on planned future satellite missions will contribute to this goal.

Through this work, several additional questions have been raised about possible future improvements and enhancements to algorithms to further utilize the remote sensing data for CH_4 monitoring and assessment. Much more research remains in this area, and it will bring many benefits to the Earth's climate, environment, and global society.

Chapter 7: Future Studies

Through this work, the following areas are identified for work in the future, to enhance the utilization of the CH_4 products from the hyperspectral infrared sounders:

- **Conducting more research on using the principal component analysis (PCA) of the hyperspectral radiances for the anomaly and trending of CH_4**: Based on the existing work, with the newly developed hybrid PCA to improve the anomaly trace gases detection. Using hybrid PCA (a combined approach using static and dynamic PCA) to detect the anomaly and trends of atmospheric trace gases e.g., CH_4, and HNO_3, and to identify possible links to the shale oil/gas extraction.

  Alternative algorithms for trace gases retrievals: Through this study, the needs for further upgrading and optimization of the algorithms were identified (e.g., more accurate regression/first guesses, improvements of the forward models and tunings, and further refining the quality controls) for improvements of the retrievals of the trace gases. Furthermore, any alternative algorithms, such as using optimal estimation (OE) approach (Roger, 2000) that adopted by EUMETSAT and other satellite chemistry groups, may need to be explored for CrIS, to maximize all spectral information and provide more realistic 3-dimention fields for trace gases.

- **Long term, continuous data records**: By far we have more than 20 years observations of hyperspectral infrared soundings. It is critical to develop consistent long term data records from the multiple hyperspectral infrared sounders on different satellite platforms (AQUA/AIRS, Metop/IASIs, and JPSS/CrISs). This requires inter-calibration and reprocessing of the Level 1B radiance data products, which had been demonstrated by H. E. Motteler and L. L. Strow (University of Maryland Baltimore County (UMBC), 2021)

with AIRS and CrIS Data - Hyperspectral Infrared Radiance Product (CHIRP). After the reprocessed Level 1B data is validated, the trace gases products need to be reprocessed using the improved algorithms based on the inter-calibrated and reprocessed radiance data sets. With the next generation hyperspectral infrared sounders being developed – Metop Second Generation (Metop-SG)/IASI-Next Generation (IASI-NG), LEO/hyperspectral sounders), such continuous long term data records can contribute significantly to the global monitoring of the trace gases and climate.

- **Fused products for trace gases with other instruments and possibly small satellites**: As described in Chapter 2 of the thesis: While the hyperspectral sounders provide spectral information that is sensitive to middle-upper troposphere/lower stratosphere, the SWIR sensors, such as S5P/TROPOMI and GHG sensors onboard GOSAT satellites, are sensitive to the total column concentration including near surface features. By combining two types of sensors using a carefully designed fusion technique, fused CH_4 data sets for the trace gases can be developed by combining the near surface information from SWIR sensors together with the mid-to upper troposphere and lower stratosphere CH_4 information. There are other new opportunities on CH_4 observations using small satellites, such as GHGSat and other satellites shown in the flyout charts in Fig. 34. The biggest challenge for utilizing the measurements from small satellites is the lack of inflight calibration due to lack of thermal control, so validation transfer from existing validation efforts is important.

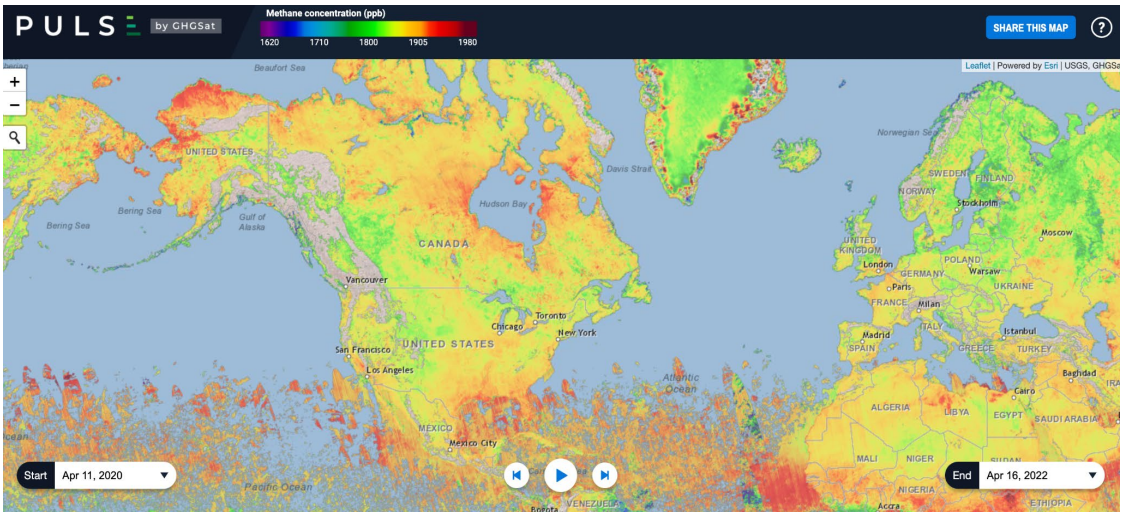

Satellite, Instrument (Agencies)	CO_2	CH_4	Swath	Sample
ENVISAT SCIAMACHY (ESA)	●	●	960 km	30x60 km²
GOSAT TANSO-FTS (JAXA-NIES-MOE)	●	●	3 pts	10.5 km (d)
OCO-2 (NASA)	●		10.6 km	1.3x2.3 km²
GHGSat (Claire)		●	12 km	0.0004 km²
TanSAT (CAS-MOST-CMA)	●		20 km	1x2 km²
Sentinel 5P TROPOMI (ESA)		●	2600 km	7x7 km²
Feng Yun 3D GAS (CMA)	●	●	7 pts	10 km (d)
GaoFen-5 GMI	●	●	5-9 pts	10 km (d)
GOSAT-2 TANSO-FTS (JAXA-MOE-NIES)	●	●	5 pts	10.5 km (d)
OCO-3 (NASA)	●		11 km	4 km²
Bluefield Technologies		●	25x20 km	0.0004 km²
MicroCarb (CNES)	●		13.5 km	40 km²
MethaneSAT (EDF)		●	200 km	1 km²
MetOp Sentinel-5 series (Copernicus)		●	2670 km	7x7 km²
Feng Yun 3G (CMA)	●	●	100 km	< 3 km²
GEOCARB (NASA)	●	●	2800 km	4x4 km²
MERLIN (DLR-CNES)		●	100 m	0.14 km (w)
TanSat-2 Constellation	●	●	3x100 km	2x2 km²
GOSAT-3 (JAXA-MOE-NIES)	●	●	TBD	TBD
CO2 Sentinel (Copernicus)	●	●	3x250 km	2x2 km²

Figure 7-1: The CO_2 and CH_4 satellite time line.

Fig. 34: Example of CH_4 from GHGSat (top), and flyout charts for trace gas satellites missions (Bottom) (Crisp et al., 2018).

Appendix: Zhou L, et al., An Overview of the Science Performances and Calibration/Validation of Joint Polar Satellite System Operational Products. Remote Sensing. 2019

An Overview of the Science Performances and Calibration/Validation of Joint Polar Satellite System Operational Products

Lihang Zhou[1,*], Murty Divakarla[2], Xingpin Liu[2], Arron Layns[3], and Mitch Goldberg[3]

[1] NOAA/NESDIS Center for Satellite Applications and Research (STAR), 5830 University Research Court, MD 20740, USA

[2] IM Systems Group, Inc., 3206 Tower Oaks, Blvd., Suite 300, Rockville, MD 20852, USA

[3] NOAA JPSS Program Office, Lanham, MD 20706, USA

* Correspondence: Lihang.Zhou@noaa.gov

Received: date; Accepted: date; Published: date

Abstract: The Suomi National Polar-orbiting Partnership (S-NPP) satellite, launched in October 2011, initiated a series of the next generation weather satellites for the National Oceanic and Atmospheric Administration (NOAA) Joint Polar Satellite System (JPSS) program. The JPSS program at the Center for Satellite Applications and Research (JSTAR) leads the development of the algorithms, Calibration, and Validation of the products to meet specified requirements, and long-term science performance monitoring and maintenance. All of the S-NPP products have been validated and are in successful operations. The recently launched JPSS-1 (renamed as NOAA-20) satellite is producing high quality data products that have been available from S-NPP along with additional products as a direct result of the instrument upgrades and science improvements. This paper presents an overview of the JPSS product suite, the performance metrics achieved for the S-NPP, and utilization of the products by NOAA stakeholders and user agencies worldwide. Status of NOAA-20 science data products and ongoing calibration/validation (Cal/Val) efforts are discussed for user awareness. In addition, operational implementation statuses of JPSS enterprise (multisensor and multiplatform) science algorithms for product generation and science product reprocessing efforts for the S-NPP mission are discussed.

Key Words: JPSS, NOAA-20, S-NPP, Cal/Val, JSTAR, L1RDS

1. Introduction

The Joint Polar Satellite System (JPSS) is the National Oceanic and Atmospheric Administration's (NOAA) operational program that provides continuity of global environmental data from multiple polar-orbiting satellites. The Suomi National Polar-orbiting Partnership (S-NPP) satellite, launched in October 2011, was the first JPSS satellite and serves as the predecessor to the JPSS-1 satellite (renamed as NOAA-20 after being handed over to NOAA for operations). NOAA-20 was launched on November 18, 2017. The S-NPP satellite, orbiting in a 1:30 AM/PM polar orbit, has been extremely successful in operations for the last seven years and has produced an array of high-quality products in the areas of atmospheric, land, ocean, and cryosphere data products. These products are built on measurements from five major instruments: the Visible Infrared Imaging Radiometer Suite (VIIRS), the Cross-track Infrared Sounder (CrIS), the Advanced Technology Microwave Sounder (ATMS), the Ozone Mapping and Profiler Suite (OMPS) and Clouds and

the Earth's Radiant Energy System (CERES) [1]. The NOAA-20 satellite is also in 1:30AM/PM orbit with a 50-minute separation from the S-NPP orbit. NOAA-20 features five similar instrument complements currently operating on S-NPP and provides continuity of the high-quality data products along with additional products as a direct result of instrument upgrades and science improvements. The JPSS-2 and the Polar Follow-On (PFO) satellites (JPSS-3, JPSS-4) will continue to host similar instrument complements for long-term consistent science products. The JPSS program also supplements these datasets with long-term agreements with the European Organisation for the Exploitation of Meteorological Satellites (EUMETSAT), the Japan Aerospace Exploration Agency (JAXA), and other international agencies to provide increased temporal and spatial coverages and types of satellite products. The JPSS constellation of polar-orbiting satellites provide a diverse set of ultraviolet (UV), visible and near infrared (VIS/NIR), infrared (IR), and microwave (MW) sensors and essential observations for many important applications for operational weather forecasting, environmental monitoring, and climate research.

The JPSS program at the center for SaTellite Applications and Research (JSTAR) led the development and calibration/validation (Cal/Val) of JPSS science algorithms to generate a vast number of products [2], which are operationally available to NOAA stakeholders and users worldwide through the NOAA Product Distribution and Access (PDA), Comprehensive Large Array-data Stewardship System (CLASS, [3]), and Direct Broadcast (DB), respectively. JSTAR includes a large team of scientists and engineers from government, academia, and industry. Details on the JPSS algorithms, performance, team leads and members, and data product access are available at the JSTAR website [4].

The S-NPP products served as a gateway to introduce algorithm upgrades and mitigations during the pre-launch phase of NOAA-20. Accounting to the lessons learned through S-NPP product operationalization and based on pre-launch characterization of the NOAA-20 instruments, the JSTAR teams developed necessary algorithm upgrades and mitigations to ensure NOAA-20 data product readiness. The JSTAR teams also developed the NOAA-20 Cal/Val plans for use during the Early Orbit Checkout (EOC), Intensive Cal/Val (ICV) and Long-Term Monitoring (LTM) phases for the NOAA-20 data products. The Integrated Calibration and Validation System (ICVS) and the Long Term Monitoring System (LTM) developed for S-NPP have been augmented to NOAA-20 for spacecraft/sensor health and satellite product display/monitoring. The JSTAR teams are currently focusing on NOAA-20 data product Cal/Val and performance evaluation. The generation and dissemination of the NOAA-20 satellite products follow the same protocols as the S-NPP.

One of the major strengths of polar-orbiting satellites is the collection of global observations needed for the Numerical Weather Prediction (NWP) assimilations worldwide. CrIS and ATMS observations are assimilated into NWP models on a routine basis and have been found to improve 5-7 day forecasts and hurricane track predictions [1]. In fact, 85% of all data assimilated into forecast models are from infrared and microwave sounders on polar orbiting satellites contributing to about 60% of forecast error reduction [5, 6]. The availability of two down-link stations (Svalbard and McMurdo) for NOAA-20 coupled with the implementation of Community Satellite Processing Packages (CSPP, [7]) implemented at the DB network of stations enables improved latency for many real-time applications [8]. The S-NPP and NOAA-20 satellite data products have been proven to be invaluable over the data-sparse polar regions [9]. To complement these data products, the JPSS Program Science Office has established the Proving Ground and Risk Reduction (PGRR) Program [10] initiatives to address data needs for near-real-time (NRT) applications and retrospective evaluations across NOAA line offices and other user agencies. The JSTAR teams have developed plans for enterprise algorithms approach for S-NPP and NOAA-20 and future mission data processing. Enterprise algorithms use the same scientific methodology and software base to create the same classification of product from differing input data (e.g. satellite, in-situ, ancillary) [11]. The teams have also made significant progress in the mission-long reprocessing of S-NPP data products generated using the most matured algorithms to achieve long-term consistency of data product quality.

In this paper, we present an overview of the JPSS product suite, its validation results for the SNPP products and science applications. We briefly introduce the status of NOAA-20 science products and ongoing Cal/Val efforts. In addition, the operational implementation statuses of JPSS enterprise science algorithms for product generation and science product reprocessing efforts for the S-NPP mission are discussed.

2. JPSS Science Data Products, Cal/Val, and Algorithm Management

2.1 *Science Data Products*

The JPSS data products include Temperature Data Records (TDRs), Sensor Data Records (SDRs), and Environmental Data Records (EDRs). Raw Data Records (RDRs) refer to the raw data generated by the sensors on the satellites. Science algorithms that perform calibration and geo-location are applied on the RDRs to produce geo-located, radiometrically and spectrally calibrated radiances (or reflectance) with annotated quality indicators to generate SDRs and TDRs. EDRs are geophysical parameters that are derived by applying retrieval algorithms to the SDRs. EDRs provide global measurements of quantities, such as temperature and moisture profiles, ozone and trace gases, aerosols, clouds, wind speeds, land surface properties, snow and ice cover, sea surface temperature, ocean color, and other products.

Fig. 1 shows a list of the JPSS TDR, SDR, and EDR operational products (hereafter referred as xDRs). The NESDIS operational EDR products derived from Global Change Observation Mission-Water (GCOM-W)/JAXA are also part of the JPSS product suite. Based on the utility of these science data products by customers and user community, ATMS TDRs, CrIS SDRs, and some of the VIIRS imagery EDRs are prioritized as Key Performance Parameters (KPPs). The remaining are prioritized as priority 2, 3, and 4 products. Documents, such as the Algorithm Theoretical Basis Documents (ATBDs), Cal/Val Plans, algorithm requirements and status documents, user guides and other science documents related to all of the SDR/EDR products are available at the JSTAR website [4]. The SDRs and imagery EDR products identified as Mission Unique Products are produced at the Interface Data Processing Segment (IDPS). The other EDRs are produced at the NOAA Data Exploitation (NDE) using enterprise algorithms.

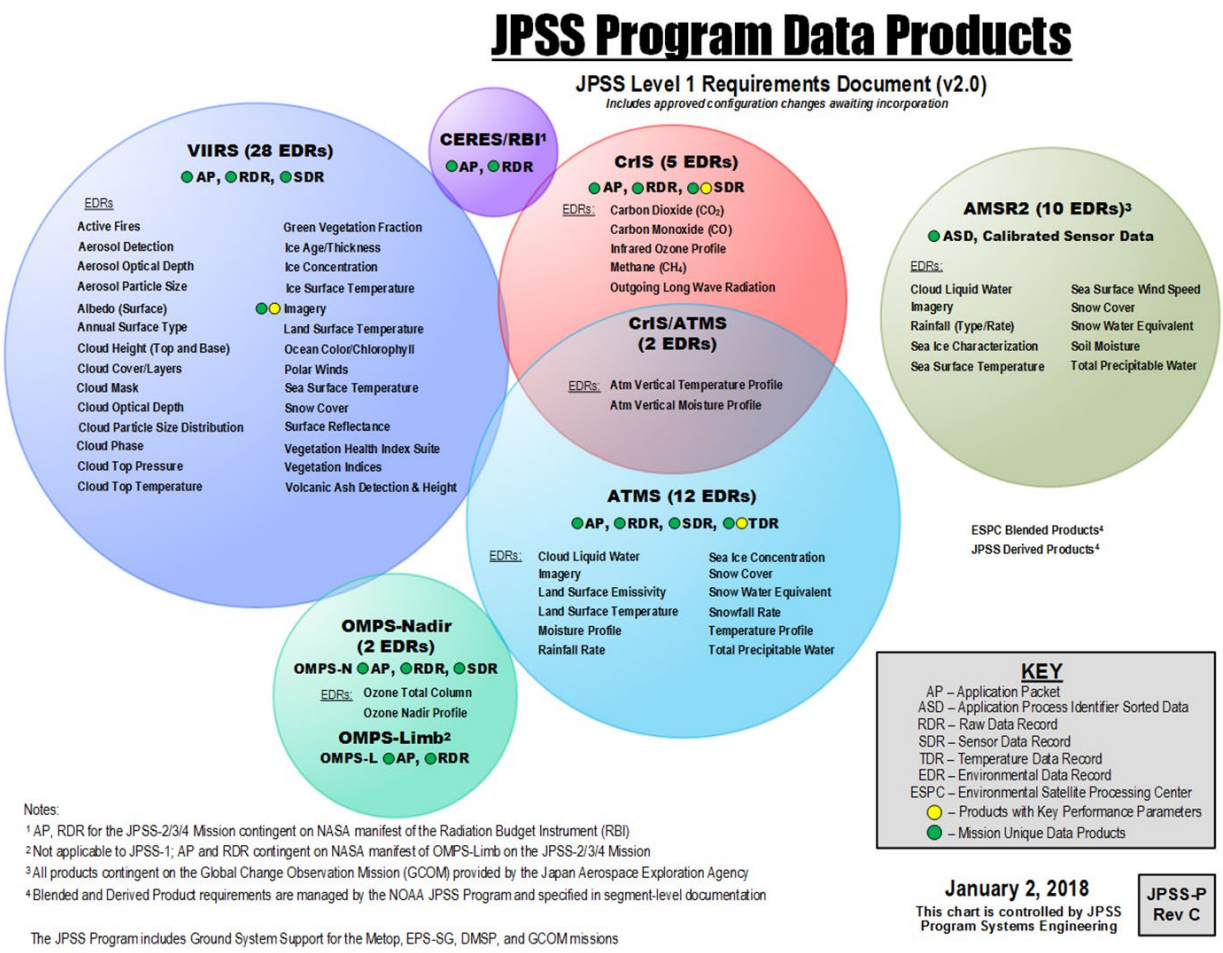

Fig. 1. Sensor and Environmental Data (xDR) products from the S-NPP/NOAA-20/GCOM-W1 instruments suite.

2.2 *Science Data Products Calibration and Validation (Cal/Val)*

For each JPSS satellite mission (S-NPP, NOAA-20, and future missions), the JSTAR SDR/EDR Cal/Val activities are planned and executed for all Cal/Val phases: pre-launch, EOC, ICV, and LTM [2]. The major objective is to evaluate and ensure that the operational SDR/EDRs meet Beta, Provisional, and Validated maturity requirements [4]. Beta maturity designates an early release product that is minimally validated and may have significant errors. The beta product is made available to users to gain familiarity to the data format. Provisional maturity indicates that the product is deemed ready for operational evaluation. Versioning control commences as the product continues to undergo improvements, and user participation in quality assurance is encouraged. Validated maturity occurs when the product performance is well-defined over a range of representative conditions using a widely distributed set of statistically robust independent measurements (from many locations and time periods) representing global conditions. Each product's Cal/Val maturity is determined by validating the algorithm's performance with truth data sets and comparing the performance with the requirements. Details of various Cal/Val tasks for each xDR product as well as the roles and responsibilities of team members are discussed in xDR-specific Cal/Val plan documents [4].

Product validation maturity reviews are performed by review panels comprised of JPSS Program and Project Scientists, NOAA customers (National Weather Service, NWS; National Ocean Service, NOS; National Marine Fisheries Service, NMFS; Office of Oceanic and Atmospheric Research, OAR), external

users, Low-earth Orbiting Working Group (LORWG) advisors, product development managers, and the JSTAR program manager. Following the Cal/Val maturity science reviews presented by the Cal/Val teams, the review board assesses the product performance, makes an overall assessment of each algorithm, and approves the maturity status according to the criteria for Beta, Provisional, and Validated Maturity. Currently, most S-NPP data products have passed the Cal/Val validation maturity stages and are in the LTM phase. The NOAA-20 data products are going through the Cal/Val maturity according to the Cal/Val plans.

The next section provides comprehensive details of the S-NPP product performance. The preliminary results of NOAA-20 product performance are discussed in Section 4.

3. S-NPP Science Data Product Performance

The JSTAR science teams have performed Cal/Val for the S-NPP SDR and EDR products from the four major instruments: VIIRS, CrIS, ATMS, and OMPS. The Cal/Val efforts validating these products have been published as a compendium of scientific papers by the Journal of Geophysical Research [12] and as individual publications [13-17]. The wide variety of EDR products generated from the S-NPP sensor suite have passed Validated maturity stage and have been proven to be very useful for many atmosphere, land, ocean, and cryosphere applications. Most of the S-NPP EDR products have also been migrated to enterprise algorithms and many of them are in operations at NDE. The following sub-sections provide details of the S-NPP product performance evaluations and science applications for each of the four S-NPP instruments. Product performance summarized in the tables are compiled from the S-NPP/NOAA-20 product maturity review presentations, or from past years' STAR JPSS Annual Science Meeting presentations. These presentations are available online at JSTAR website [4].

3.1 *The VIIRS instrument and Science Data Products*

The VIIRS instrument onboard the S-NPP/NOAA-20 satellites has transitioned much of the capability of the experimental MODerate Resolution Imaging Spectroradiometer (MODIS) instrument into the operational domain. The instrument offers a total of 21 (plus one Day Night Band, DNB [18]) bands with similar central wavelengths to MODIS [19] and similar radiometric accuracy [20-22]. The VIIRS instrument also provides better spatial resolution (375m for the Imaging-resolution or I-band and 750m for Moderate-resolution or M-bands at nadir) and reduced variation over the 3000 km wide swath. Further, the availability of the DNB offers a wide variety of applications [23, 24] and makes the VIIRS JPSS products vital for long-term continuity with greater operational utility.

The S-NPP VIIRS instrument produces more than 20 EDR products and most of the data products have been validated with various truth data sets and the product performances have been verified with the Level-1 Requirement Document Supplement (L1RDS, [25]) requirements for progression through the Beta, Provisional, and Validated Maturity stages. Table 1 summarizes the S-NPP VIIRS SDR performance meeting the Accuracy, Precision, and Uncertainty (APU) specifications [14, 21, 26, 27]. A compendium of scientific papers published by the Remote Sensing journal (edited by Changyong Cao, [28]) provides complete details of the VIIRS science data products and Cal/Val assessments.

Table 1. S-NPP VIIRS SDR performance meeting the specifications

Band		Center Wavelength (nm)	Specification SNR (RSB & DNB) NEDT (TEB)*	Performance (on-orbit)
RSB	**M1**	412	316, 352 (LG,HG)	1045, 588
	M2	445	409, 380 (LG,HG)	1010, 572
	M3	488	414, 416 (LG,HG)	988, 628
	M4	555	315, 362 (LG,HG)	856, 534
	M5	672	360, 242 (LG,HG)	631, 336
	M6	746	199	368

	M7	865	340, 215 (LG,HG)	631, 457
	M8	1240	74	221
	M9	1378	83	227
	M10	1610	342	586
	M11	2250	90	22
	I1	640	119	214
	I2	865	150	264
	I3	1610	6	149
	M12	3700	0.396	0.12
	M13	4050	0.107	0.04
	M14	8550	0.091	0.06
TEB	**M15**	10763	0.07	0.03
	M16	12013	0.072	0.03
	I4	3740	2.5	0.4
	I5	11450	1.5	0.4
DNB	**DNB**	700	6	> 10

* Signal-to-noise ratios (SNR) or noise-equivalent Temperature Differences (NEDT) for Reflective Solar Bands (RSB), and Thermal Emissive Bands (TEBs). Radiometric biases for the reflective solar bands are within 2% of MODIS equivalent bands, after bias correction with extensive validation. For the thermal emissive bands, bias is within 0.1K relative to CrIS on the same spacecraft.

The VIIRS SDRs and imagery EDR products designated as KPPs have been vital to the success of the S-NPP/NOAA-20 missions. The imagery EDR products are comprised of five Imaging-resolution or I-band (375m resolution) products, six Moderate-resolution or M-band (750m resolution) products, and Near Constant Contrast (NCC) Imagery derived at 750 m resolution from the DNB sensor [29]. The Alaska region and other high-latitude regions benefit from overlapping swaths from adjacent orbits, which enables the derivation of polar winds products and many cryosphere product composites. VIIRS imagery applications in meteorological operations over the Alaska region are discussed in detail by Don Hillger et al [9]. In addition to the high-latitude applications, the VIIRS imagery products are being used for nowcasting of severe weather, such as hurricanes and blizzards days in advance and for assessing environmental hazards, such as droughts, floods, forest fires, poor air quality, and harmful coastal waters [30]. Fig. 2 shows the VIIRS imagery product and combined use of the infrared and Day/Night band imageries. Moonlight provides a means to peering through cirrus clouds, which are optically thin at visible light wavelengths. This enabled the VIIRS Day/Night band to detect low cloud structures that revealed the true center of low-level circulation associated with Hurricane Flossie. The DNB has been proved to be useful for many applications including tropical cyclone analysis and forecasting, night fire products, nighttime aerosol retrievals, mapping of city lights/power outage detection, boat detections, and detection of airglow gravity waves, among other events [31-36].

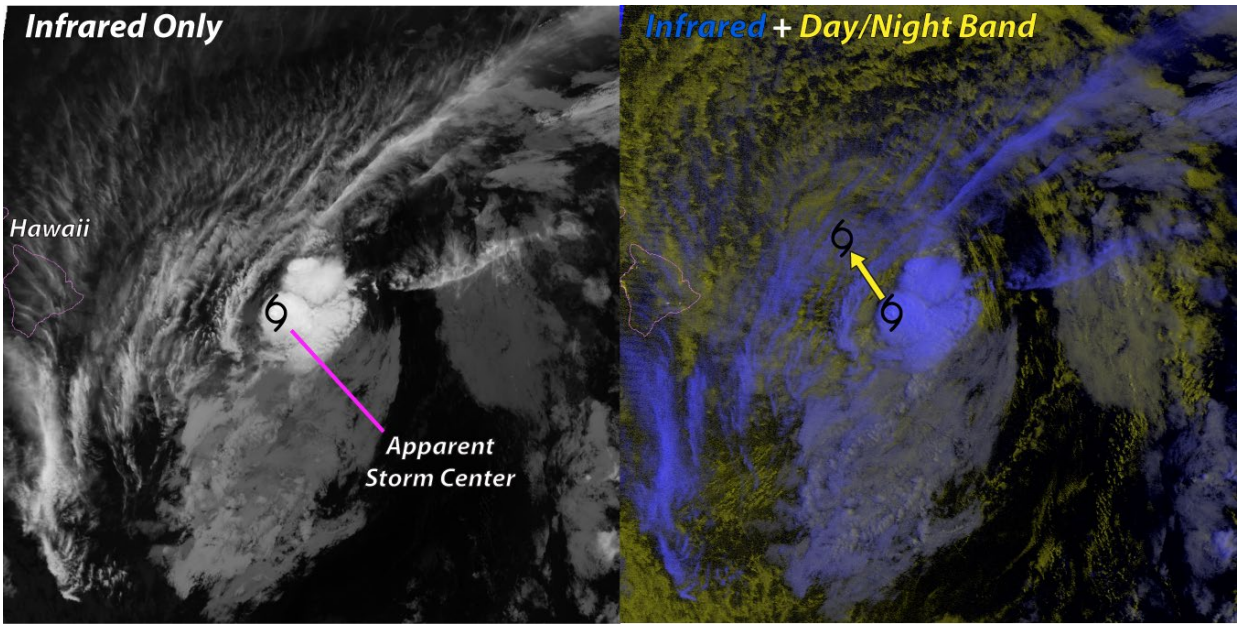

Fig. 2. Nocturnal Tropical Cyclone tracking using VIIRS IR and DNB band, as presented on S-NPP VIIRS Imagery Validated Maturity Review by JSTAR Imagery EDR Team (Don Hillger et al. 2014, https://www.star.nesdis.noaa.gov/jpss/documents/AMM/Imagery_Val.pdf)

In addition to the EDR imagery products, the VIIRS product suite contains a wide variety of geophysical products (i.e., EDRs), include those for atmosphere (e.g. aerosol optical thickness, AOT; aerosol detection products, ADP), land (e.g. variety of vegetation indices, VI; green vegetation fraction, GVF; land surface temperature, LST), ocean (e.g. sea surface temperature, SST; ocean color, OC), and cryosphere (e.g. ice surface temperature, IST; sea ice thickness, concentration; snow fraction, polar winds). Many of these products use the enterprise VIIRS cloud mask (ECM), which is based on heritage from the Advanced Very High Resolution Radiometer (AVHRR) Pathfinder Atmospheres Extended (PATMOS-x) and naïve Bayesian approach [37, 38]. The ECM has been applied to multiple sensors (e.g. AVHRR, Geostationary Operational Environment Satellite, GOES-16 Advanced Baseline Imager, ABI), and the cloud products have been tested against the Cloud-Aerosol Lidar and Infrared Pathfinder Satellite Observation (CALIPSO) and MODIS cloud mask (MYD25) products [39, 40]. The primary output from the ECM is cloud probability and a 4-level cloud mask derived solely from the cloud probability. In addition, the enterprise cloud algorithm uses a set of seven algorithms to produce a full suite of cloud products, such as cloud phase/type, cloud top/base height, cloud top temperature, cloud top pressure, cloud optical depths, particle sizes, and cloud water path. The VIIRS ECM cloud products are provided to NWS Aviation Weather Center for global monitoring of aviation hazards [41]. NOAA OAR uses the cloud-product information for model verification over Polar Regions, and cloud height information is used in deriving polar atmospheric motion vectors [42, 43]. The ECM and cloud height are used in resolving some of the artifacts in the CrIS clear radiance for NWP data assimilations [42, 44]. Fig. 3 shows an example of the VIIRS daytime cloud-mask derived from the NOAA enterprise cloud product algorithm. The enterprise cloud products performance are provided in Table 2, Table 3, and Table 4.

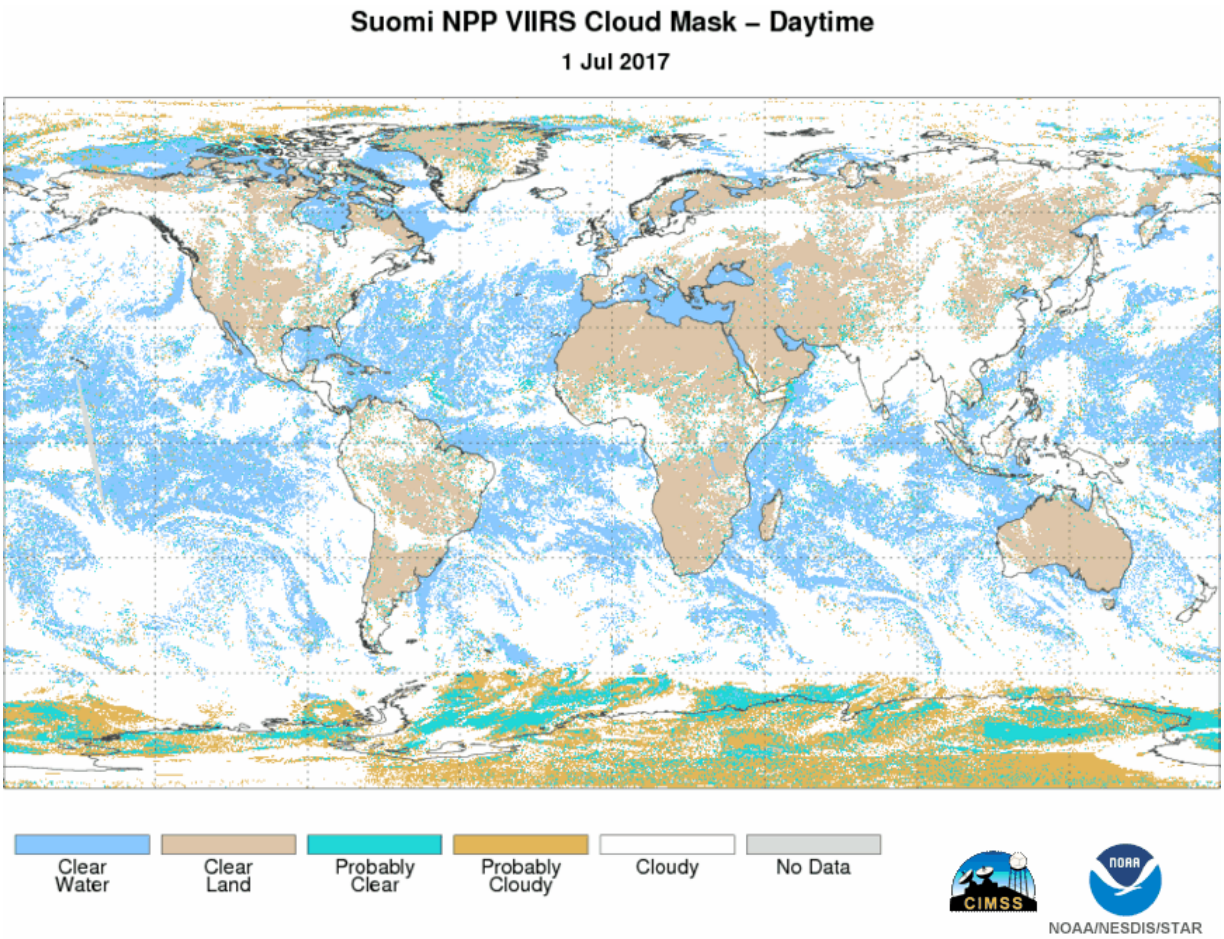

Fig. 3. An example of VIIRS daytime cloud mask generated using the VIIRS enterprise cloud algorithm (Fig. Courtesy: Andy Heidinger, NOAA)

Table 2. S-NPP VIIRS Cloud Mask Performance versus specifications*

	Ocean	Snow-Free Land	Desert	Snow-Covered Land	Sea Ice	Antarctic and Greenland
Global			0.888 (0.87)			
Day	0.95 (0.92)	0.912 (0.90)	0.864 (0.85)	0.896 (0.88)	0.908 (0.82)	0.741 (0.80)
Night	0.912 (0.90)	0.883 (0.88)	0.858 (0.85)	0.878 (0.85)	0.799 (0.72)	0.701 (0.70)

* Product performance and specification data (in parenthesis) summarized in the table are obtained from the Enterprise Clouds Algorithms Readiness Review presented on December 15, 2015.

Table 3. S-NPP VIIRS Cloud Products Performance (Accuracy: Magnitude of the mean measurement errors; Precision: The standard deviation of the measurement errors [27])

Product	Requirement		Performance	
Cloud Phase				
- **% correct classification**	80%		> 82.6%	
Cloud Type				
- **% correct classification**	60%		> 72.6%	
	Accuracy	**Precision**	**Accuracy**	**Precision**
Cloud Base Height	2 km	2 km	0.3 km	1.7 km
Cloud Optical Depth	2 or 20%	3 or 30%	1.59/0.9%	4.43/25.7%
- **Day, Water**	2 or 20%	3 or 30%	1.81/3.6%	5.02/31.1%

- **Day, Ice**	30%	0.8 or 30%	-0.12/7.3%	0.63
- **Night**				
Cloud Particle Size				
- **Water**	4 μm	4 μm	3.03 μm	4.30 μm
- **Ice**	10 μm	10 μm	5.69 μm	5.23 μm

Table 4. S-NPP VIIRS Cloud Top Products Performance

Product	Type	Bias	STD	Within the specified Accuracy	Within the specified Precision
CTH – Cloud Top Height	All Clouds	-0.3 km	1.26 km	81.9%	82.3%
	Water	-0.02 km	0.80 km	90.7%	90.8%
	Ice	-0.87 km	1.74 km	64.5%	65.7%
CTT – Cloud Top Temperature	All Clouds	1.65 K	9.08 K	51.2%	36.3%
	Water	-0.51 K	4.08 K	70.4%	74.5%
	Ice	4.03 K	12.02 K	29.8 %	24.2 %
CTP – Cloud Top Pressure	All Clouds	-11.0 hPa	95.7 hPa	80.9%	80.1%
	Water	8.8 hPa	68.8 hPa	89.6%	89.4%
	Ice	-28.6 hPa	111.6 hPa	73.2%	63.7%

A suite of land products (e.g. surface reflectance, VIIRS vegetation, surface albedo, land surface temperature, surface type, and active fire products) is derived from the VIIRS instrument channels. These products are used for a wide variety of applications, including land use management and monitoring, ecosystem dynamics, atmospheric chemistry, human health, biomass burning emissions, operational air quality forecasting, etc. [45-47]. All S-NPP land products have met the maturity requirements (Table 5) and have been declared validated, and many have been transitioned to enterprise algorithms for NDE operations.

Table 5. S-NPP VIIRS Land Products Performance

Product	Requirement		Performance	
Global Gridded Surface Type				
- **% correct typing**	70%		77.6 ± 0.6%	
	Accuracy	**Precision**	**Accuracy**	**Precision**
Land Surface Temperature	1.4 K	2.5 K	-0.08 K	2.26 K
Surface Albedo	0.08	0.05	-0.005	0.05
Surface Reflectance *	0.005+0.05ϱ	0.005+0.05ϱ	-0.00560	0.00563
Green Vegetation Fraction **				
- **Global**	12 %	15%	8%	8.4%
- **Regional**	12 %	15%	7.1%	7%
Vegetation Index				
- **TOA NDVI**	0.05	0.04	0.013	0.012
- **TOC NDVI**	0.05	0.04	0.012	0.018
- **TOC EVI**	0.05	0.04	0.020	0.011

* **Surface Reflectance:** Better than 0.005+0.05ϱ for M4, M5, M7, I1, I2, I3, M8, M10, M11, shown in table is the Band-5 performance; ϱ denotes the retrieved surface reflectance

** **Green Vegetation Fraction:** Uncertainty Requirement 17%; Product performance: 11.6% for Global, and 10% for Regional

Fig. 4 gives a glimpse into NDE enterprise Vegetation Product Suite (NVPS) that includes a variety of VI products and the GVF product. The GVF product is used for monitoring drought, vegetation health monitoring, crop conditions, and global food supply and demand [47]. The VIIRS VI products are consist of the Normalized Difference Vegetation Index (NDVI) derived from Top-of-the-atmosphere (TOA) reflectances and the Enhanced Vegetation Index (EVI) derived from atmospherically-corrected, top-of-canopy (TOC) reflectances, NDVI from TOC reflectances (an additional product from NOAA-20) [48]. The VIIRS VI and GVF algorithm performance has been evaluated using MODIS products, along with 35 Flux Tower sites providing in-situ data from Earth Observing System (EOS) Land Validation Core sites. The GVF products have been validated with the EOS data sets and Google Earth derived GVF [49]. Other land products are at various stages of operational use in weather and climate forecasting systems (e.g. VIIRS GVF, GCOM Soil Moisture in National Center for Environmental Prediction (NCEP) Land and Coupled Models and High Resolution Rapid Refresh, HRRR models) and are used in crop forecasts generated by the United States Department of Agriculture (USDA, e.g. Vegetation Health and GCOM Soil Moisture in the US Drought Monitor). The main requirement by the end users (e.g. Land Hydrology group) is to have consistent sets of land products delivered on the same grid resolution (e.g. 1 km). Currently, the land product teams are finalizing the technical details of a land product global gridding system that uses pixel level granule products and produces a consistent set of global gridded products at 1 km spatial resolution.

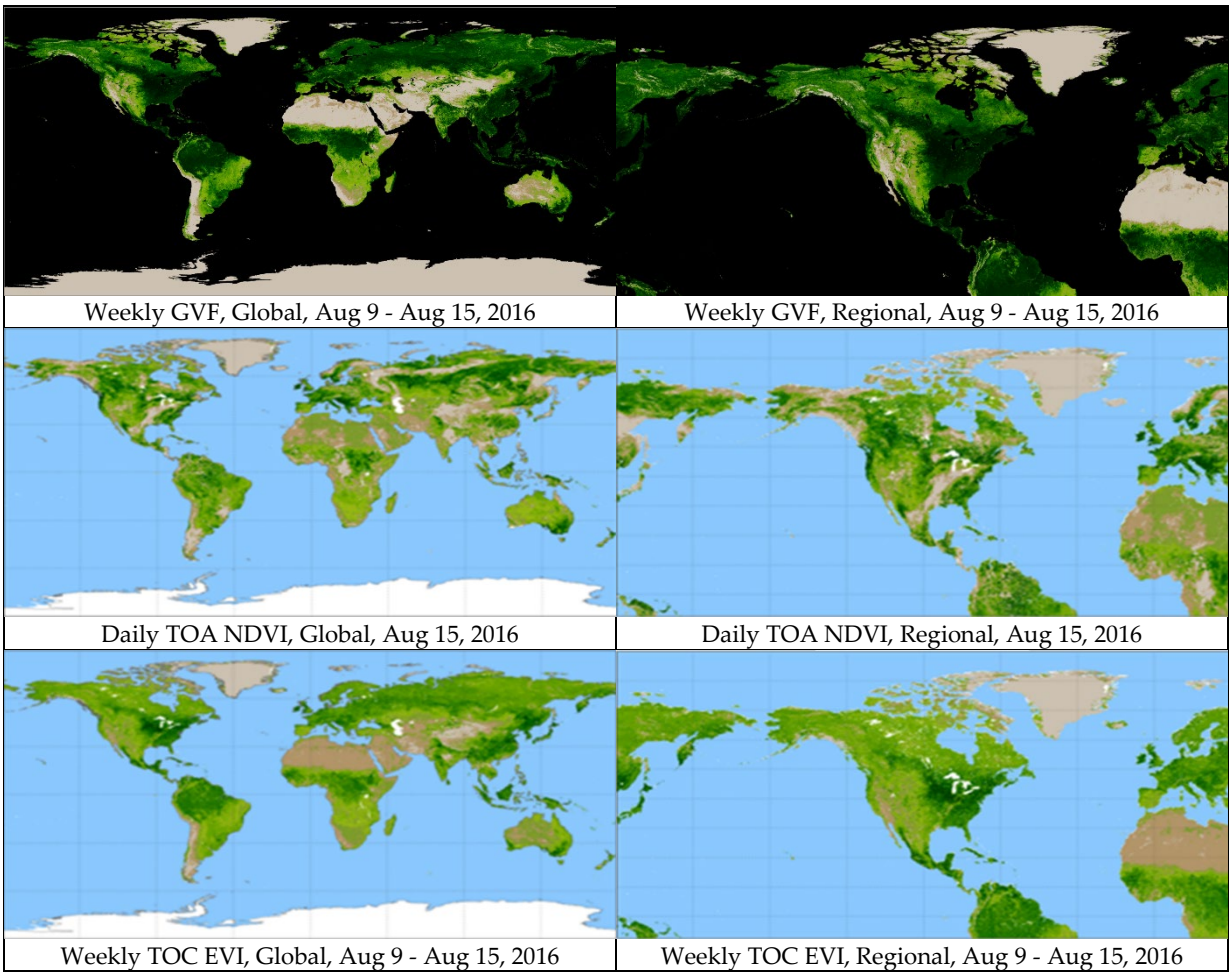

Weekly GVF, Global, Aug 9 - Aug 15, 2016 | Weekly GVF, Regional, Aug 9 - Aug 15, 2016

Daily TOA NDVI, Global, Aug 15, 2016 | Daily TOA NDVI, Regional, Aug 15, 2016

Weekly TOC EVI, Global, Aug 9 - Aug 15, 2016 | Weekly TOC EVI, Regional, Aug 9 - Aug 15, 2016

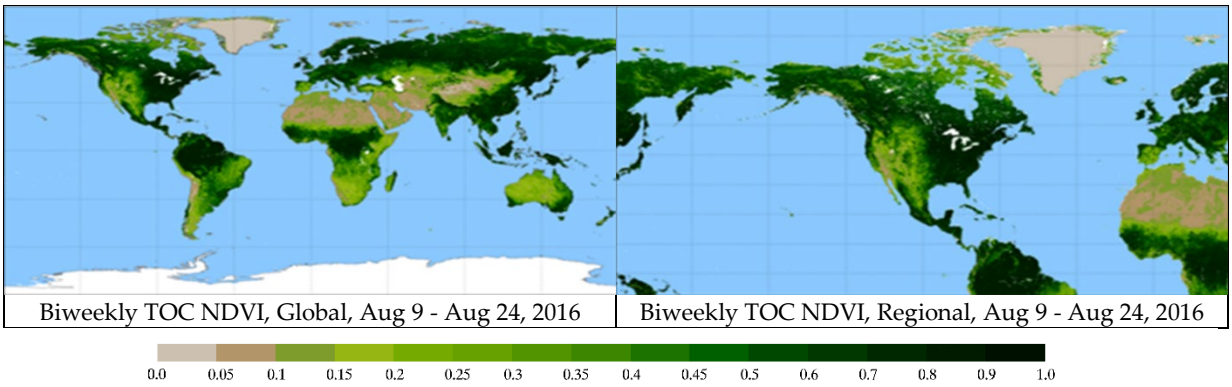

Fig. 4. VIIRS Gridded Vegetation Products. The NDE enterprise Vegetation Product Suite (NVPS) includes a variety of Vegetation Index (VI) products and the GVF product. The product suite contains daily, weekly and biweekly global and regional (North America) products at 4 km and at 1 km spatial resolution, respectively (Fig. Courtesy: Yunyue Yu, STAR VI/GVF team).

A wide variety of ocean data products are derived from the VIIRS instrument. Fig. 5 and Fig. 6 shows two important ocean EDR products, the SST and the ocean color chlorophyll-a (OCC). The SST product is derived using the Advanced Clear-Sky Processor for Ocean (ACSPO) SST algorithm [35, 50, 51]. The algorithm, a regression algorithm trained with in-situ measurements, uses separate sets of VIIRS channels for day and night and retrieves SST at every cloud-free VIIRS pixel. The algorithm produces consistent products from the S-NPP VIIRS, the GOES instruments, as well as NOAA-20 and GOES-16 for many real-time applications. The team also produces a gridded product by mapping the SST EDR product into equal 0.02° grid boxes. The gridded SST product shows comparable performance with SST EDRs, and the product is used by several major international NWP centers. As shown in Fig. 5, the SST produced from GOES-16 (on the left panel) and from SNPP (on the right panel) using the same ACSPO algorithm show consistent features between the two satellite platforms. Whereas the higher temporal resolution of GOES-16 allows better coverage of SST for low and middle latitude, the S-NPP allows global coverage including Polar Regions and higher spatial resolution. In addition to using JPSS and GOES observations, the ACSPO system also brings in non-NOAA satellite SST products to produce global 5 km blended SST products benefitting from both the higher spatial resolutions of polar satellite data and the higher temporal resolution of geostationary satellite data [52].

The VIIRS Ocean Color (OC) products are generated using the NOAA Multi-Sensor Level 1 to Level 2 (MSL12) processing system [53, 54] for both near real-time applications and for science quality applications [55] for incorporation into longer time series needs such as the integrated ecosystem approach for fisheries management applications [56]. JPSS VIIRS OC products are also reprocessed for the best quality mission-long S-NPP OC products to benefit the users worldwide. Fig. 6 shows a five-year climatology of the global distribution of the chlorophyll derived from the reprocessed OC products. Applications of JPSS ocean data products include the use of VIIRS SST products for coral reef watch anomalies, hotspots, and bleaching area alerts [57], and many of these products are distributed through the CoastWatch, OceanWatch, and PolarWatch portals [52, 58]. All S-NPP ocean data products have reached validated maturity and Table 6 shows the APU specifications for these products.

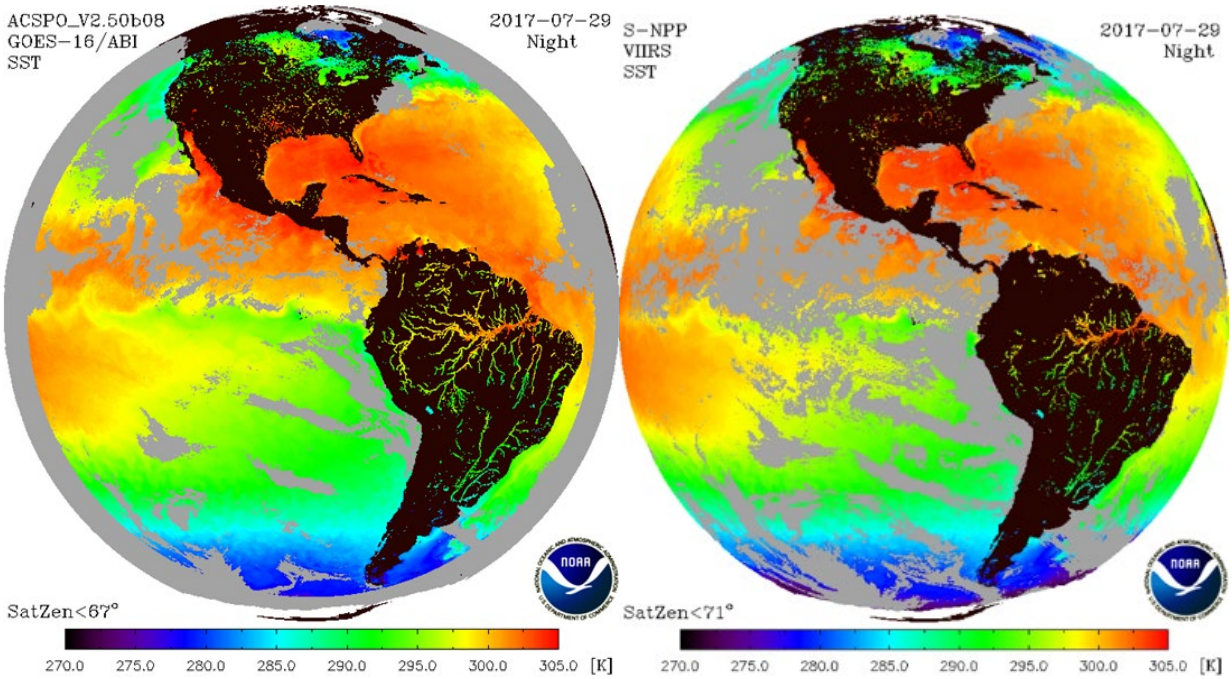

Fig. 5. ACSPO enterprise algorithm produce consistent results when applied on GOES-16 ABI (left) and on the VIIRS (right) for nighttime composites in the same domain. Large areas are cloudy during the S-NPP night overpass at 1:30 am; the GOES-16 ABI nighttime composite picks up more clear areas due to the high temporal resolution (every 15 minutes). The VIIRS SST, on the other hand, provides global coverage, including the Polar Regions. (Fig. Courtesy: Alex Ignatov, STAR SST team)

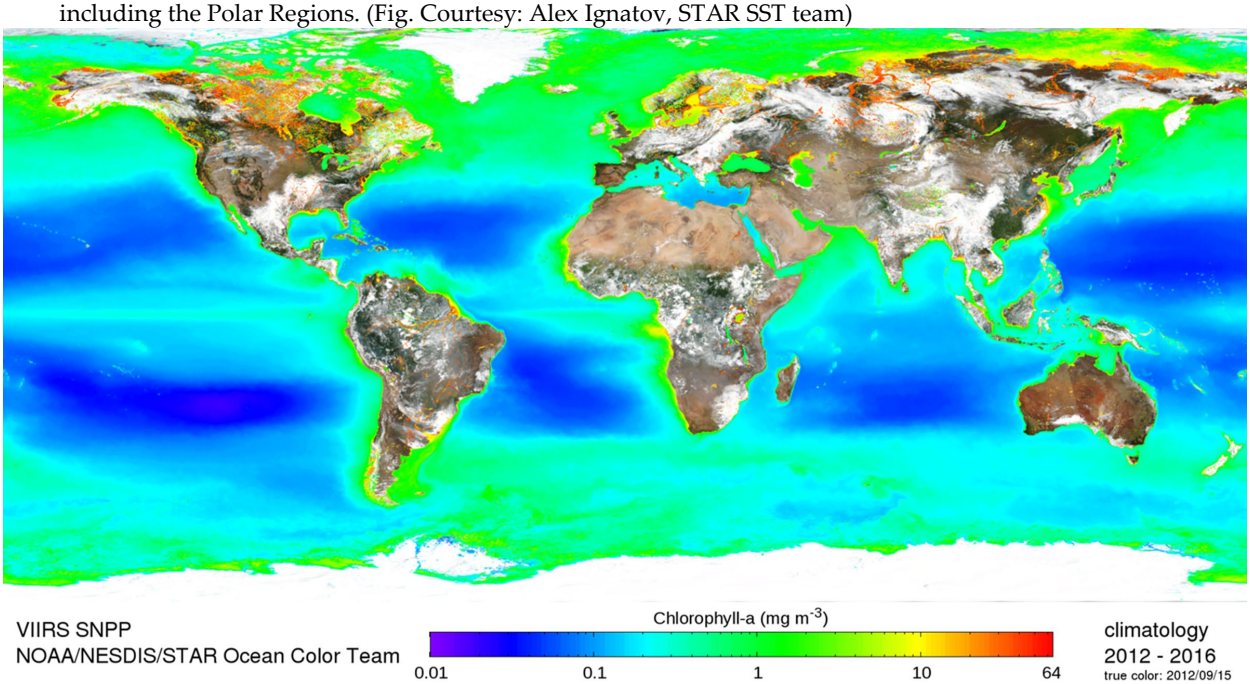

Fig. 6. S-NPP Ocean Color climatology Chl-a (2012-2016). In addition to (MSL12) OC processing system NRT products (meeting latency requirements), the OC team also produces JPSS-VIIRS reprocessed ocean-color products for the best quality mission-long S-NPP OC data products to benefit users worldwide (Fig. Courtesy: Menghua Wang, STAR OC team).

Table 6. S-NPP VIIRS Ocean Products Performance

Product	Requirement	Performance

		Accuracy	Precision	Accuracy	Precision
Ocean Color	**nLw(410)**	10%	10%	1.0153	0.096
	nLw(443)	10%	10%	1.0119	0.092
	nLw(486)	10%	10%	1.0124	0.088
	nLw(551)	10%	10%	1.0098	0.135
	nLw(671)	10%	10%	1.0045	0.498
	Chl-a	30%	30%	1.0016	0.163
Sea Surface Temperature	**Day**	±0.20	0.60	±0.20	0.45
	Night	±0.20	0.60	±0.15	0.35

The VIIRS Atmospheric composition products include aerosol products, namely, (1) the aerosol optical depth (or aerosol optical thickness, AOD, AOT, quantitative measure of aerosol loading) and (2) the aerosol detection product (ADP, qualitative information on the type of aerosol based on MODIS algorithm) [59]. The AOD product from VIIRS is a pixel-level product at a very high resolution. The JSTAR aerosol team has developed the NOAA enterprise processing system (EPS) aerosol algorithm that work for both S-NPP/JPSS and GOES-16. The EPS algorithm implemented at NDE [60-63] requires observed spectral reflectances from a set of VIS and NIR bands and many ancillary data sets. Unlike traditional retrieval algorithms, the AOD algorithm compares the VIIRS observed spectral reflectances for selected VIS and NIR bands with reflectances calculated for a set of AOD and aerosol models. The algorithm then selects the AOD and the aerosol model for which the calculated reflectances best match the observed ones over dark and bright surfaces. The algorithm computes actual exponents at two wavelengths to use as a proxy for the aerosol product itself. The algorithm currently operational for S-NPP meets or exceeds the requirements and has shown improved bias characteristics over the IDPS algorithm and retrieval of the AOD product over an expanded measurement range, including bright surfaces in desert and semi-arid dry regions and over inland water bodies. Many user agencies are using the AOT products for applications, such as air-pollution monitoring and as forecasting.

The ADP enterprise algorithm currently operating on a variety of instruments (S-NPP/NOAA-20 VIIRS, GOES-16 ABI, etc.) identifies volcanic ash, dust, and smoke. The dust and smoke products are based on enterprise algorithms while volcanic ash is a separate algorithm [64]. The volcanic ash algorithm identifies pixels that have ash and estimates ash height and ash loading using an optimal estimation technique. The quality flag associated with the volcanic ash detection is bundled with the ADP product quality flags to identify ash. The ADP product shows about 85% and 92% probability of correct detection for the smoke and dust, good agreement with the Multi-angle Imaging SpectroRadiometer (Fig. 7) and meet the requirements. The ADP enterprise algorithm has been used to reprocess S-NPP VIIRS 2013-2015 data sets to produce dust and smoke climatology. The team is also working on variants of the aerosol products that can tradeoff between data consistency and data latency in order to meet the demands of different users for different applications. Table 7 shows the product performance for the AOD, ADP and Volcanic Ash product.

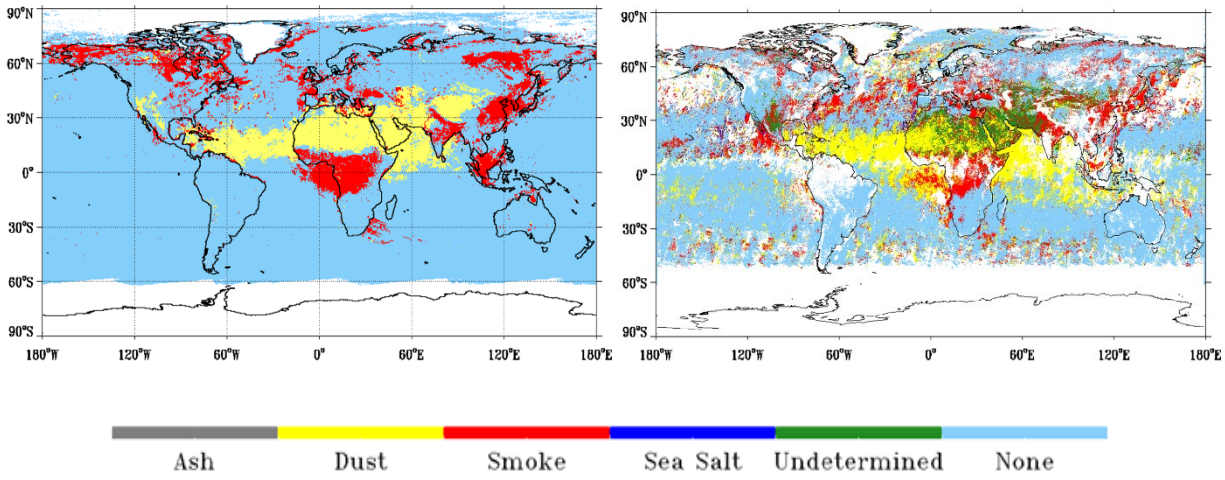

Fig. 7. The VIIRS Aerosol Detection Product (ADP) (left panel) is found to be in good agreement with Multiangle Imaging Spectroradiometer (MISR) (right panel), with respect the location of dust and smoke. The ADP enterprise algorithm is currently running on S-NPP (NDE) and meets the performance requirements (Fig. Courtesy: Shobha Kondragunta/Istvan Laszlo, STAR Aerosol team).

Table 7. S-NPP VIIRS Atmosphere Products Performance

Product	Requirement		Performance	
Aerosol Detection (%)				
- **% correct typing, Smoke**	80		84.7	
- **% correct typing, Dust**	70		92.6	
	Accuracy	**Precision**	**Accuracy**	**Precision**
Aerosol Optical Depth				
- **Land: AOD < 0.1**	0.06	0.15	0.01	0.05
- **Land: 0.1 ≤ AOD ≤ 0.8**	0.05	0.25	-0.04	0.11
- **Land: AOD > 0.8**	0.20	0.45	-0.19	0.34
- **Water: AOD < 0.3**	0.08	0.15	0.02	0.04
- **Water: AOD >= 0.3**	0.15	0.35	-0.01	0.11
Aerosol Particle Size				
- **550/860 μm, Ocean**	0.3	0.6	0.07	0.39
- **865/1610 μm, Ocean**	0.3	0.6	-0.04	0.33
Volcanic Ash				
- **Height**	3 km		-1.91 km	1.37 km
- **Mass Loading**	2 tons/km^2	2.5 tons/km^2	1.13 tons/km^2	1.40 tons/km^2

The VIIRS active fire (AF) land product, used together with the aerosol products, has the heritage of the MODIS Collection 4 version of the algorithm [46, 65, 66] and is an operational M-band product at 750m resolution identifying fire hot spots or cloudy conditions over either land or water. The AF product also provides the fire radiative power (FRP), a proxy for the intensity of fire, for each fire pixel. The NOAA JSTAR team is also evaluating an experimental/research AF product at I/M-band 375m resolution, and validation of this experimental product is planned via campaigns of opportunities. Fig. 8 shows an example of the AF products for the King Fire in CA in September 2014 with VIIRS fire product in the middle panel for 750 m resolution, the right panel for 375 m resolution, and MODIS (1 km) fire product in the left panel. The VIIRS fire data product and the MODIS fire data products show good agreement, and the higher spatial resolution VIIRS product shows higher number of detections, improved mapping capability, and higher fidelity needed for near real-time alert systems.

The S-NPP NDE AF algorithm has been in operations since March 2016. The team is currently optimizing the 375m enterprise algorithm product that combines the advantages of high spatial resolution I-band data with the good radiometric signal of M-band for FRP. The aerosol products and the AF products are used routinely for estimating bio-mass burning emissions and operational air quality forecasting [67]. These products are provided to many users, such as the High Resolution Rapid Refresh (HRRR) and the blended Global Biomass Burning Emissions Product (GBBEPx) [68] with imagery and integrated air quality analysis tools available through the Enhanced Infusing Satellite Data into Environmental Applications (eIDEA) website [69], which blends polar and geostationary fire hot spot data for real-time information.

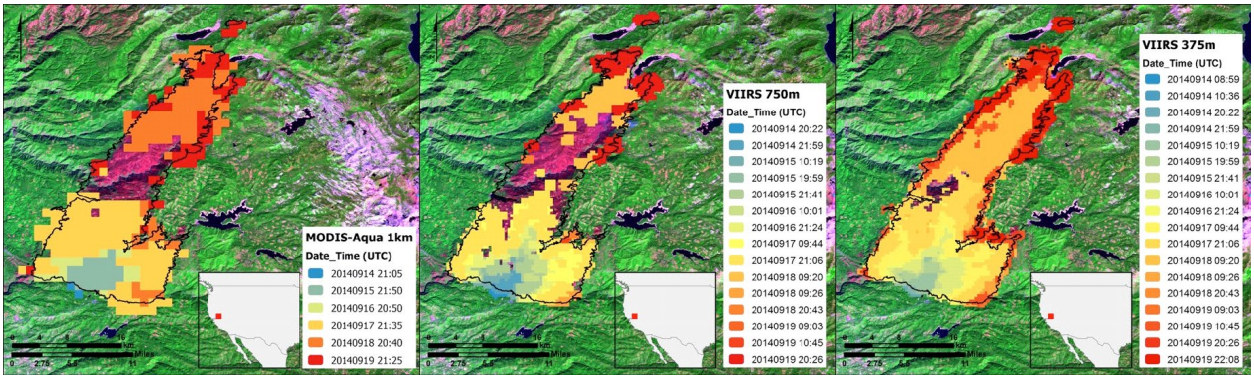

Fig. 8. The VIIRS Active Fire Product (middle panel for 750m and right panel for 375m) and comparison with MODIS (left panel) King Fire, CA/September 2014. This higher spatial resolution VIIRS product shows higher number of detections, improved mapping capability, and higher fidelity needed for near real-time alerts (Fig. Courtesy: Ivan Csiszar, STAR Active Fire Team).

The VIIRS operational cryosphere products [70-73] include two snow products (binary snow cover and snow fraction) and three ice products (ice surface temperature, ice concentration, and ice thickness/age) as shown in Fig. 9. The VIIRS polar winds product is also considered to be part of the cryosphere products. As part of JPSS, the GCOM Advanced Microwave Scanning Radiometer-2 (AMSR2) instrument (see section 3.4) also provides three snow products (snow cover, snow depth, and snow water equivalent) and two sea ice products (sea ice concentration and sea ice type). These products are operational and meet accuracy and precision requirements (Table 8).

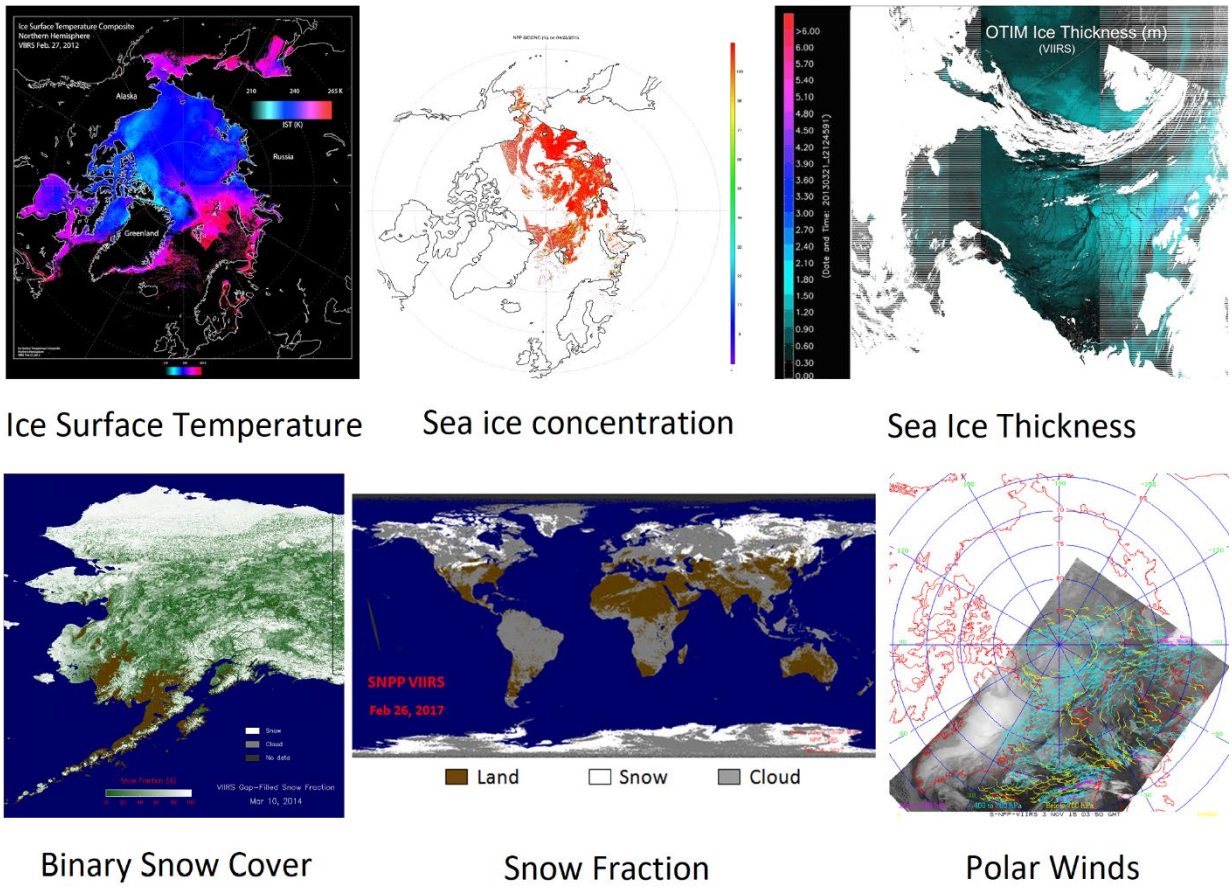

Fig. 9. The VIIRS Cryosphere products are all operationally produced from the S-NPP and meet APU requirements (Fig. Courtesy: Jeff Key, STAR Cryosphere team).

Table 8. S-NPP VIIRS Cryosphere Products Performance

Product	Requirement		Performance	
Snow Cover				
- **Binary Map: % correct typing**	90%		93-94%	
- **Snow Fraction: uncertainty**	20%		~17%	
Sea Ice				
- **Ice Surface Temperature: uncertainty**	1 K		0.9 K	
- **Ice Concentration: uncertainty**	10%		8.9%	
- **Ice Age: % correct typing**	70%		90% (first-year/other)	
	Accuracy	**Precision**	**Accuracy**	**Precision**
Ice Thickness				0.5 m
VIIRS Polar Winds	7.5 m/s	3.8 m/s	5.79 m/s	3.58 m/s

In addition to the products overviewed in this paper, there are more VIIRS EDR products, and the JSTAR website provides a complete description as well as evaluations.

3.2 *The CrIS/ATMS Instruments and Science Data Products*

The CrIS and the ATMS instruments provide IR and MW radiance products (SDRs) for assimilation into the NWP models and have shown considerable impact in reducing medium range forecast errors [1, 74, 75]. In addition to NWP model assimilations, radiance observations from the CrIS and ATMS are used individually and together in the sounding product retrieval algorithms to derive a wide variety of surface

and atmospheric sounding products (EDRs) for many atmospheric applications. Many of these EDR products are ingested into the Advanced Weather Interactive Processing System (AWIPS-2 [76]), and Weather Forecasting Offices (WFOs) nationwide utilize these products for analyzing atmospheric instabilities, potential outbreaks of severe weather, and in now-casting applications [77].

The CrIS instrument aboard the S-NPP/NOAA-20 is a Fourier Transform Spectrometer (FTS) instrument with channels in three bands covering longwave (LWIR, 650–1095 cm^{-1}), midwave (MWIR, 1210–1750 cm^{-1}), and shortwave (SWIR 2155–2550 cm^{-1}) bands [78]. The instrument is similar to other hyperspectral IR sounding instruments, such as the Infrared Atmospheric Sounding Interferometer (IASI, [79]) and the Atmospheric Infrared Sounder (AIRS, [80, 81]).

The Advanced Technology Microwave Sounder (ATMS) is a cross-track scanning passive microwave radiometer used to retrieve atmospheric temperature and moisture profiles under clear and cloudy conditions. The instrument has 22 channels spanning 23.8–183.3GHz and includes most of the channels carried by the Advanced Microwave Sounding Unit (AMSU) and the Microwave Humidity Sounder (MHS or similar instrument such as AMSU-B) instruments flown aboard earlier NOAA polar-orbiting satellites. Details of the ATMS instrument, channel characteristics, calibration and validation of the ATMS SDR products are discussed in details by [15] [82].

Fig. 10 summarizes ATMS SDR on-orbit NEDT performance and on-orbit biases computed using the European Center for Medium Range Weather Forecasting (ECMWF) forecast/analysis fields. Table 9 shows S-NPP CrIS Nominal Spectral Resolution (NSR) and Full Spectral Resolution (FSR) SDR performance. Until December 4, 2014, the S-NPP CrIS instrument was operated at a NSR of 0.625, 1.25 and 2.5 cm^{-1} for LWIR, MWIR and SWIR bands, respectively. Starting December 4, 2014, the S-NPP CrIS instrument has been operating in FSR mode with a spectral resolution of 0.625 cm^{-1} in all of the 3 bands, as shown in Fig. 11. The NOAA-20 CrIS instrument has been operating in FSR mode since the beginning of the NOAA-20 mission, and the CrIS SDR processing algorithms for both S-NPP and NOAA-20 have adapted the latest calibration algorithms that contains major changes to the CrIS calibration equation, self-anodization corrections, resampling matrices, and calibration filter [17].

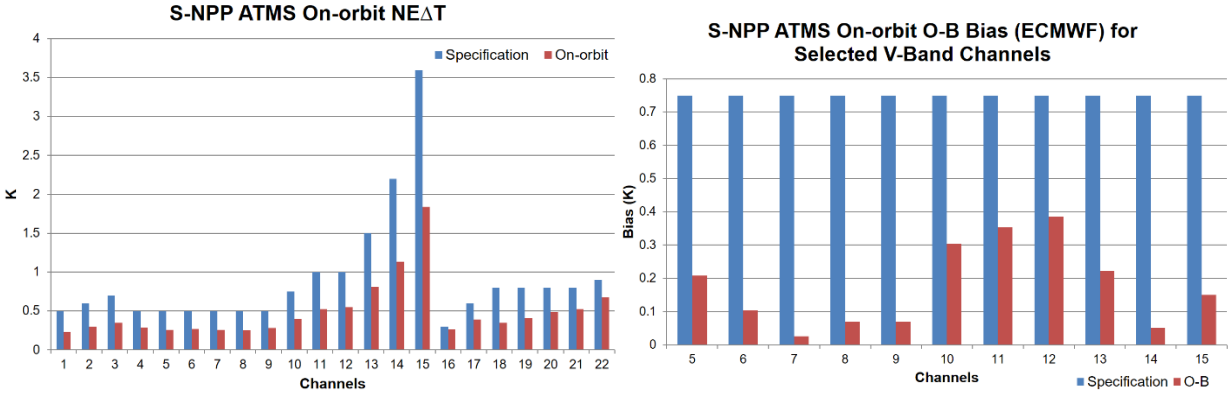

Fig. 10. S-NPP ATMS SDR Performance. The red and blue bars represent the NEDT on-orbit performance versus the specification for the S-NPP ATMS instrument (left Fig.). The S-NPP ATMS SDRs show smaller bias between the observed and calculated radiances using the CRTM (O-B) (red) compared to the specifications (blue) (right Fig.). These Fig.s indicate excellent on-orbit performance of the ATMS instrument. Fig.s are obtained from 2016 JSTAR Annual Meeting team's overview presentation available at JSTAR website [4] (Fig. Courtesy: Quanhua Liu, STAR ATMS SDR team).

Table 9. S-NPP CrIS SDR Performance*

Product	Band	Spectral Range (cm^{-1})	Number of Channels	Spectral Resolution (cm^{-1})	NEdN @287K BB $mW/m^2/sr/cm^{-1}$	Radiometric Uncertainty @287K BB (%)	Frequency Uncertainty (ppm)	Geolocation Uncertainty (km)
NSR	LW	650-1095	713	0.625	**0.098** (0.14)	**0.12** (0.45)	**3** (10)	**1.2** (1.5)
	MW	1210-1750	433	1.25	**0.036** (0.06)	**0.15** (0.58)	**3** (10)	**1.2** (1.5)
	SW	2155-2550	159	2.5	**0.003** (0.007)	**0.20** (0.77)	**3** (10)	**1.2** (1.5)
FSR	LW	650-1095	713	0.625	**0.101** (0.14)	**0.17** (0.45)	**2** (10)	**0.25** (1.5)
	MW	1210-1750	865	0.625	**0.0522** (0.084)	**0.21** (0.58)	**2** (10)	**0.25** (1.5)
	SW	2155-2550	633	0.625	**0.00741** (0.014)	**0.28** (0.77)	**2** (10)	**0.25** (1.5)

* S-NPP CrIS SDR performance and specification (in parenthesis) summary

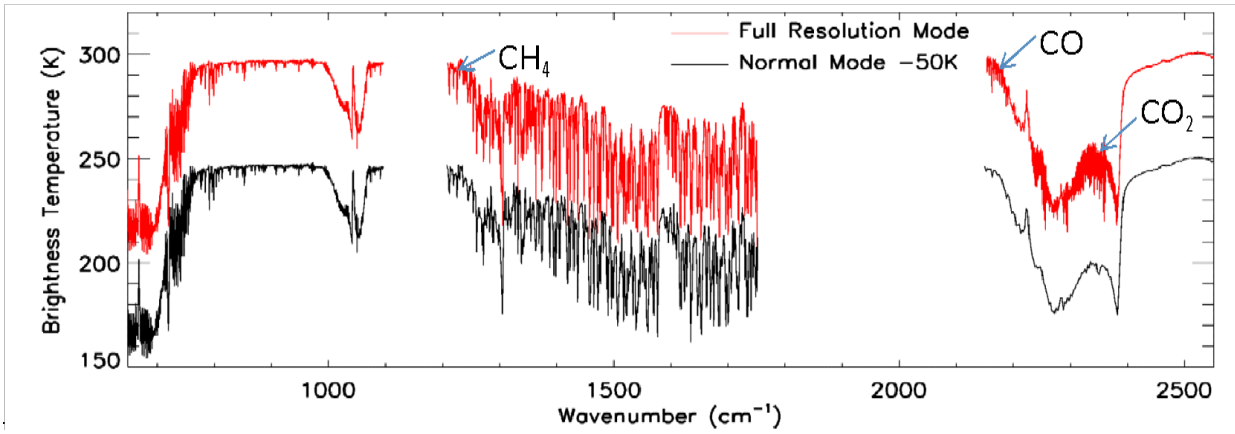

Fig. 11. CrIS NSR/FSR The full spectral resolution coupled with incredibly low noise in all three bands enables high quality CO and other trace gas retrievals (Fig. Courtesy: Flavio Iturbide-Sanchez, STAR CrIS SDR team).

The availability of MW sounding instruments and the utility of the MW retrievals as the initial guess for the hyper-spectral IR sounding retrievals have alleviated cloud-clearing and allowed generation of high-quality geophysical products in scenes with up to 80% cloud cover [80, 83]. Initial development of the microwave-only and microwave/infrared sounding products for the JPSS mission were based on pre-existing microwave/infrared sensor pairs, such as the AMSU-A and MHS paired with the IASI instrument, and the AMSU-A instrument paired with the Aqua-AIRS instrument. Details of these instruments and their channel characteristics are described in many publications [69-71].

These developments led NOAA to define, develop, and operationalize two EDR operational product development systems. The NOAA Unique Combined Atmospheric Processing System (NUCAPS, [84]) uses hyper-spectral CrIS IR observations (aided by ATMS), while the Microwave Integrated Retrieval System (MiRS, [85]) relies solely on ATMS observations.

3.2.1 The NUCAPS CrIS/ATMS EDR Products

The NUCAPS algorithm is built upon heritage from the Atmospheric Infrared Sounder (AIRS) science team retrieval algorithm [83]. In addition to temperature, water vapor, and ozone products, the NUCAPS system operationally produces several trace gas products (e.g. CO, CH_4, CO_2, Volcanic SO_2) from the CrIS/ATMS instruments. CrIS radiances are also used to produce near-real-time Outgoing Longwave Radiation (OLR) product. CrIS-derived OLR values are estimated as a weighted linear combination of CrIS-adjusted ''pseudo channel'' radiances. The estimation of OLR on a near-real-time basis provides a unique perspective for studying the variability of Earth's current atmospheric radiation budget [86] .

The CrIS instrument NSR/FSR observations have been applied to NUCAPS retrieval algorithm to provide temperature, moisture, ozone profiles, and atmospheric trace gas profiles [84]. The full spectral resolution coupled with low noise in all three bands enable high quality CO and other trace gas retrievals [87]. The FSR observations allow discriminating very strong water lines in the MWIR and this leads to better derivation of upper tropospheric humidity. The increased spectral resolution also improves the calibration of the SWIR and improve temperature sounding, which, in turn, leads to improved sounding products [88].

The NUCAPS algorithm has been adapted as an enterprise solution to work on S-NPP and NOAA-20 CrIS/ATMS, AIRS/AMSU-A, and Meteorological Operational Satellite Program (MetOp) Infrared Atmospheric sounder (IASI)/AMSU-A/AMSU-B instrument complements. The algorithm has been evolved and evaluated over the years using the data from the hyper-spectral IR instruments and using associated MW instruments. The temperature, water vapor, and ozone retrievals have been validated for AIRS [89, 90], IASI [91], and CrIS [92-95]. The CO derived from full resolution SNPP and NOAA-20 CrIS SDR has reached provisional maturity, while CO_2 and CH_4 remain at beta maturity [4]. Tables 10 and 11 show the S-NPP NUCAPS products performance for Temperature/Moisture Profiles and for Trace Gases and OLR Products, respectively.

Table 10. S-NPP NUCAPS Temperature/Moisture Profile Performance and Requirements*

Clear (Cloud < 50%)				**Cloudy (Cloud ≥ 50%)**			
Temperature Profile		**Moisture Profile**		**Temperature Profile**		**Moisture Profile**	
Layer	**P (R) K**	**Layer**	**P (R) %**	**Layer**	**P (R) K**	**Layer**	**P (R) %**
1-30	1.5 (1.5)	100-300	22.7 (35)	30-300	2.1 (1.5)	100-400	39.8 (40)
30-300	1.1 (1.5)	300-600	24.9 (35)	300-700	2.3 (1.5)	400-600	35.6 (40)
300-Surf	1.3 (1.6)	600-Surf	22.7 (20)	700-Surf	3.0 (2.5)	600-Surf	29.2 (20)

* S-NPP NUCAPS Temperature and Moisture Profile Performance and Requirements (in parenthesis) summary

Table 11. S-NPP NUCAPS Trace Gases and OLR Products Performance

Product	**Requirement**		**Performance**	
	Accuracy	**Precision**	**Accuracy**	**Precision**
IR Ozone Profile (O_3) *				
- 4-260 hPa	10%	20%	-1.8%	14.3%
- 260 hPa – Surface	10%	20%	-9.4%	21.2%
Carbon Monoxide (CO)	±25%	35%	5.2%	5.5%
Carbon Dioxide (CO_2)	±1% (4 ppmv)	0.5% (2 ppmv)		
Methane (CH_4)	±4% (80 ppbv)	1% (20 ppbv)		
Outgoing Longwave Radiation	5 W/m^2	12 W/m^2	1.5 W/m^2	5 W/m^2

* Ozone: Uncertainty: 25% (Requirement), Performance: 18.9% (4-260hPa); 23.2% (260hPa – Surface)

Fig. 12 comprises a suite of images from JPSS products; VIIRS Active Fire (a), VIIRS AOD (b), as well as the CO derived from CrIS/NUCAPS at 500mb (c) and 700mb (d), over the severe fires in California for 09 November 2018. The retrieved CO product from NUCAPS, while showing the consistent distribution with the fire and smoke observed from VIIRS, also provides information about the vertical distribution and transport of the CO over the downwind regions. NUCAPS Sounding EDRs derived from various satellite missions (S-NPP and NOAA-20 CrIS/ATMS; Aqua-AIRS/AMSU-A; MetOp-A, B, IASI/AMSU-A/AMSU-B) allow for inter-comparison of the products and enterprise validations using common ground truth measurements [89, 90, 96], development of blended products for consistent mission-agnostic data products, and in establishing future objective requirements.

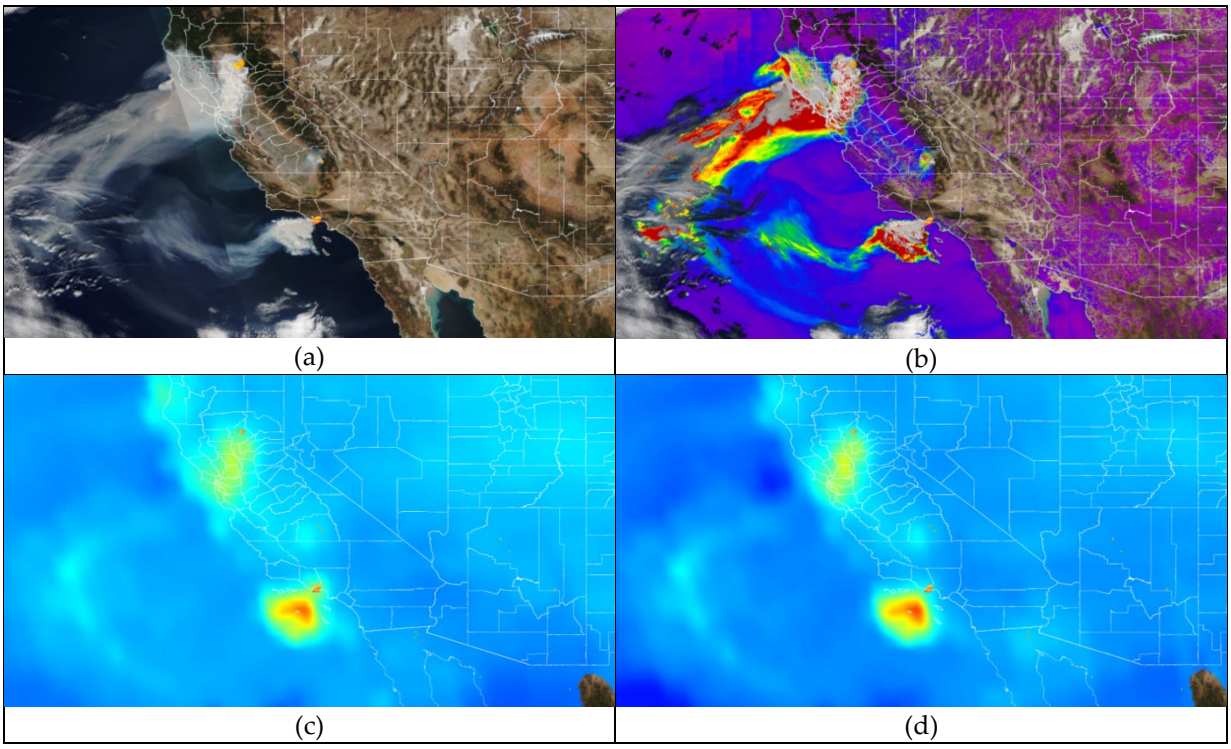

Fig. 12. JPSS Products captured severe California fire in November 2018: (a). VIIRS Active Fire; (b). VIIRS AOD; (c) CrIS/NUCAPS CO at 500mb; (d). CrIS/NUCAPS CO at 700mb (Fig.s from JSTAR Mapper website https://www.star.nesdis.noaa.gov/jpss/mapper)

3.2.2 The MiRS 'Microwave-only' ATMS EDR Products

The MIRS processing systems is a 'microwave-only' retrieval system is based on 1D-variational and physical retrieval algorithm using the Community Radiative Transfer Model (CRTM) as the forward and adjoint operators [85]. The MiRS retrieval algorithm is designed as an enterprise processing system and is applied operationally on a number of microwave sensors from many satellite platforms, including the ATMS aboard the S-NPP/NOAA-20 satellites. The MiRS product suite includes a wide variety of surface and atmosphere products, such as temperature, water vapor, clouds, rain rate, and the cryosphere products [97]. Recently, the MiRS team added snow fall rate (SFR, [98]) to the operational list of products, and most of the MiRS products from the S-NPP ATMS have reached the validated maturity stage, and the NOAA-20 MiRS products have passed through Beta and Provisional maturity reviews. Fig. 13 shows an example of the S-NPP ATMS derived MiRS total precipitable water (left panel) compared with the ECMWF analysis fields (middle panel) with the correlation higher than 0.98 as shown in the corresponding scatter plot. Tables 12 and 13 provide the APUs validation results for the MiRS product suite.

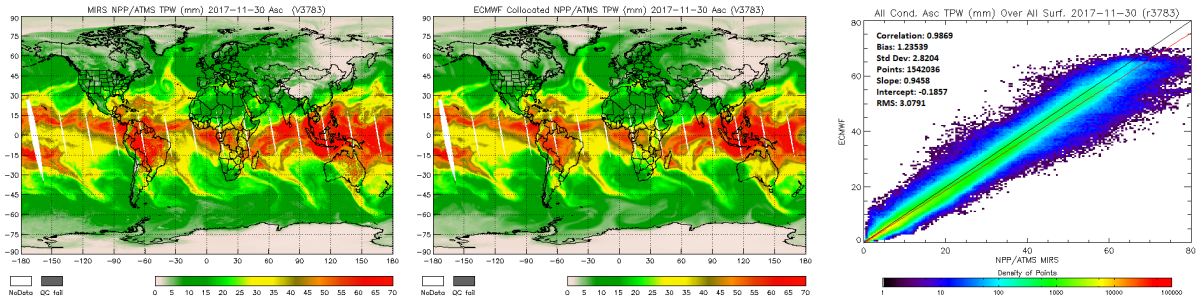

Fig. 13. MiRS Total Precipitable Water (left panel) compared to ECMWF analysis fields (middle panel). The scatter plot (right panel) shows very good agreement with a correlation higher than 0.98 between MiRS retrieved and ECMWF TPW (Fig. Courtesy: Quanhua Liu, STAR MiRS team).

Table 12. S-NPP MiRS Temperature/Moisture Profile Performance*

Product	Sea Clear		Sea Cloudy		Land Clear/Cloudy	
Temperature Profile	**Accuracy (K)**	**Precision (K)**	**Accuracy (K)**	**Precision (K)**	**Accuracy (K)**	**Precision (K)**
100 hPa	-0.2 (0.2)	1.7 (2.0)	0.0 (0.8)	1.9 (2.0)	-0.5 (0.5)	1.5 (2.0)
300 hPa	0.6 (0.5)	1.5 (2.0)	0.4 (0.8)	1.9 (2.5)	0.8 (0.8)	1.7 (2.0)
500 hPa	-0.5 (0.2)	1.1 (2.0)	-0.5 (0.6)	1.4 (2.0)	0.0 (0.2)	1.5 (2.5)
900 hPa	0.2 (1.5)	1.9 (3.0)	0.6 (2.0)	2.1 (3.0)	-0.8 (2.5)	2.6 (5.5)
Water Vapor Profile	**Accuracy (%)**	**Precision (%)**	**Accuracy (%)**	**Precision (%)**	**Accuracy (%)**	**Precision (%)**
400 hPa	0 (30)	45 (60)	0 (30)	55 (60)	7 (30)	45 (60)
500 hPa	2 (20)	40 (60)	2 (20)	42 (65)	2 (10)	35 (60)
700 hPa	4 (20)	30 (50)	2 (10)	32 (60)	5 (10)	30 (50)
900 hPa	0 (20)	15 (30)	0 (20)	18 (30)	5 (20)	25 (50)

* MiRS Temperature and Water Vapor Profile performance and requirements (shown in parenthesis) summary

Table 13. S-NPP MiRS Products Performance

Product	Requirement		Performance	
Snow Cover				
- Probability of Detection (%)	80		84	
Snowfall Detection				
- Probability of Detection (%)	40		51	
	Accuracy	**Precision**	**Accuracy**	**Precision**
Snowfall Rate (mm/hr)	0.3	1.0	0.06	0.74
Snow Water Equivalent (cm)	3.0	6.0	-1.2-2.0	2.1-4.2
Sea Ice Concentration (%)	10	25	2-10	10-20
Cloud Liquid Water (mm)	0.03	0.08	0.003-0.009	0.07
Land Surface Emissivity (%)				
- 23.8 GHz	2.0	3.0	0.0-0.4	2.0-2.3
- 50.3 GHz	1.5	3.0	0.1-0.6	2.7-3.0
- 165.5 GHz	1.5	4.0	0.1-0.7	3.0-3.8
Land Surface Temperature *	4 K	7 K	-1.84 K	5.26 K
Total Precipitable Water (mm)				
- Sea Clear	1.5	2.5	1.3	1.8
- Sea Cloudy	0.5	2.5	0.2	1.9
- Sea-Ice Clear/Cloudy	2.0	2.0	-0.5	1.6
- Land Clear/Cloudy	2.5	5.5	-0.5	4.8
- Snow Clear/Cloudy	0.5	2.0	-0.2	0.8
Rainfall Rate (mm/hr)				
- Sea	0.10	1.0	0.08	1.0
- Land	0.05	1.5	0.01	0.8

* LST Performance Uncertainty and Requirement (shown in parenthesis): 5.58 (8.0) K

3.3 *The OMPS instrument and Science Data Products*

The S-NPP OMPS has three instruments, the Nadir Mapper (OMPS-NM), Nadir Profiler (OMPS-NP), and Limb Profiler (OMPS-LP) that measures scattered solar UV and visible radiance to derive three

dimensional distributions of ozone and other atmospheric constituents for daily monitoring. The OMPS Version 8 algorithms for Total Ozone (V8TOz from OMPS-NM) and Ozone Profile (V8Pro from OMPS-NP) have the heritage from the Solar Backscatter Ultra Violet (SBUV) algorithms [99]. The OMPS-LP ozone product algorithm is based on a scattering retrieval technique used for the Shuttle Ozone Limb Sounding experiment [100]. The NM instrument provides total column ozone (TC), UV absorbing aerosol index (UVAI), and total column SO_2 at 50 x 50 km^2 horizontal resolution at nadir from S-NPP with 2% accuracy. Starting with NOAA-20, these products will be produced at 17 x 17 km^2 resolution at nadir. The NP instrument produces middle and upper stratosphere ozone profiles in the orbital track at 250 x 250 km^2 (50 x 250 km^2 from NOAA-20) resolution with 5% accuracy and 5 to 10 km vertical resolution in the middle and upper stratosphere. The Limb Profiler (LP) currently on S-NPP (and in the future on JPSS-2) provides high vertical resolution stratospheric ozone product at 5% accuracy and 3 km vertical resolution in the stratosphere. The OMPS-NM total column ozone products have been compared with similar products from ground-based and satellite based instruments [101] as shown by the comparisons between S-NPP OMPS-NM (NOAA Version 8 algorithm), MetOp-A/B Global Ozone Monitoring Experiment–2 (GOME-2, NOAA Version 8 algorithm), and NASA EOS Aura Ozone Monitoring Instrument (OMI, NASA Version 8.6 algorithm) in Fig. 14. The JSTAR ozone teams currently produce daily, global and regional scale TC, UVAI and SO_2 products and support UV index forecasts and hazard warning systems in place of OMI (SO_2) [102]. The NCEP uses OMPS EDR products towards (1) continuation of the long-term climate data record and climate monitoring that began with the SBUV/2, (2) near real-time monitoring of the ozone hole, and (3) UV index forecasts and for stratospheric intrusion/monitoring forecasts. Fig. 15 shows an example of the UV index forecast product produced from the S-NPP OMPS observations [103]. Some research products include total column and tropospheric NO_2 (from NM), the Mg II index product that is of interest to solar activity (from NP), and stratospheric aerosol profiles derived from the LP, which help map-out stratospheric aerosol loading due to natural eruptions. Table 14 shows the S-NPP OMPS SDR performance.

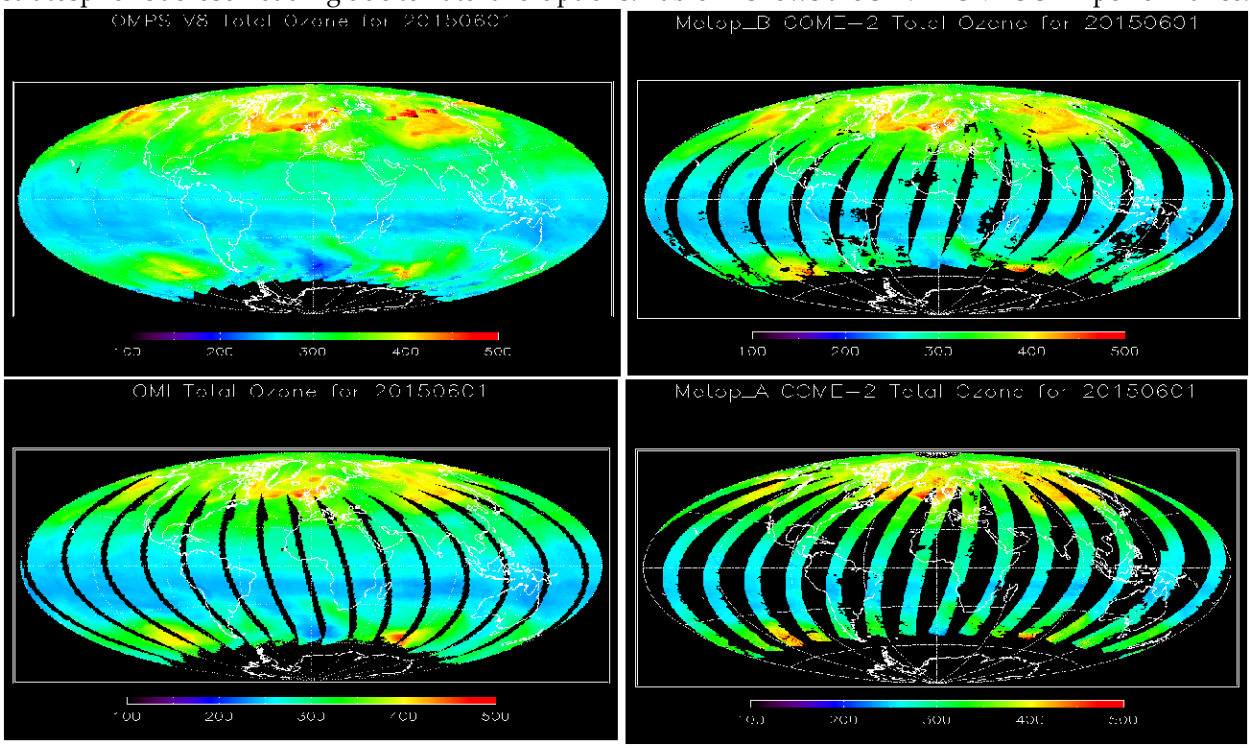

Fig. 14. OMPS Total Column Ozone Products from MetOp-B GOME-2 (NOAA Version 8 algorithm), NASA EOS Aura OMI (NASA Version 8.6 algorithm) and S-NPP OMPS-NM (NOAA Version 8 algorithm) for 20150601 (Fig. Courtesy: Lawrence E Flynn, STAR OMPS Ozone team).

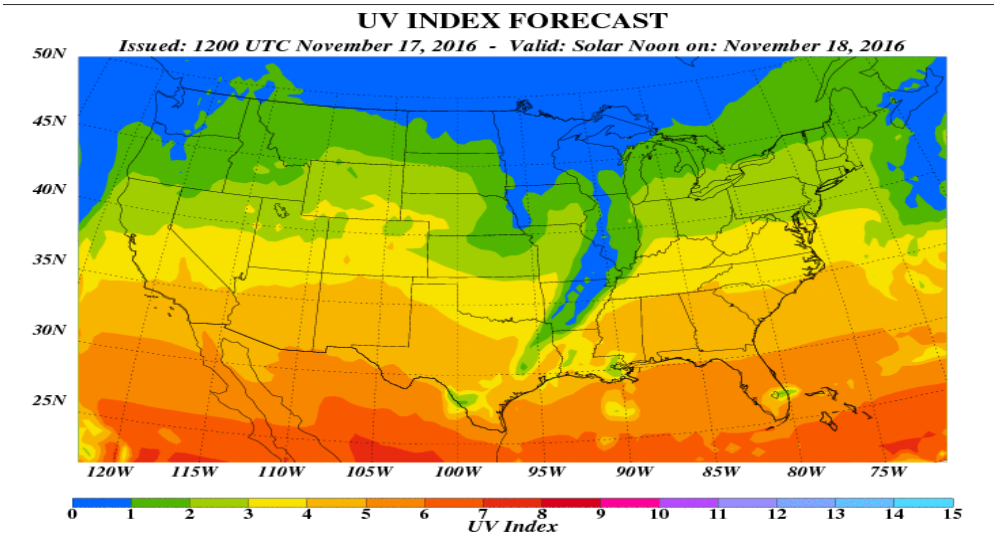

Fig. 15. UV Index Forecast product (November 18, 2016) utilizing S-NPP OMPS observations (Fig. Courtesy: Craig Long, NWS)

Table 14. S-NPP OMPS SDR Performance

Attribute	OMPS-NM		OMPS-NP	
	L1RDS Thresholds	Performance	L1RDS Thresholds	Performance
Non-linearity accuracy	< 0.2%	< 0.2%	< 0.2%	< 0.2%
SNR	1000	> 1000	45-400 channel dependent	> 1000
Straylight Out-of-band & Out-of-Field response	< 2%	< 2%	< 2%	< 2%
Orbital thermal wavelength shift	0.02nm	~0.006nm	0.02nm	~0.006nm
Absolute irradiance calibration accuracy	< 7%	< 7% for most channels	< 7%	< 7% for most channels
Absolute radiance calibration accuracy	< 8%	< 8%	< 8%	< 8%
Albedo calibration accuracy	< 2%	< 2% For most channels	< 2%	< 2% For most channels

3.4 *The GCOM-AMSR2 Instrument and Science Data Products*

The GCOM AMSR2 instrument is a dual-polarized, conical scanning, passive microwave radiometer and provides a variety of products exploiting the availability of dual-polarized measurements with central frequencies at 6.925, 10.65, 18.7, 23.8, 36.5, and 89.0 GHz. AMSR2 provides data continuity with several enhancements for the AMSR for Earth Observing System (AMSR-E) on NASA's Aqua satellite [104]. Under the collaborative agreements between the JPSS and the JAXA Program, the IDPS processing system generates RDRs from G-COM data received in real-time through Svalbard. The NDE operational system

generates G-COM AMSR2 Level-1 data sets (equivalent to SDRs) using the software provided by JAXA and derives a variety of Level-1 and Level-2 products that include: calibrated microwave brightness temperatures, total precipitable water, cloud liquid water, precipitation type/rate, sea surface temperature, and sea surface wind speed [105]. Some of these products serve as standalone AMSR2 baseline products, while others are blended products with a multitude of sensors (e.g. ATMS) [106]. The baseline suite of products from AMSR2 includes cloud properties, rain rate, soil moisture, and snow and ice products (Table 15). Examples of blended products include total precipitable water and rain rate. The processing systems of MIRS, Interactive Multisensor Snow and Ice Mapping System (IMS), and Soil Moisture Operational Product System (SMOPS) produce these hydrological products and use enterprise solutions to derive products from JPSS ATMS, GCOM-AMSR2, and other instrument complements. Some JPSS hydrological products have been utilized in Earth system modeling and data assimilation, such as snow cover and soil moisture [107].

Table 15. GCOM-AMSR2 Products Performance

Product	Requirement	Performance
Cloud Liquid Water		
- **Uncertainty (over ocean)**	0.05 mm	0.03-0.09 mm
- **Accuracy**	0.01 mm	0.01 mm
Total Precipitable Water		
- **Uncertainty**	2 mm or 10%	1.1-1.8 mm
- **Accuracy**	1 mm	0.1-0.7 mm
Precipitation (Type/Rate)		
- **Precision**	0.05 mm/hr	0.01 mm/hr
- **Uncertainty, over ocean**	2 mm/hr	1.2-1.4 mm/hr
- **Uncertainty, over land**	5 mm/hr	3.1-3.6 mm/hr
Sea Surface Temperature		
- **Uncertainty**	1.0 K	0.5-0.7 K
- **Accuracy**	0.5 K	0.2 K
Sea Surface Wind Speed		
- **Uncertainty**	2.0 m/s or 10%	0.9-1.5 m/s
- **Accuracy**	0.5 m/s	0.1-0.3 m/s
Sea Ice		
- **Ice concentration, uncertainty**	10%	3.9% NH; 4.4% SH
- **Ice type, % correct typing**	70%	80-90%, Arctic winter
Snow		
- **Snow Depth, uncertainty**	20 cm	15-22 cm
- **Snow Cover, % correct typing**	80%	72-97 %
Snow Water Equivalent		
- **Uncertainty**	50-70 %	20-22 %
Soil Moisture		
- **Uncertainty**	6%	5%

4. NOAA-20 Algorithm Upgrades and Science Data Products

Launched on November 18, 2017 with a 50-minute separation from the S-NPP orbit, NOAA-20 carries aboard the same instrument complements currently operating on S-NPP. This provide both continuity of the existing high quality data products currently produced through S-NPP and additional products as a direct result of the instrument upgrades and science improvements. Feedback from S-NPP product development, Cal/Val, maturity reviews, and user communities has allowed the JSTAR teams to realize a

large number of science improvements and upgrades for both existing S-NPP algorithms and many new products. Some of these science improvements and upgrades have already been implemented as part of S-NPP products upgrades. In addition to the science improvements, the JSTAR teams developed necessary algorithm upgrades and mitigations prior to the NOAA-20 launch based on pre-launch characterizations of the instruments. During the pre-launch phase, the JSTAR teams facilitated performance analysis of pre-launch test data, such as instrument configuration parameters (or calibration LUTs), improvements and refinements to mitigate instrument waivers. The JSTAR teams also verified NOAA-20 science algorithm developments related to instrument upgrades using proxy data sets derived from S-NPP and NOAA-20 pre-launch test data sets. All NOAA-20 SDR pre-launch product algorithms were implemented in the IDPS, and most of the EDR algorithms have been migrated to enterprise algorithms for operationalization in NDE.

Following the launch of the NOAA-20 satellite, various testing activities have allowed the JSTAR teams to successfully monitor, evaluate, and quantify changes from the pre-launch versions of the NOAA-20 science datasets (e.g. radiometric, spectral, and geometric changes). The JSTAR teams accomplished most of the first 90 day planned science activities to achieve Beta and Provisional Maturity for NOAA-20 KPP products using on-orbit performance and calibration data and after accommodating post-launch fixes and updates to calibration LUTs. All NOAA-20 KPPs (SDRs and imagery products) have been declared Beta maturity as of January 25, 2018, Provisional maturity as of February 16, 2018, and Validated maturity as of October 2018. NOAA NESDIS promoted all of these SDR products into operations after attaining provisional maturity status. The science teams adapted S-NPP EDR validated maturity algorithms for NOAA-20 and updated the algorithms with the other NOAA-20 specific sensor characteristics to define the NOAA-20 EDR product algorithms. The JSTAR teams initiated the execution of Cal/Val plans and schedules for all of the EDR products.

Fig. 16 shows the expedited schedule of the Cal/Val and product validated maturity for NOAA-20 SDR/EDR products. Following the lessons learned through S-NPP product maturity, adapting Cal/Val tools developed during S-NPP Cal/Val process to NOAA-20, and methodologies optimized in collecting the in-situ measurements, the teams are expediting the NOAA-20 validated maturity.

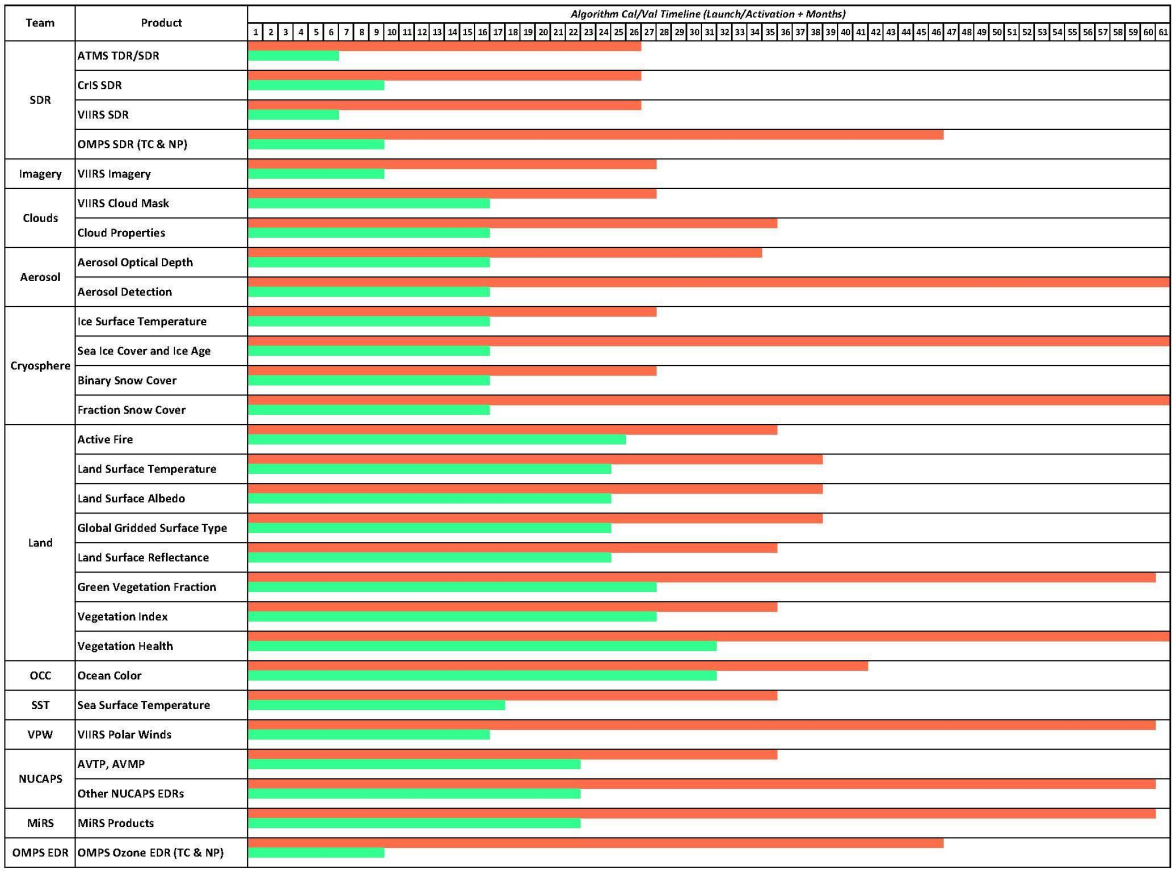

Fig. 16. NOAA-20 Validated Maturity projections. The red (for S-NPP) and green (for NOAA-20) bars depict validated maturity timelines (Launch/Activation + Months). The lessons learnt through S-NPP product maturity, adapting some of the Cal/Val tools developed through S-NPP, methodologies optimized in collecting the in-situ measurements are helping to expedite the NOAA-20 validated maturity.

5. Quality Assurance and Product Quality Monitoring

To ensure efficient research-to-operations transitions for science product algorithm updates, the JSTAR Program has implemented Quality Assurance (QA) procedures. The QA procedures [2] implemented and time-tested through S-NPP product development, operations, and reactive maintenance phases have been augmented for NOAA-20 to achieve efficient end-to-end product life-cycle operations. As part of the quality assurance and users engagement, JSTAR teams continue to update the website [4] with detailed information on the JPSS instruments, science data products and documents, product maturity status, long term validation, and science monitoring of S-NPP/NOAA-20 SDR/EDR products.

For JPSS product quality monitoring, the JSTAR teams have implemented two performance-monitoring systems for the S-NPP/NOAA-20, namely, the ICVS [108] and the EDR LTM [109] monitoring systems. The ICVS is a web-based system for continuously monitoring the sensors' performance and the associated data product quality. The JSTAR science teams as well as Common Ground System and flight teams have used ICVS for many corrective actions and long-term sustainment of S-NPP/NOAA-20 products. Similar to the ICVS, the EDR LTM integrates science product monitoring and routine validations to aid the operational users and product scientists in monitoring the EDR product quality in near real time routinely as well as on a long-term basis. The LTM system currently allows users to visualize satellite EDR products from the Suomi NPP and other domestic and international polar-orbiting satellite constellations

through a searchable interface to easily access data, products and plots by date, type, and other sorting parameters. Ongoing improvements to the LTM include maps of quality flags, inter-comparisons of products from similar satellite instrument complements from an array of polar orbiting satellites, and overlays of products useful for many user-applications. The JSTAR-Mapper [110] is the latest addition to the LTM, which provides synergistic use of data products in identifying and analyzing near-real time event-based applications.

6. Reprocessing and Enterprise EDR Algorithms

One of the major objectives of the JSTAR teams is to provide consistent long-term high quality data products derived from four instruments on S-NPP. In the process of achieving Beta, Provisional, and Validated maturity stages, the science teams have implemented periodic updates of algorithms (e.g. fixing shortfalls through processing coefficient table (PCT) updates, improvements to quality flags, and performing mitigations to instrument sensor/channel mal-functions) for real-time product generation. Consequently, although the product accuracy and precision is improved in meeting the requirements for various maturity stages, the operational stream of data products may have varying characteristics, and the science teams recognized the need for science quality reprocessing to remove artifacts and to reduce biases. Based on the recommendations received from NOAA stakeholders and user communities through reprocessing, enterprise algorithm workshops, and STAR Annual Science Team Meetings [4], the JSTAR science teams have updated the SDR algorithms and calibration input parameters with the validated maturity algorithm codes and reprocessed the SDR products for the S-NPP mission. The reprocessed SDR products are currently hosted at the Cooperative Institute for Climate & Satellites (CICS) servers [111] and are going through final quality checks and verification. Meanwhile, the JSTAR science teams have implemented most of the EDR enterprise algorithms at NDE. Since the EDR products get impacted both by upstream SDR product changes as well as EDR algorithm changes (through various maturity stages), the teams are currently working on S-NPP EDR reprocessing using the reprocessed SDRs and NDE operational versions of the enterprise EDR algorithms to generate mission-long consistent EDR products. This will ensure long-term consistency of data product quality and enable users to utilize the high-quality products retroactively to evaluate impacts on user applications and prepare the necessary infrastructure to use the near-real time products.

7. NWP and NRT Applications, User Connectivity Initiatives

7.1 *JPSS data in NWP Assimilations*

The S-NPP ATMS radiances and CrIS FSR data sets are routinely accessed and assimilated by the NWP centers worldwide, and forecast experiments conducted with the assimilation of these radiances have shown positive impact [5] . Following the operational systems development starting with AIRS near-real-time processing using NUCAPS [112], NWP centers worldwide have accessed several hyperspectral radiance products, such as the thinned radiance data sets, principal component scores, and cloud-cleared radiances, etc. The NUCAPS enterprise processing system that runs on Aqua-AIRS, MetOp-A/B-IASI, and S-NPP/NOAA-20 CrIS instruments provide the retrieval products to the forecast users. The NOAA NWS, the ECMWF, and many other operational agencies worldwide assimilate these radiances into their NWP models. Forecast Sensitivity Observation Impact (FSOI) experiments conducted by Jung et. al., [44] with the CrIS data assimilation into Global Forecasting System (GFS) show that utilizing 104 FSR channels from the new channel selection and adjusting assimilation weights has improved CrIS ranking from 9th to 5th of the total moist energy norm computed from the Global Data Assimilation System (GDAS) ensembles.

7.2 *PGRR and NRT Applications and User Connectivity Initiatives*

The PGRR science program initiated at the beginning of the JPSS program has been providing vital program functions on (a) addressing data needs across NOAA line offices (e.g. NWS, NMFS, OAR, etc.) and other agencies, (b) identification of requirements and prioritization via the LORWG, (c) fostering algorithm development for high-quality data products, Cal/Val, publications, reprocessing and enterprise solutions, and (d) overseeing deliveries of software packages to operations and CSPP DB services. A wide

number of PGI and near real-time applications are ongoing in Atmospheric Chemistry, River Ice and Flooding, Fire and Smoke, Soundings, Data Assimilation, Imagery/Now casting, Ocean/Coastal applications, Hydrology, Arctic, and Land data assimilations, and details on these activities are published through JPSS Science Seminar Annual Digest publications [113].

8. Summary and Conclusions

The S-NPP satellite has been extremely successful in operations for the last seven years and has produced an array of very high quality atmospheric, land, ocean, and cryosphere data products. The recently launched NOAA-20 is producing high quality data products currently provided through S-NPP, along with additional products as a direct result of the instrument upgrades and science improvements. All of the S-NPP data products have passed through the Cal/Val validated maturity stage, and the products are now at the long-term monitoring and reactive maintenance phase. The NOAA-20 KPP products have all reached validated maturity status as of October 2018. The NOAA-20 EDR products are currently at the Beta/Provisional maturity stages, and most EDRs reached provisional maturity stage by the end of 2018. The S-NPP/NOAA-20 satellite data products are disseminated through the NOAA's PDA and CLASS systems for NOAA stakeholders and user agencies worldwide. Progress on using S-NPP products in NWP assimilations worldwide, in support of observing and predicting key weather phenomena (e.g. hurricanes, blizzards), and for event based applications (e.g. flash floods, volcanic ash, wildfires etc.), have shown remarkable success. The ability to derive JPSS products regionally at a much higher latency through DB networks using CSPP has been extremely fruitful for many real-time applications. The JPSS-2 and follow-on satellites (JPSS-3, 4) with similar instruments and consistent science products produced from the JPSS constellation provide users with the opportunity to transition from the aging legacy NOAA POES and EOS Aqua and Terra satellites products and keep-up with continuity and connectivity for coordinated science experiments. Commitments and collaborative agreements between the JPSS Program, EUMETSAT, and JAXA are leading to a wide variety of enterprise algorithm solutions for consistent data product generation, demonstration of blended product generation and application, and operationalization towards mission-agnostic data products leading to measurement-based approach. The JSTAR Program will continue the development/improvement of algorithms for both S-NPP and NOAA-20, as well as future JPSS missions. The team is also actively engaged in implementing the enterprise algorithms and in reprocessing the S-NPP SDR/EDR data products with the most mature, validated algorithms towards the generation and archival of science quality data products to advance satellite research and applications. Finally, through the ICVS, EDR-LTM, and JPSS Mapper websites, JSTAR provides much needed real-time product display and evaluations, along with numerous documents and webpage links on S-NPP/NOAA-20 products, ATBDs, maturity reviews, meeting minutes of JSTAR Annual Science Team Meetings and coordinated efforts with NOAA stakeholders and user communities.

Acknowledgements

The work of JSTAR program is funded by NOAA JPSS Office (NJO). This paper describes the collective work of government industry and academic teams over the course of many years. The authors would like to acknowledge the hard work and dedication of all contributing individual companies and organizations. The manuscript contents are solely the opinions of the authors and do not constitute a statement of policy, decision, or position on behalf of NOAA or the U.S. government.

References

1. Goldberg, Mitchell D., Heather Kilcoyne, Harry Cikanek, and Ajay Mehta. "Joint Polar Satellite System: The United States Next Generation Civilian Polar-Orbiting Environmental Satellite System." *Journal of Geophysical Research: Atmospheres* 118, no. 24 (2013): 13,463-13,75.
2. Zhou, Lihang, Murty Divakarla, and Xingpin Liu. *An Overview of the Joint Polar Satellite System (Jpss) Science Data Product Calibration and Validation*. Vol. 8, 2016.

3. NOAA. "Comprehensive Large Array-Data Stewardship System (Class) Website." http://www.nsof.class.noaa.gov (accessed January 23).
4. NOAA, JSTAR. "Jpss Center for Satellite Research and Applications (Star) Website." https://www.star.nesdis.noaa.gov/jpss/index.php (accessed January 23).
5. Goldberg, M.D. "The Value of Polar Satellite Direct Broadcast Data for Nowcasting and Short Range Weather Forecasting." In *EUMETSAT*. Rome, Italy, 2017.
6. Joo, Sangwon, John Eyre, and Richard Marriott. "The Impact of Metop and Other Satellite Data within the Met Office Global Nwp System Using an Adjoint-Based Sensitivity Method." *Monthly Weather Review* 141, no. 10 (2013): 3331-42.
7. CIMSS. "Cooperative Institute of Meteorological Satellite Studies (Cimss) Community Satellite Processing Package." http://cimss.ssec.wisc.edu/cspp/ (accessed January 23).
8. Gumley, L., M. Goldberg, B. Flynn, D. Santek, J. Braun, and J. Davies. "Rapid Acquisition, Processing and Delivery of Advanced Infrared and Microwave Sounder Data from Polar Orbiting Satellites for Numerical Weather Prediction and Other Time-Sensitive Applications." In *EUMETSAT*. Rome, Italy, 2017.
9. Hillger, Don, Tom Kopp, Curtis Seaman, Steven Miller, Dan Lindsey, Eric Stevens, Jeremy Solbrig, William Straka Iii, Melissa Kreller, Arunas Kuciauskas, and Amanda Terborg. *User Validation of Viirs Satellite Imagery*. Vol. 8, 2015.
10. Mitch Goldberg., HA Cikanek, L. Zhou, J. Price. *The Joint Polar Satellite System in Comprehensive Remote Sensing: Missions and Sensors*. Edited by Shunlin Liang. Vol. 1: Elsevier 2017.
11. Walter Wolf, J. Daniels, S. Sampson, L. Zhou, T. King and B. Das. "Migration to Operational Enterprise Algorithms." In *AMS Annual Meeting: 12th Annual Symposium on New Generation Operational Environmental Satellite Systems* New Orleans, LA, 2016.
12. Powell Jr., Alfred M., and Fuzhong Weng. "Introduction to Special Section on Suomi National Polar-Orbiting Partnership Satellite Calibration, Validation, and Applications." *Journal of Geophysical Research: Atmospheres* 118, no. 21 (2013): 12,216-12,17.
13. Pan, C., M. Kowalewski, R. Buss, L. Flynn, X. Wu, M. Caponi, and F. Weng. "Performance and Calibration of the Nadir Suomi-Npp Ozone Mapping Profiler Suite from Early-Orbit Images." *IEEE Journal of Selected Topics in Applied Earth Observations and Remote Sensing* 6, no. 3 (2013): 1539-51.
14. Cao, Changyong, Jack Xiong, Slawomir Blonski, Quanhua Liu, Sirish Uprety, Xi Shao, Yan Bai, and Fuzhong Weng. "Suomi Npp Viirs Sensor Data Record Verification, Validation, and Long-Term Performance Monitoring." *Journal of Geophysical Research: Atmospheres* 118, no. 20 (2013): 11,664-11,78.
15. Weng, Fuzhong, Xiaolei Zou, Ninghai Sun, Hu Yang, Miao Tian, William J. Blackwell, Xiang Wang, Lin Lin, and Kent Anderson. "Calibration of Suomi National Polar-Orbiting Partnership Advanced Technology Microwave Sounder." *Journal of Geophysical Research: Atmospheres* 118, no. 19 (2013): 11,187-11,200.
16. Han, Yong, Henry Revercomb, Mike Cromp, Degui Gu, David Johnson, Daniel Mooney, Deron Scott, Larrabee Strow, Gail Bingham, Lori Borg, Yong Chen, Daniel DeSlover, Mark Esplin, Denise Hagan, Xin Jin, Robert Knuteson, Howard Motteler, Joe Predina, Lawrence Suwinski, Joe Taylor, David Tobin, Denis Tremblay, Chunming Wang, Lihong Wang, Likun Wang, and Vladimir Zavyalov. "Suomi Npp Cris Measurements, Sensor Data Record Algorithm, Calibration and Validation Activities, and Record Data Quality." *Journal of Geophysical Research: Atmospheres* 118, no. 22 (2013): 12,734-12,48.
17. Han, Yong, and Yong Chen. "Calibration Algorithm for Cross-Track Infrared Sounder Full Spectral Resolution Measurements." *IEEE Transactions on Geoscience and Remote Sensing* 56, no. 2 (2018): 1008-16.
18. B. Liao, L., Stephanie Weiss, Steve Mills, and Bruce Hauss. *Suomi Npp Viirs Day-Night Band on-Orbit Performance*. Vol. 118, 2013.
19. NESDIS. "Suomi-Npp Viirs and Aqua Modis Intercomparison." https://ncc.nesdis.noaa.gov/VIIRS/VIIRS_MODIS_Intercomparison.php (accessed January 23).
20. Uprety, Sirish, and Changyong Cao. *Suomi Npp Viirs Reflective Solar Band on-Orbit Radiometric Stability and Accuracy Assessment Using Desert and Antarctica Dome C Sites*. Vol. 166, 2015.
21. Uprety, Sirish, Changyong Cao, Xiaoxiong Xiong, Slawomir Blonski, Aisheng Wu, and Xi Shao. "Radiometric Intercomparison between Suomi-Npp Viirs and Aqua Modis Reflective Solar Bands Using Simultaneous Nadir Overpass in the Low Latitudes." *Journal of Atmospheric and Oceanic Technology* 30, no. 12 (2013): 2720-36.

22. Madhavan, Sriharsha, Jake Brinkmann, Brian N. Wenny, Aisheng Wu, and Xiaoxiong Xiong. "Evaluation of Viirs and Modis Thermal Emissive Band Calibration Stability Using Ground Target." *Remote Sensing* 8, no. 2 (2016): 158.
23. Cao, Changyong, and Yan Bai. "Quantitative Analysis of Viirs Dnb Nightlight Point Source for Light Power Estimation and Stability Monitoring." *Remote Sensing* 6, no. 12 (2014): 11915-35.
24. Miller, Steven D., William Straka, Stephen P. Mills, Christopher D. Elvidge, Thomas F. Lee, Jeremy Solbrig, Andi Walther, Andrew K. Heidinger, and Stephanie C. Weiss. "Illuminating the Capabilities of the Suomi National Polar-Orbiting Partnership (Npp) Visible Infrared Imaging Radiometer Suite (Viirs) Day/Night Band." *Remote Sensing* 5, no. 12 (2013): 6717.
25. JPSS:. "Joint Polar Satellite System (Jpss): Program Level 1 Requirements Supplement, Version 2.10, June 2014.".
26. Cao, Changyang. "Validated Maturity Science Review for Noaa-20 Viirs Sdr, Available at Jpss Star Validated Maturity Review Website." https://www.star.nesdis.noaa.gov/jpss/documents/AMM/N20/VIIRS_SDR_Validated.pdf (accessed March 7).
27. JPSS. "Program Lexicon Jpss-470-00041, Accessible through Star Jpss Webpage:." https://www.star.nesdis.noaa.gov/jpss/documents/470-00041_JPSS_Program_Lexicon_RevC_January_21_2016.pdf (accessed March 3).
28. (edited), Changyong Cao. *Calibration Validation of Visible Infrared Imaging Radiometers and Applications, Isbn 978-3-03842-318-8 (Pbk); Isbn 978-3-03842-319-5 (Pdf), Https://Doi.Org/10.3390/Books978-3-03842-319-5, © 2017 Mdpi; under Cc by-Nc-Nd License*.
29. Hillger, Donald, Thomas Kopp, Thomas Lee, Daniel Lindsey, Curtis Seaman, Steven Miller, Jeremy Solbrig, Stanley Kidder, Scott Bachmeier, Tommy Jasmin, and Tom Rink. "First-Light Imagery from Suomi Npp Viirs." *Bulletin of the American Meteorological Society* 94, no. 7 (2013): 1019-29.
30. Hillger, Donald, Curtis Seaman, Calvin Liang, Steven Miller, Daniel Lindsey, and Thomas Kopp. "Suomi Npp Viirs Imagery Evaluation." *Journal of Geophysical Research: Atmospheres* 119, no. 11 (2014): 6440-55.
31. Lai, Chang, Jia Yue, Jiyao Xu, William C. Straka, Steven D. Miller, and Xiao Liu. "Suomi Npp Viirs/Dnb Imagery of Nightglow Gravity Waves from Various Sources over China." *Advances in Space Research* 59, no. 8 (2017): 1951-61.
32. McHardy, T. M., J. Zhang, J. S. Reid, S. D. Miller, E. J. Hyer, and R. E. Kuehn. "An Improved Method for Retrieving Nighttime Aerosol Optical Thickness from the Viirs Day/Night Band." *Atmos. Meas. Tech.* 8, no. 11 (2015): 4773-83.
33. Miller, Steven D. "A Dynamic Scaling Algorithm for the Optimized Digital Display of Viirs Day/Night Band Imagery Au - Seaman, Curtis J." *International Journal of Remote Sensing* 36, no. 7 (2015): 1839-54.
34. Mills, Stephen, and Steven Miller. "Viirs Day/Night Band—Correcting Striping and Nonuniformity over a Very Large Dynamic Range." *Journal of Imaging* 2, no. 1 (2016).
35. Gladkova, Irina, Alexander Ignatov, Fazlul Shahriar, Yury Kihai, Don Hillger, and Boris Petrenko. "Improved Viirs and Modis Sst Imagery." *Remote Sensing* 8, no. 1 (2016).
36. Zhang, J., S. L. Jaker, J. S. Reid, S. D. Miller, J. Solbrig, and T. D. Toth. "Characterization and Application of Artificial Light Sources for Nighttime Aerosol Optical Depth Retrievals Using the Viirs Day/Night Band." *Atmos. Meas. Tech. Discuss.* 2018 (2018): 1-45.
37. Heidinger, Andrew, Michael Foster, Denis Botambekov, Michael Hiley, Andi Walther, and Yue Li. "Using the Nasa Eos a-Train to Probe the Performance of the Noaa Patmos-X Cloud Fraction Cdr." *Remote Sensing* 8, no. 6 (2016).
38. Heidinger, Andrew K., Amato T. Evan, Michael J. Foster, and Andi Walther. "A Naive Bayesian Cloud-Detection Scheme Derived Fromcalipsoand Applied within Patmos-X." *Journal of Applied Meteorology and Climatology* 51, no. 6 (2012): 1129-44.
39. Frey, Richard A., Steven A. Ackerman, Yinghui Liu, Kathleen I. Strabala, Hong Zhang, Jeffrey R. Key, and Xuangi Wang. "Cloud Detection with Modis. Part I: Improvements in the Modis Cloud Mask for Collection 5." *Journal of Atmospheric and Oceanic Technology* 25, no. 7 (2008): 1057-72.
40. Young, S. A., M. A. Vaughan, and D. M. Winker. "Adaptive Algorithms for the Fully-Automated Retrieval of Cloud and Aerosol Extinction Profiles from Calipso Lidar Data." Paper presented at the IGARSS

2003. 2003 IEEE International Geoscience and Remote Sensing Symposium. Proceedings (IEEE Cat. No.03CH37477), 21-25 July 2003 2003.
41. Weinrich, Jeff. "Aviation Initive." In *STAR JPSS 2018 Annual Conference*. NOAA Center for Weather and Climate Prediction Conference Center, College Park, MD, https://www.star.nesdis.noaa.gov/star/documents/meetings/2018JPSSAnnual/Monday/4_4_Session4_Talk4_Weinrich_AviationInitiative.ptt.pdf, 2018.
42. Heidinger, Andrew. "Viirs Cloud Product Status." In *STAR JPSS 2018 Annual Conference*. NOAA Center for Weather and Climate Prediction Conference Center, College Park, MD, https://www.star.nesdis.noaa.gov/star/documents/meetings/2018JPSSAnnual/Monday/4_2_Session4_Talk2_Heidinger_Cloud_Status_20min_2018.pdf, 2018.
43. Key, Jeff. "Snow, Ice, and Polar Winds." In *STAR JPSS 2018 Annual Conference*. NOAA Center for Weather and Climate Prediction Conference Center, College Park, MD, https://www.star.nesdis.noaa.gov/star/documents/meetings/2018JPSSAnnual/Tuesday/Session8_Talk0_Key_cryosphere_overview.pdf, 2018.
44. James A. Jung, Andrew. Collard, Kristen Bathmann, Dave Groff, Andrew Heidinger, Mitchell Goldberg. "Preparing for Cris Full Spectral Resolution Radiances in the Ncep Global Forecast System." In *21st International TOVS Study Conference*. Darmstadt, Germany, 2017.
45. Wang, Run, Bo Wan, Qinghua Guo, Maosheng Hu, and Shunping Zhou. *Mapping Regional Urban Extent Using Npp-Viirs Dnb and Modis Ndvi Data*. Vol. 9, 2017.
46. Csiszar, Ivan, Wilfrid Schroeder, Louis Giglio, Evan Ellicott, Krishna P. Vadrevu, Christopher O. Justice, and Brad Wind. "Active Fires from the Suomi Npp Visible Infrared Imaging Radiometer Suite: Product Status and First Evaluation Results." *Journal of Geophysical Research: Atmospheres* 119, no. 2 (2014): 803-16.
47. Kogan, F., W. Guo, W. Yang, and H. Shannon. *Space-Based Vegetation Health for Wheat Yield Modeling and Prediction in Australia*. Vol. 12, 2018.
48. Vargas, M., T. Miura, N. Shabanov, and A. Kato. "An Initial Assessment of Suomi Npp Viirs Vegetation Index Edr." *Journal of Geophysical Research: Atmospheres* 118, no. 22 (2013): 12,301-12,16.
49. Vargas, M. "Snpp Viirs Green Vegetation Fraction Validated Maturity Review." https://www.star.nesdis.noaa.gov/jpss/documents/AMM/VIIRS_GVF_Val.pdf (accessed February 28).
50. Ignatov, Alexander, Irina Gladkova, Yanni Ding, Fazlul Shahriar, Yury Kihai, and Xinjia Zhou. "Jpss Viirs Level 3 Uncollated Sea Surface Temperature Product at Noaa." 2017.
51. Petrenko, Boris, Alexander Ignatov, Yury Kihai, John Stroup, and Prasanjit Dash. "Evaluation and Selection of Sst Regression Algorithms for Jpss Viirs." *Journal of Geophysical Research: Atmospheres* 119, no. 8 (2014): 4580-99.
52. NOAA. "Coastwatch Oceanwatch: Satellite Data Products for Understanding and Managing Our Oceans and Coasts " https://coastwatch.noaa.gov/cw/index.html (accessed January 23).
53. Wang, Menghua, Xiaoming Liu, Lide Jiang, SeungHyun Son, Junqiang Sun, Wei Shi, Liqin Tan, Puneeta Naik, Karlis Mikelsons, Xiaolong Wang, and Veronica Lance. "Evaluation of Viirs Ocean Color Products." Paper presented at the SPIE Asia-Pacific Remote Sensing 2014.
54. Wang, Menghua, and Lide Jiang. *Viirs-Derived Ocean Color Product Using the Imaging Bands*. Vol. 206, 2018.
55. NOAA. "Star Ocean Color Team." https://www.star.nesdis.noaa.gov/sod/mecb/color/index.php (accessed January 23).
56. Garcia, S., and K. Cochrane. "Ecosystem Approach to Fisheries: A Review of Implementation Guidelines." *ICES Journal of Marine Science* 62, no. 3 (2005): 311-18.
57. NOAA, STAR. "Coral Reef Watch: Satellite Monitoring and Modeled Outlooks " https://coralreefwatch.noaa.gov (accessed January 23).
58. NOAA. "Polarwatch: Providing Access to Ocean Satellite Data in the Arctic and Antarctic." https://polarwatch.noaa.gov/ (accessed January 23).
59. Ciren, Pubu, and Shobha Kondragunta. "Dust Aerosol Index (Dai) Algorithm for Modis." *Journal of Geophysical Research: Atmospheres* 119, no. 8 (2014): 4770-92.
60. Huang, Jingfeng, Shobha Kondragunta, Istvan Laszlo, Hongqing Liu, Lorraine Remer, Hai Zhang, Stephen Superczynski, P. Ciren, Brent N. Holben, and Maksym Petrenko. *Validation and Expected Error*

Estimation of Suomi-Npp Viirs Aerosol Optical Thickness and Ångström Exponent with Aeronet: Validation of Viirs Aerosol Products. Vol. 121, 2016.
61. Kondragunta, Shobha, Istvan Laszlo, P. Ciren, Hai Zhang, Hongqing Liu, Jingfeng Huang, and Amy Huff. *Exceptional Events Monitoring Using S-Npp Viirs Aerosol Products*, 2017.
62. Yu, Tao, Wen Wang, P. Ciren, and Rui Sun. *An Assessment of Air-Quality Monitoring Station Locations Based on Satellite Observations*, 2018.
63. Zhang, Hai, Shobha Kondragunta, Istvan Laszlo, Hongqing Liu, Lorraine Remer, Jingfeng Huang, Stephen Superczynski, and P. Ciren. *An Enhanced Viirs Aerosol Optical Thickness (Aot) Retrieval Algorithm over Land Using a Global Surface Reflectance Ratio Database: Enhanced Viirs Aot Retrieval Alg. Land*, 2016.
64. Pavolonis, Michael J., Andrew K. Heidinger, and Justin Sieglaff. "Automated Retrievals of Volcanic Ash and Dust Cloud Properties from Upwelling Infrared Measurements." *Journal of Geophysical Research: Atmospheres* 118, no. 3 (2013): 1436-58.
65. Giglio, Louis, Jacques Descloitres, Christopher O. Justice, and Yoram J. Kaufman. "An Enhanced Contextual Fire Detection Algorithm for Modis." *Remote Sensing of Environment* 87, no. 2-3 (2003): 273-82.
66. Kaufman, Yoram J., Christopher O. Justice, Luke P. Flynn, Jackie D. Kendall, Elaine M. Prins, Louis Giglio, Darold E. Ward, W. Paul Menzel, and Alberto W. Setzer. "Potential Global Fire Monitoring from Eos-Modis." *Journal of Geophysical Research: Atmospheres* 103, no. D24 (1998): 32215-38.
67. Huff, A. K., S. Kondragunta, H. Zhang, and R. M. Hoff. "Monitoring the Impacts of Wildfires on Forest Ecosystems and Public Health in the Exo-Urban Environment Using High-Resolution Satellite Aerosol Products from the Visible Infrared Imaging Radiometer Suite (Viirs)." *Environ Health Insights* 9, no. Suppl 2 (2015): 9-18.
68. OSPO, NOAA. "The Blended Global Biomass Burning Emissions Product (Gbbepx V2)." http://www.ospo.noaa.gov/Products/land/gbbepx/index.html (accessed January 23).
69. NOAA, STAR. "Enhanced Infusing Satellite Data into Environmental Applications." http://www.star.nesdis.noaa.gov/smcd/spb/aq/eidea (accessed January 23).
70. Key, Jeffrey R., Robert Mahoney, Yinghui Liu, Peter Romanov, Mark Tschudi, Igor Appel, James Maslanik, Dan Baldwin, Xuanji Wang, and Paul Meade. "Snow and Ice Products from Suomi Npp Viirs." *Journal of Geophysical Research: Atmospheres* 118, no. 23 (2013): 12,816-12,30.
71. Liu, Yinghui, Jeffrey Key, Mark Tschudi, Richard Dworak, Robert Mahoney, and Daniel Baldwin. "Validation of the Suomi Npp Viirs Ice Surface Temperature Environmental Data Record." *Remote Sensing* 7, no. 12 (2015): 17258-71.
72. Wang, Xuanji, Jeffrey Key, Ron Kwok, and Jinlun Zhang. "Comparison of Arctic Sea Ice Thickness from Satellites, Aircraft, and Piomas Data." *Remote Sensing* 8, no. 9 (2016).
73. Liu, Yinghui, Jeffrey Key, and Robert Mahoney. "Sea and Freshwater Ice Concentration from Viirs on Suomi Npp and the Future Jpss Satellites." *Remote Sensing* 8, no. 6 (2016).
74. Weng, F., X. Zou, X. Wang, S. Yang, and M. D. Goldberg. "Introduction to Suomi National Polar-Orbiting Partnership Advanced Technology Microwave Sounder for Numerical Weather Prediction and Tropical Cyclone Applications." *Journal of Geophysical Research: Atmospheres* 117, no. D19 (2012): n/a-n/a.
75. Zou, X., F. Weng, B. Zhang, L. Lin, Z. Qin, and V. Tallapragada. "Impacts of Assimilation of Atms Data in Hwrf on Track and Intensity Forecasts of 2012 Four Landfall Hurricanes." *Journal of Geophysical Research: Atmospheres* 118, no. 20 (2013): 11,558-11,76.
76. UCAR, Unidata. "Advanced Weather Interactive Processing System." https://www.unidata.ucar.edu/software/awips2/ (accessed January 23).
77. CIMSS. "Nucaps Soundings Available in Awips Ii." http://cimss.ssec.wisc.edu/goes/blog/archives/15857 (accessed January 23).
78. Lee, Thomas F., Craig S. Nelson, Patrick Dills, Lars Peter Riishojgaard, Andy Jones, Li Li, Steven Miller, Lawrence E. Flynn, Gary Jedlovec, William McCarty, Carl Hoffman, and Gary McWilliams. "Npoess: Next-Generation Operational Global Earth Observations." *Bulletin of the American Meteorological Society* 91, no. 6 (2009): 727-40.
79. Hilton, Fiona, Raymond Armante, Thomas August, Chris Barnet, Aurelie Bouchard, Claude Camy-Peyret, Virginie Capelle, Lieven Clarisse, Cathy Clerbaux, Pierre-Francois Coheur, Andrew Collard, Cyril Crevoisier, Gaelle Dufour, David Edwards, Francois Faijan, Nadia Fourrié, Antonia Gambacorta, Mitchell Goldberg, Vincent Guidard, Daniel Hurtmans, Samuel Illingworth, Nicole Jacquinet-Husson, Tobias

Kerzenmacher, Dieter Klaes, Lydie Lavanant, Guido Masiello, Marco Matricardi, Anthony McNally, Stuart Newman, Edward Pavelin, Sebastien Payan, Eric Péquignot, Sophie Peyridieu, Thierry Phulpin, John Remedios, Peter Schlüssel, Carmine Serio, Larrabee Strow, Claudia Stubenrauch, Jonathan Taylor, David Tobin, Walter Wolf, and Daniel Zhou. "Hyperspectral Earth Observation from Iasi: Five Years of Accomplishments." *Bulletin of the American Meteorological Society* 93, no. 3 (2012): 347-70.

80. Chahine, Moustafa T., Thomas S. Pagano, Hartmut H. Aumann, Robert Atlas, Christopher Barnet, John Blaisdell, Luke Chen, Murty Divakarla, Eric J. Fetzer, Mitch Goldberg, Catherine Gautier, Stephanie Granger, Scott Hannon, Fredrick W. Irion, Ramesh Kakar, Eugenia Kalnay, Bjorn H. Lambrigtsen, Sung-Yung Lee, John Le Marshall, W. Wallace McMillan, Larry McMillin, Edward T. Olsen, Henry Revercomb, Philip Rosenkranz, William L. Smith, David Staelin, L. Larrabee Strow, Joel Susskind, David Tobin, Walter Wolf, and Lihang Zhou. "Airs." *Bulletin of the American Meteorological Society* 87, no. 7 (2006): 911-26.

81. Aumann, H. H., M. T. Chahine, C. Gautier, M. D. Goldberg, E. Kalnay, L. M. McMillin, H. Revercomb, P. W. Rosenkranz, W. L. Smith, D. H. Staelin, L. L. Strow, and J. Susskind. "Airs/Amsu/Hsb on the Aqua Mission: Design, Science Objectives, Data Products, and Processing Systems." *IEEE Transactions on Geoscience and Remote Sensing* 41, no. 2 (2003): 253-64.

82. Weng, F., and X. Zou. "Errors from Rayleigh-Jeans Approximation in Satellite Microwave Radiometer Calibration Systems." *Appl Opt* 52, no. 3 (2013): 505-8.

83. Susskind, Joel, Chris Barnet, John Blaisdell, Lena Iredell, Fricky Keita, Lou Kouvaris, Gyula Molnar, and Moustafa Chahine. "Accuracy of Geophysical Parameters Derived from Atmospheric Infrared Sounder/Advanced Microwave Sounding Unit as a Function of Fractional Cloud Cover." *Journal of Geophysical Research: Atmospheres* 111, no. D9 (2006).

84. Gambacorta Antonia., Nalli, N. R., Barnet, C. D., Tan, C., Iturbide-sanchez, F., and Zhang, K. "The Noaa Unique Combined Atmospheric Processing System (Nucaps) Algorithm Theoretical Basis Document:." https://www.star.nesdis.noaa.gov/jpss/documents/ATBD/ATBD_NUCAPS_v2.0.pdf (accessed February 26, 2019).

85. Boukabara, Sid-Ahmed, Kevin Garrett, Wanchun Chen, Flavio Iturbide-Sanchez, Christopher Grassotti, Cezar Kongoli, Ruiyue Chen, Quanhua Liu, Banghua Yan, Fuzhong Weng, Ralph Ferraro, Thomas J. Kleespies, and Huan Meng. "Mirs: An All-Weather 1dvar Satellite Data Assimilation and Retrieval System." *IEEE Transactions on Geoscience and Remote Sensing* 49, no. 9 (2011): 3249-72.

86. Zhang, Kexin, Mitchell D. Goldberg, Fengying Sun, Lihang Zhou, Walter W. Wolf, Changyi Tan, Nicholas R. Nalli, and Quanhua Liu. "Estimation of near-Real-Time Outgoing Longwave Radiation from Cross-Track Infrared Sounder (Cris) Radiance Measurements." *Journal of Atmospheric and Oceanic Technology* 34, no. 3 (2017): 643-55.

87. Gambacorta, Antonia, Christopher Barnet, Walter Wolf, Thomas King, Eric Maddy, Larrabee Strow, Xiaozhen Xiong, Nicholas Nalli, and Mitch Goldberg. *An Experiment Using High Spectral Resolution Cris Measurements for Atmospheric Trace Gases: Carbon Monoxide Retrieval Impact Study*. Vol. 11, 2014.

88. Barnet, Chris. "Use of Cris Radiances at Noaa." In *NOAA Satellite Conference*. The City College of New York, New York, https://www.satelliteconferences.noaa.gov/2017/doc/presentation/wednesday/NSC2017_Session_17.2_Barnet.pdf, 2017.

89. Divakarla, Murty G., Chris D. Barnet, Mitchell D. Goldberg, Larry M. McMillin, Eric Maddy, Walter Wolf, Lihang Zhou, and Xingpin Liu. "Validation of Atmospheric Infrared Sounder Temperature and Water Vapor Retrievals with Matched Radiosonde Measurements and Forecasts." *Journal of Geophysical Research* 111, no. D9 (2006).

90. Divakarla, Murty, Christopher Barnet, Mitchell Goldberg, Eric Maddy, Fredrick Irion, Mike Newchurch, Xingpin Liu, Walter Wolf, Lawrence Flynn, Gordon Labow, Xiaozhen Xiong, Jennifer Wei, and Lihang Zhou. "Evaluation of Atmospheric Infrared Sounder Ozone Profiles and Total Ozone Retrievals with Matched Ozonesonde Measurements, Ecmwf Ozone Data, and Ozone Monitoring Instrument Retrievals." *Journal of Geophysical Research* 113, no. D15 (2008).

91. Divakarla, Murty, Antonia Gambacorta, Christopher Barnet, Mitchell Goldberg, Eric Maddy, Tom King, Walter Wolf, Nick Nalli, Kexin Zhang, and Hua Xie. "Validation of Iasi Temperature and Water Vapor Retrievals with Global Radiosonde Measurements and Model Forecasts." Paper presented at the Imaging and Applied Optics, Toronto, 2011/07/10 2011.

92. Nalli, N. R., A. Gambacorta, Q. Liu, C. D. Barnet, C. Tan, F. Iturbide-Sanchez, T. Reale, B. Sun, M. Wilson, L. Borg, and V. R. Morris. "Validation of Atmospheric Profile Retrievals from the Snpp Noaa-Unique Combined Atmospheric Processing System. Part 1: Temperature and Moisture." *IEEE Transactions on Geoscience and Remote Sensing* 56, no. 1 (2018): 180-90.
93. Nalli, Nicholas R., Christopher D. Barnet, Anthony Reale, David Tobin, Antonia Gambacorta, Eric S. Maddy, Everette Joseph, Bomin Sun, Lori Borg, Andrew K. Mollner, Vernon R. Morris, Xu Liu, Murty Divakarla, Peter J. Minnett, Robert O. Knuteson, Thomas S. King, and Walter W. Wolf. "Validation of Satellite Sounder Environmental Data Records: Application to the Cross-Track Infrared Microwave Sounder Suite." *Journal of Geophysical Research: Atmospheres* 118, no. 24 (2013): 13,628-13,43.
94. Nalli, N. R., A. Gambacorta, Q. Liu, C. Tan, F. Iturbide-Sanchez, C. D. Barnet, E. Joseph, V. R. Morris, M. Oyola, and J. W. Smith. "Validation of Atmospheric Profile Retrievals from the Snpp Noaa-Unique Combined Atmospheric Processing System. Part 2: Ozone." *IEEE Transactions on Geoscience and Remote Sensing* 56, no. 1 (2018): 598-607.
95. Sun, B., A. Reale, F. H. Tilley, M. E. Pettey, N. R. Nalli, and C. D. Barnet. "Assessment of Nucaps S-Npp Cris/Atms Sounding Products Using Reference and Conventional Radiosonde Observations." *IEEE Journal of Selected Topics in Applied Earth Observations and Remote Sensing* 10, no. 6 (2017): 2499-509.
96. Reale, Tony, Bomin Sun, Franklin H. Tilley, and Michael Pettey. "The Noaa Products Validation System (Nprovs)." *Journal of Atmospheric and Oceanic Technology* 29, no. 5 (2012): 629-45.
97. Boukabara, S. A., K. Garrett, C. Grassotti, F. Iturbide-Sanchez, W. Chen, Z. Jiang, S. A. Clough, X. Zhan, P. Liang, Q. Liu, T. Islam, V. Zubko, and A. Mims. "A Physical Approach for a Simultaneous Retrieval of Sounding, Surface, Hydrometeor, and Cryospheric Parameters from Snpp/Atms." *Journal of Geophysical Research: Atmospheres* 118, no. 22 (2013): 12,600-12,19.
98. Meng, Huan, Jun Dong, Ralph Ferraro, Banghua Yan, Limin Zhao, Cezar Kongoli, Nai-Yu Wang, and Bradley Zavodsky. "A 1dvar-Based Snowfall Rate Retrieval Algorithm for Passive Microwave Radiometers." *Journal of Geophysical Research: Atmospheres* 122, no. 12 (2017): 6520-40.
99. Bhartia, P. K., R. D. McPeters, L. E. Flynn, S. Taylor, N. A. Kramarova, S. Frith, B. Fisher, and M. DeLand. "Solar Backscatter Uv (Sbuv) Total Ozone and Profile Algorithm." *Atmospheric Measurement Techniques* 6, no. 10 (2013): 2533-48.
100. McPeters, Richard D., Scott J. Janz, Ernest Hilsenrath, Tammy L. Brown, David E. Flittner, and Donald F. Heath. "The Retrieval of O3profiles from Limb Scatter Measurements: Results from the Shuttle Ozone Limb Sounding Experiment." *Geophysical Research Letters* 27, no. 17 (2000): 2597-600.
101. Flynn, L., C. Long, X. Wu, R. Evans, C. T. Beck, I. Petropavlovskikh, G. McConville, W. Yu, Z. Zhang, J. Niu, E. Beach, Y. Hao, C. Pan, B. Sen, M. Novicki, S. Zhou, and C. Seftor. "Performance of the Ozone Mapping and Profiler Suite (Omps) Products." *Journal of Geophysical Research: Atmospheres* 119, no. 10 (2014): 6181-95.
102. Flynn, Larry. "Jpss-Cpo Tim: Omps Products Summary " https://www.star.nesdis.noaa.gov/jpss/documents/meetings/2016/JPSS_CPO/2.2_Flynn_OMPS-Products.pdf (accessed February 26, 2019).
103. NWS. "Climate Prediction Center - Stratosphere: Omps Total Ozone." https://www.cpc.ncep.noaa.gov/products/stratosphere/omps/ (accessed February 26).
104. Imaoka, K., M. Kachi, M. Kasahara, N. Ito, K. Nakagawa, and T. Oki. "Instrument Performance and Calibration of Amsr-E and Amsr2." *International Archives of the Photogrammetry, Remote Sensing and Spatial Information Science* XXXVIII, Part 8, (2010): 13-16.
105. Chang, P., Z. Jelenak, S. Alsweiss, S. Soisuvarn, P. Meyers, and R. Ferraro. "An Overview of Noaa's Gcom-W1/Amsr-2 Product Processing and Utilization." Paper presented at the 2017 IEEE International Geoscience and Remote Sensing Symposium (IGARSS), 23-28 July 2017 2017.
106. Ferraro, Ralph, Patrick Meyers, Paul Chang, Zorana Jelenak, Christopher Grassotti, and Shuyan Liu. "Application of Gcom-W Amsr2 and S-Npp Atms Hydrological Products to a Flooding Event in the United States." *IEEE Journal of Selected Topics in Applied Earth Observations and Remote Sensing* 10, no. 9 (2017): 3884-91.
107. Lihang Zhou, M. Divakarla, H. Archambault, Annarita Mariotti, and Haun Meng. "Exploring Jpss Data Application for Earth System Data Assimilation." NOAA JPSS-STAR (JSTAR) Website https://www.star.nesdis.noaa.gov/jpss/documents/meetings/2017/JPSS_CPO_MAPP/JPSS_CPO_MAPP_REPORT.pdf, 2017.

108. NOAA, STAR. "Integrated Calibration and Validation System Long-Term Monitoring." https://www.star.nesdis.noaa.gov/icvs/ (accessed January 23).
109. NOAA. "Star Jpss Environmental Data Records: Product Monitoring for Weather, Climate, and Environmental Applications." https://www.star.nesdis.noaa.gov/jpss/EDRs/ (accessed January 23).
110. NOAA, STAR. "Jpss Mapper for near Real-Time Environmental Monitoring and Applications." https://www.star.nesdis.noaa.gov/jpss/mapper (accessed January 23).
111. STAR. "S-Npp Reprocessed Sensor Data Records " http://jlrdata.umd.edu/opendap/thredds (accessed January 23).
112. Goldberg, M. D., Y. Qu, L. M. McMillin, W. Wolf, Zhou Lihang, and M. Divakarla. "Airs near-Real-Time Products and Algorithms in Support of Operational Numerical Weather Prediction." *IEEE Transactions on Geoscience and Remote Sensing* 41, no. 2 (2003): 379-89.
113. NOAA. "Jpss Science Seminar Annual Digest Publications." http://www.jpss.noaa.gov/assets/pdfs/science_publications/ (accessed January 23).

Bibliography

Alvarado, M., Andrews, A., Barnet, C., Bowman, K., Cady-Pereira, K., De Gouw, J., Fahey, D., Fischer, E., Gambacorta, A., Jones, D., Karion, A., Kim, S.-W., Liu, Q., Mao, J., Merrelli, A., Millet, D., Nalli, N., Neuman, A., Nowak, J., Payne, V., Pierce, B., Rosenlof, K., Saikawa, E., Sharma, A., Shephard, M., Smith, N., Sweeney, C., Tong, D., Wong, J., Warner, J., Wolf, W., Worden, H., Xiong, X., Yurganov, L., & Zhu, L. (2015). Advancing atmospheric chemistry through the use of satellite observations from the Cross-track Infrared Sounder (CrIS): CrIS Atmospheric Chemistry Data User's Workshop report, Sept. 18-19, 2014, College Park, MD. doi:10.7289/V50V89SS.

Aumann, H. H., Chahine, M. T., Gautier, C., Goldberg, M. D., Kalnay, E., McMillin, L. M., … Susskind, J. (2003). AIRS/AMSU/HSB on the Aqua mission: design, science objectives, data products, and processing systems. IEEE Transactions on Geoscience and Remote Sensing, 41(2), 253–264. JOUR. https://doi.org/10.1109/TGRS.2002.808356.

Aumann, H. H., and Thomas S. Pagano, T. S. (2008). Using AIRS and IASI data to evaluate absolute radiometric accuracy and stability for climate applications", Proc. SPIE 7085, Atmospheric and Environmental Remote Sensing Data Processing and Utilization IV: Readiness for GEOSS II, 708504. https://doi.org/10.1117/12.795225.

Backus, G., and Gilbert, F. (1968) The resolving power of gross Earth data. Geophys. J. R. astr.Soc. v.16 p.169-205.

Bergamaschi, P., Houweling ,S., Segers, A., Krol, M., Frankenberg, C., Scheepmaker, R. A., Dlugokencky E., Wofsy, S. C., Kort, E. A., Sweeney, C., Schuck, T., Brenninkmeijer, C., Chen, H., Beck, V., and Gerbig, C. (2013). Atmospheric CH_4 in the first decade of the 21st

century: Inverse modeling analysis using SCIAMACHY satellite retrievals and NOAA surface
measurements, J. Geophys. Res. Atmos., 118, 7350–7369, doi:10.1002/jgrd.50480.

Bergamaschi, P., A. Danila, R. F. Weiss, P. Ciais, R. L. Thompson, D. Brunner, I. Levin, Y. Meijer, F. Chevallier, G. Janssens-Maenhout, H. Bovensmann, D. Crisp, S. Basu, E. Dlugokencky, R. Engelen, C. Gerbig, D. Günther, S. Hammer, S. Henne, S. Houweling, U.
Karstens, E. Kort, M. Maione, A. J. Manning, J. Miller, S. Montzka, S. Pandey, W. Peters, P.
Peylin, B. Pinty, M. Ramonet, S. Reimann, T. Röckmann, M. Schmidt, M. Strogies, J. Sussams, O. Tarasova, J. van Aardenne, A. T. Vermeulen, F. Vogel. (2018). Atmospheric monitoring
and inverse modelling for verification of greenhouse gas inventories, EUR 29276 EN, Publications Office of the European Union, Luxembourg, ISBN 978-92-79-88938-7, doi:10.2760/759928, JRC111789.

Boers, N., Marwan, N., Barbosa, H. M. J. & Kurths, J. A deforestation-induced tipping point for the South American monsoon system. Sci. Rep. 7, 41489 (2017).

Boulton, C.A., Lenton, T.M. & Boers, N. (2022). Pronounced loss of Amazon rainforest resilience since the early 2000s. Nat. Clim. Chang. 12, 271–278. https://doi.org/10.1038/s41558-022-01287-8

Bruhwiler, L., Parmentier, FJ.W., Crill, P. et al. (2021). The Arctic Carbon Cycle and Its Response to Changing Climate. Curr Clim Change Rep 7, 14–34. https://doi.org/10.1007/s40641-020-00169-5.

Buchholz, R. R., Emmons, L. K., Tilmes, S., & the CESM2 development team (2019). CESM2.1/CAM-chem instantaneous output for boundary conditions. UCAR/NCAR - Atmospheric Chemistry Observations and Modeling Laboratory. Accessed 1 June 2019, https://doi.org/10.5065/NMP7-EP60.

Budyko, M.I. (1969). "The effect of solar radiation variations on the climate of the Earth". Tellus. 21 (5): 611–9. doi:10.3402/tellusa. v21i5.10109. S2CID 21745322.

Conrath, B.J. (1972). Vertical resolution of temperature profiles obtained from remote radiation measurements. J. Atmos. Sci., 29, 1262–1271.

Chahine, M. T., Pagano, T. S., Aumann, H. H., Atlas, R., Barnet, C., Blaisdell, J., Chen, L., Divakarla, M., Fetzer, E. J., Goldberg, M., Gautier, C., Granger, S., Hannon, S., Irion, F. W., Kakar, R., Kalnay, E., Lambrigtsen, B. H., Lee, S., Le Marshall, J., Mcmillan, W. W., Mcmillin, L., Olsen, E. T., Revercomb, H., Rosenkranz, P., Smith, W. L., Staelin, D., Strow, L. L., Susskind, J., Tobin, D., Wolf, W., & Zhou, L. (2006). AIRS, Bulletin of the American Meteorological Society, 87(7), 911-926.

Chandra, N., P. K. Patra, J. S. H. Bisht, A. Ito, T. Umezawa, N. Saigusa, S. Morimoto, S. Aoki, G. Janssens-Maenhout, R. Fujita, M. Takigawa, S. Watanabe, N. Saitoh, and J. G. Canadell, 2021: Emissions from the oil and gas sectors, coal mining and ruminant farming drive methane growth over the past three decades. J. Meteor. Soc. Japan, 99, 309–337, doi:10.2151/jmsj.2021-015.

Chelliah, M. and Arkin P., 1992: Large-Scale Interannual Variability of Monthly Outgoing Longware Radiation Anomalies over the Global Tropics. J. Climate, 5, 371-389.

Chiodi, A. M., and Harrison, D. E. (2010). Characterizing warm-ENSO variability in the equatorial Pacific: An OLR perspective. J. Climate, 23, 2428–2439.

Christy, J. R.; Spencer, R. W.; Norris, W. B.; Braswell, W. D. (2003). Error estimates of version 5.0 of MSU-AMSU bulk atmospheric temperature. J. Atmos. Oceanic Technol. 20(5), 613–629.

Chu, P.S., and Wang, J. B. (1997). Recent climate change in the tropical western Pacific and Indian Ocean regions as detected by outgoing longwave radiation records. J. Climate, 10, 636–646, https://doi.org/10.1175/1520-0442

Clerbaux, N.; Akkermans, T.; Baudrez, E.; Velazquez Blazquez, A.; Moutier, W.; Moreels, J.; Aebi, C. (2020). The Climate Monitoring SAF Outgoing Longwave Radiation from AVHRR. Remote Sens., 12, 929.

Cressot, C., Chevallier, F., Bousquet, P., Crevoisier, C., Dlugokencky, E. J., Fortems-Cheiney, A., Frankenberg, C., Parker, R., Pison, I., Scheepmaker, R. A., Montzka, S. A., Krummel, P. B., Steele, L. P., and Langenfelds, R. L. (2014). On the consistency between global and regional

methane emissions inferred from SCIAMACHY, TANSO-FTS, IASI and surface measurements, Atmos. Chem. Phys., 14, 577-592, 2014, doi:10.5194/acp-14-577-2014.

Conrath, B.J. (1972) Vertical resolution of temperature profiles obtained from remote radiation measurements. J. Atmos. Sci. v.29 p.1262-1271.

Covey, K., Soper, F., Pangala, S., Bernardino, A., Pagliaro, Z., Basso, L., … Elmore, A. (2021). Carbon and beyond: The biogeochemistry of climate in a rapidly changing Amazon. Frontiers in Forests and Global Change, 4, 618401. doi:10.3389/ffgc.2021.618401

Crisp, D., Meijer, Y., Munro, R., Bowman, K. and Chatterjee, A. (2018). A constellation architecture for monitoring carbon dioxide and methane from space.

Crevoisier, C., Nobileau, D., Fiore, A.M., Armante, R., Chédin, A., & Scott, N.A. (2009). Tropospheric methane in the tropics – first year from IASI hyperspectral infrared observations. Atmospheric Chemistry and Physics, 9, 6337-6350.

Crevoisier, C. (2018). Use of Hyperspectral Infrared Radiances to Infer Atmospheric Trace Gases, Editor(s): Shunlin Liang, Comprehensive Remote Sensing, Elsevier, 2018, Pages 345-387, ISBN 9780128032213, https://doi.org/10.1016/B978-0-12-409548-9.10396-3.

Denman, K.L., et al. (2007) Couplings between Changes in the Climate System and Biogeochemistry. Climate Change 2007: The Physical Science Basis. In: Solomon, S., et al., Eds., Contribution of Working Group I to the Fourth Assessment Report of the Intergovernmental Panel on Climate Change, Cambridge University Press, Cambridge, 500-587.

Dewitte,S.; Clerbaux,N. (2018). Decadal Changes of Earth's Outgoing Longwave Radiation. Remote Sens. 10, 1539.

Dimdore-Miles, O. B., Palmer, P. I., and Bruhwiler, L. P. (2018). Detecting changes in Arctic methane emissions: limitations of the inter-polar difference of atmospheric mole fractions, Atmos. Chem. Phys., 18, 17895–17907, https://doi.org/10.5194/acp-18-17895-2018.

Divakarla, M. G., Barnet, C. D., Goldberg, M. D., McMillin, L. M., Maddy, E., Wolf, W., Zhou, L., and Liu, X. (2006), Validation of Atmospheric Infrared Sounder temperature and water vapor retrievals with matched radiosonde measurements and forecasts, J. Geophys. Res., 111, D09S15, doi:10.1029/2005JD006116.

Dlugokencky, E. J., L. P. Steele, P. M. Lang, and K. A. Masarie. "The Growth Rate and Distribution of Atmospheric Methane." Journal of Geophysical Research 99 (1994): 17,021-17,43.

Dlugokencky, E. J., Houweling, S., Bruhwiler, L., Masarie, K. A., Lang, P. M., Miller, J. B., and Tans, P. P. (2003). Atmospheric methane levels off: Temporary pause or a new steady-state? Geophys. Res. Lett., 30, 1992–1995, https://doi.org/10.1029/2003GL018126

Dlugokencky, E. J., Bruhwiler, L., White, J. W., Emmons, L. K., Novelli, P. C., Montzka, S. A., Masarie, K. A., Lang, P. M., Crotwell, A. M., Miller, J. B., and Gatti, L. V. (2009). Observational constraints on recent increases in the atmospheric CH 4 burden, Geophys. Res. Lett., 36, 3–7, https://doi.org/10.1029/2009GL039780

Dlugokencky, E.J., A.M. Crotwell, J.W. Mund, M.J. Crotwell, and K.W. Thoning (2019), Atmospheric CH_4 Dry Air Mole Fractions from the NOAA ESRL Carbon Cycle Cooperative Global Air Sampling Network, 1983-2018, Version: 2019-07, https://doi.org/10.15138/VNCZ-M766

Ellingson,R.G.; Yanuk, D.J.; Lee, H.T.; Gruber,A.A. (1989).Technique for estimating outgoing longwave radiation from HIRS radiance observations. J. Atmos. Ocean. Technol., 6, 706–711.

Etheridge, D. M., Steele, L. P., Francey, R. J., and Langenfelds, R. L. (1998). Atmospheric methane between 1000 A.D. and present: Evidence of anthropogenic emissions and climatic variability, J. Geophys. Res., 103 (D13), 15979– 15993, doi:10.1029/98JD00923.

Emmons, L. K., Walters, S., Hess, P. G., Lamarque, J. F., Pfister, G. G., Fillmore, D., Granier, C., Guenther, A., Kinnison, D., Laepple, T., Orlando, J., Tie, X., Tyndall, G., Wiedinmyer, C., Baughcum, S. L., & Kloster, S. (2010). Description and evaluation of the Model for Ozone and Related chemical Tracers, version 4 (MOZART-4). Geoscientific Model Development, 3(1), 43– 67. https://doi.org/10.5194/gmd-3-43-2010

Emmons, L. K., Schwantes, R. H., Orlando, J. J., Tyndall, G., Kinnison, D., Lamarque, J.-F., et al. (2020). The Chemistry Mechanism in the Community Earth System Model version 2 (CESM2). Journal of Advances in Modeling Earth Systems, 12, e2019MS001882. https://doi.org/10.1029/2019MS001882

Fetzer, E. J., Olsen, E., and Chen, L. (2003). Validation of AIRS/AMSU/HSB retrieved products", Proc. SPIE 5151, Earth Observing Systems VIII. https://doi.org/10.1117/12.506328

Fetzer, E. J., Lambrigtsen, B. H., Eldering, A., Aumann, H. H., and Chahine, M. T. (2006), Biases in total precipitable water vapor climatologies from Atmospheric Infrared Sounder and Advanced Microwave Scanning Radiometer, J. Geophys. Res., 111, D09S16, doi:10.1029/2005JD006598.

Frankenberg, C., Aben, I., Bergamaschi, P., Dlugokencky, E. J., Van Hees, R., Houweling, S., Van Der Meer, P., Snel, R., and Tol, P. (2011). Global column-averaged methane mixing ratios from 2003 to 2009 as derived from SCIAMACHY: Trends and variability, J. Geophys. Res.-Atmos., 116, 1–12, https://doi.org/10.1029/2010JD014849, 2011.

Fung, I., John, J., Lerner, J., Matthews, E., Prather, M., Steele, L. P., and Fraser, P. J. (1991), Three-dimensional model synthesis of the global methane cycle, J. Geophys. Res., 96(D7), 13033– 13065, doi:10.1029/91JD01247.

Gambacorta, A.; Barnet, C.; Wolf, W.; Goldberg, M.; King, T.; Nalli, N.; Maddy, E.; Xiong, X.; Divakarla, M. (2012). The NOAA Unique CrIS/ATMS Processing System (NUCAPS): First light retrieval results. Proceedings of ITSC-XVIII; International TOVS Working Group (ITWG).

Gambacorta, A.; Barnet, C. (2013). Methodology and information content of the NOAA NESDIS operational channel selection for the Cross-Track Infrared Sounder (CrIS). IEEE Trans. Geosci. Remote Sensing, 51, 3207–3216. doi:10.1109/TGRS.2012.2220369.

Gambacorta, A.; Barnet, C.; Wolf, W.; King, T.; Maddy, E.; Strow, L.; Xiong, X.; Nalli, N.; Goldberg, M. (2014). An experiment using high spectral resolution CrIS measurements for atmospheric trace gases: Carbon monoxide retrieval impact study. IEEE Geosci. Remote Sensing Lett. 2014, 11, 1639–1643. doi:10.1109/LGRS.2014.2303641.

Ganesan, A. L., Stell, A. C., Gedney, N., Comyn-Platt, E., Hayman, G., Rigby, M., Poulter, B., and Hornibrook, E. R.: Spatially Resolved Isotopic Source Signatures of Wetland Methane Emissions, Geophys. Res. Lett., 45, 3737–3745, https://doi.org/10.1002/2018GL077536, 2018.

Ganesan, A. L., Schwietzke, S., Poulter, B., Arnold, T., Lan, X., Rigby, M., Vogel, F. R., van der Werf, G. R., Janssens-Maenhout, G., Boesch, H., Pandey, S., Manning, A. J., Jackson, R. B., Nisbet, E. G., and Manning, M. R.: Advancing Scientific Understanding of the Global Methane Budget in Support of the Paris Agreement, Global Biogeochem. Cycles, 33, 1475–1512, https://doi.org/10.1029/2018GB006065, 2019.

Goldberg, M. D., Kilcoyne, H., Cikanek, H., & Mehta, A. (2013). Joint Polar Satellite System: The United States next generation civilian polar-orbiting environmental satellite system. Journal of Geophysical Research: Atmospheres, 118(October), 13463–13475. https://doi.org/10.1002/2013JD020389

Goldberg, M.; Cikanek, H.A.; Zhou, L.; Price, J. *The Joint Polar Satellite System in Comprehensive Remote Sensing: Missions and Sensors*; Liang, S., Ed.; Elsevier: Lanham, MD, USA, 2018; Volume 1.

Goldberg, M. D., Qu, Y., McMillin, L. M., Wolf, W., Zhou, L., and Divakarla, M. (2003). AIRS Near Real-Time Products and Algorithms in Support of Operational Numerical Weather Prediction, IEEE Transactions on Geoscience and Remote Sensing 41, No. 2, 379-389.

Han, Y.; Revercomb, H.; Cromp, M.; Gu, D.; Johnson, D.; Mooney, D.; Scott, D.; Strow, L.; Bingham, G.; Borg, L.; et al. Suomi NPP CrIS measurements, sensor data record algorithm, calibration and validation activities, and record data quality. J. Geophys. Res. Atmos. 2013, 118, 12734–12748.

Han, Y.; Chen, Y. Calibration Algorithm for Cross-Track Infrared Sounder Full Spectral Resolution Measurements. IEEE Trans. Geosci. Remote Sens. 2018, 56, 1008–1016.

Hilton et al., 2012 F. Hilton, T. August, C. Barnet, A. Bouchard, C. Camy-Peyret, L. Clarisse, C. Clerbaux, P.-F. Coheur, A. Collard, C. Crevoisier, G. Dufour, D. Edwards, F. Faijan, N. Fourrié, A. Gambacorta, S. Gauguin, V. Guidard, D. Hurtmans, S. Illingworth, N. Jacquinet-Husson, T. Kerzenmacher, D. Klaes, L. Lavanant, G. Masiello, M. Matricardi, T. McNally, S. Newman, E. Pavelin, E. Péquignot, T. Phulpin, J. Remedios, P. Schlüssel, C. Serio, L. Strow, J. Taylor, D. Tobin, A. Uspensky, D. Zhou, Hyperspectral earth observation from IASI: five years of accomplishments Bull. Am. Meteorol. Soc., 93 (3) (2012), pp. 347-370, 10.1175/BAMS-D-11-00027.IPCC. Climate change: the IPCC scientific assessment. In: Houghton JT, Jenkins GJ, Ephraums JJ, editors. Report prepared for IPCC by working group 1. Cambridge: Cambridge University Press; 1990. p. 365.

Huang, H., & Antonelli, P. (2001). Application of Principal Component Analysis to High-Resolution Infrared Measurement Compression and Retrieval, Journal of Applied Meteorology, 40(3), 365-388.

IPCC. Climate change 2001: the scientific basis. In: Houghton JT, Ding Y, Griggs DJ, Noguer M, van der Linden PJ, Dai X, Maskell K, Johnson CA, editors. Contribution of working group I to the third assessment report of the intergovernmental panel on climate change. Cambridge: Cambridge University Press; 2001. p. 881.

IPCC (2013). Climate Change 2013: The Physical Science Basis.EContribution of Working Group I to the Fifth Assessment Report of the Intergovernmental Panel on Climate Change. [Stocker, T. F., D. Qin, G.-K. Plattner, M. Tignor, S. K. Allen, J. Boschung, A. Nauels, Y. Xia, V. Bex and P. M. Midgley (eds.)]. Cambridge University Press, Cambridge, United Kingdom and New York, NY, USA, 1585 pp.

IPCC, 2014: Climate Change 2014: Synthesis Report. Contribution of Working Groups I, II and III to the Fifth Assessment Report of the Intergovernmental Panel on Climate Change [Core Writing Team, R.K. Pachauri and L.A. Meyer (eds.)]. IPCC, Geneva, Switzerland, 151 pp.

IPCC 2021: Climate Change 2021: The Physical Science Basis. Contribution of Working Group I to the Sixth Assessment Report of the Intergovernmental Panel on Climate Change [Masson-Delmotte, V., P. Zhai, A. Pirani, S.L. Connors, C. Péan, S. Berger, N. Caud, Y. Chen, L. Goldfarb, M.I. Gomis, M. Huang, K. Leitzell, E. Lonnoy, J.B.R. Matthews, T.K. Maycock, T. Waterfield, O. Yelekçi, R. Yu, and B. Zhou (eds.)]. Cambridge University Press. In the Press.

Iturbide-Sanchez F., et al., "Recalibration and Assessment of the SNPP CrIS Instrument: A Successful History of Restoration After Midwave Infrared Band Anomaly," in IEEE Transactions on Geoscience and Remote Sensing, vol. 60, pp. 1-21, 2022, Art no. 5514421, doi: 10.1109/TGRS.2021.3112400.

Jackson, R. B., Saunois, M., Bousquet, P., Canadell, J. G., Poulter, B., Stavert, A. R., Bergamaschi, P., Niwa, Y., Segers, A., and Tsuruta, A.: Increasing anthropogenic methane emissions arise equally from agricultural and fossil fuel sources, Environ. Res. Lett., in press, https://doi.org/10.1088/1748-9326/ab9ed2, 2020.

Jacob, D. J., Turner, A. J., Maasakkers, J. D., Sheng, J., Sun, K., Liu, X., Chance, K., Aben, I., McKeever, J., and Frankenberg, C.: Satellite observations of atmospheric methane and their value for quantifying methane emissions, Atmos. Chem. Phys., 16, 14371–14396, https://doi.org/10.5194/acp-16-14371-2016, 2016.

Kahn, B. H., Irion, F. W., Dang, V. T., Manning, E. M., Nasiri, S. L., Naud, C. M., Blaisdell, J. M., Schreier, M. M., Yue, Q., Bowman, K. W., Fetzer, E. J., Hulley, G. C., Liou, K. N., Lubin, D., Ou, S. C., Susskind, J., Takano, Y., Tian, B., Worden, J. R.. 2014. The Atmospheric Infrared Sounder version 6 cloud products. Atmos. Chem. Phys.. Vol. 14, No. 1, pp. 399-426. DOI: 10.5194/acp-14-399-2014 ISSN: 1680-7324

Kalluri, S., Barnet, C., Divakarla, M., Esmaili, R., Nalli, N., Pryor, K., Reale, T., Smith, N., Tan, C., Wang, T., Warner, J., Wilson, M., **Zhou, L**., & Zhu, T. (2022). Validation and Utility of Satellite Retrievals of Atmospheric Profiles in Detecting and Monitoring Significant Weather Events, Bulletin of the American Meteorological Society (BAMS), 103(2), E570-E590. Retrieved May 2, 2022, from https://journals.ametsoc.org/view/journals/bams/103/2/BAMS-D-20-0126.1.xml

Khalil M. A. K. and R. A. Rasmussen, Atmospheric methane: recent global trends, Environmental Science & Technology 1990 24 (4), 549-553, DOI: 10.1021/es00074a014

Kirschke, S., Bousquet, P., Ciais, P. et al. (2013). Three decades of global methane sources and sinks. Nature Geosci 6, 813–823. https://doi.org/10.1038/ngeo1955

Kroeze, C. (1992). Latitudinal and Altitudinal Distribution of Carbon Dioxide, Halocarbons, Nitrous Oxide, Methane, Carbon Monoxide and Hydroxyl in the Atmosphere. IIASA Working Paper. IIASA, Laxenburg, Austria: WP-92-038

Kulawik, S. S., Worden, J. R., Payne, V. H., Fu, D., Wofsy, S. C., McKain, K., Sweeney, C., Daube Jr., B. C., Lipton, A., Polonsky, I., He, Y., Cady-Pereira, K. E., Dlugokencky, E. J., Jacob, D. J., and Yin, Y.: Evaluation of single-footprint AIRS CH_4 profile retrieval uncertainties using aircraft profile measurements, Atmos. Meas. Tech., 14, 335–354, https://doi.org/10.5194/amt-14-335-2021, 2021.

Lamarque, J.-F., Emmons, L. K., Hess, P. G., Kinnison, D. E., Tilmes, S., Vitt, F., Heald, C. L., Holland, E. A., Lauritzen, P. H., Neu, J., Orlando, J. J., Rasch, P. J., and Tyndall, G. K. (2012). CAM-chem: description and evaluation of interactive atmospheric chemistry in the Community Earth System Model, Geosci. Model Dev., 5, 369–411, https://doi.org/10.5194/gmd-5-369-2012.

Lee, J. N., Susskind, J., Iredel, L. (2017). Changes in OLR over Arctic as Depicted by AIRS, CERES and MERRA-2, https://ntrs.nasa.gov/citations/20170011301

Lee, T.F.; Nelson, C.S.; Dills, P.; Riishojgaard, L.P.; Jones, A.; Li, L.; Miller, S.; Flynn, L.E.; Jedlovec, G.; McCarty, W.; et al. (2009). NPOESS: Next-Generation Operational Global Earth Observations. Bull. Am. Meteorol. Soc. 91, 727–740.

Lenton T. M., Rockström J, Gaffney O, Rahmstorf S, Richardson K, Steffen W, Schellnhuber HJ. Climate tipping points - too risky to bet against. Nature. (2019). 575(7784):592-595. doi: 10.1038/d41586-019-03595-0. PMID: 31776487.

Levy H. (1971). Normal atmosphere: large radical and formaldehyde concentrations predicted. Science. https://doi.org/10.1126/science.173.3992.141.

Liebmann,B.; Smith, C.A. Description of a complete (interpolated) outgoing longwave radiation dataset .Bull. Am. Meteorol. Soc. 1996, 77, 1275–1277.

Lovejoy, T. E. & Nobre, C. (2018). Amazon tipping point. Sci. Adv. 4, eaat2340.

Liu, S., Proudman, J. & Mitloehner, F.M. Rethinking methane from animal agriculture. *CABI Agric Biosci* 2, 22 (2021). https://doi.org/10.1186/s43170-021-00041-y

Loeb, N.; Doelling, D.; Wang, H.; Su, W.; Nguyen, C.; Corbett, J.; Liang, L.; Mitrescu, C.; Rose, F.; Kato, S. Clouds and the Earth's Radiant Energy System (CERES) Energy Balanced and Filled (EBAF) Top-of-Atmosphere (TOA) Edition-4.0 Data Product. J. Clim. 2018, 31, 895–918.

Loeb, N. G., Johnson, G. C., Thorsen, T. J., Lyman, J. M., Rose, F. G., & Kato, S. (2021). Satellite and ocean data reveal marked increase in Earth's heating rate. Geophysical Research Letters, 48, e2021GL093047. https://doi.org/10.1029/2021GL093047

Maddy, E. S., and C. D. Barnet (2008), Vertical resolution estimates in Version 5 of AIRS operational retrievals, IEEE Trans. Geosci. Remote Sens., 46(8), 2375–1384, doi:10.1109/TGRS.2008.917498.

Manabe, Syukoro; Wetherald, Richard T. (1975). The Effects of Doubling the CO2 Concentration on the Climate of a General Circulation Model. Journal of the Atmospheric Sciences. 32 (1): 3–15.

Massart, S. Agusti-Panareda A., Aben I., Butz A., Chevallier F., Crevoisier C., Engelen R., Frankenberg C., and Hasekamp O. (2014). Assimilation of atmospheric methane products in the

MACC-II system: from SCIAMACHY to TANSO and IASI, Atmos. Chem. Phys., 14, 6139- 6158 doi:10.5194/acp-14-6139-2014.

Mears, C. A., Schabel, M. C.; Wentz, F. J. A reanalysis of the MSU channel 2 tropospheric temperature record. J. Clim. 2003, 16, 3650–3664.

Mears, C. A.; Wentz, F. J. Sensitivity of satellite-derived tropospheric temperature trends to the diurnal cycle adjustment. J. Clim. 2016, 29, 3629–3646.

Ministry of Foreign Affairs, Ministry of Science, and Communications: Brazil's Third Biennial Update Report to the United Nations Framework Convention on Climate Change, available at: https://unfccc.int/sites/default/files/resource/2018-02-28_BRA-BUR3_ENG_FINAL.pdf (last access: 22 October 2020), 2019.

Ministry of Science and Innovation (2016). Third National Communication of Brazil to the United Nations Framework Convention on Climate Change – Volume I, available at: https://unfccc.int/sites/default/files/resource/branc3v1.pdf (last access: 22 October 2020), 2016.

Molod, A., Takacs, L., Suarez, M., & Bacmeister, J. (2015). Development of the GEOS-5 atmospheric general circulation model: Evolution from MERRA to MERRA2. Geoscientific Model Development, 8(5), 1339– 1356. https://doi.org/10.5194/gmd-8-1339-2015

Myhre G, Shindell D, Bréon FM, Collins W, Fuglestvedt J, Huang J, et al. Anthropogenic and natural radiative forcing. In: Stocker TF, Qin D, Plattner GK, Tignor M, Allen SK, Boschung J, Nauels A, Xia Y, Bex V, Midgley PM, editors. Climate change 2013: the physical science basis. contribution of working group I to the fifth assessment report of the intergovernmental panel on climate change. Geneva: IPCC; 2013a. http://www.climatechange2013.org/.

Myhre G, Shindell D, Bréon FM, Collins W, Fuglestvedt J, Huang J, et al. Anthropogenic and natural radiative forcing supplementary material; 2013b. http://www.climatechange2013.org/.

Nalli, N.R.; Barnet, C.D.; Reale, A.; Tobin, D.; Gambacorta, A.; Maddy, E.S.; Joseph, E.; Sun, B.; Borg, L.; Mollner, A.; Morris, V.R.; Divakarla, M.; Liu, X.; .; Minnett, P.J.; Knuteson, R.O.; King, T.S.; Wolf, W.W. Validation of satellite sounder environmental data records: Application to the Cross-track Infrared Microwave Sounder Suite. J. Geophys. Res. Atmos. 2013, 118, 13,628–13,643. doi:10.1002/2013JD020436.

Nalli, N.R.; Gambacorta, A.; Liu, Q.; Barnet, C.D.; Tan, C.; Iturbide-Sanchez, F.; Reale, T.; Sun, B.; .; Wilson, M.; Borg, L.; Morris, V.R. Validation of atmospheric profile retrievals from the SNPP NOAA-Unique Combined Atmospheric Processing System. Part 1: Temperature and moisture. IEEE Trans. Geosci. Remote Sensing 2018, 56, 180–190. doi:10.1109/TGRS.2017.2744558.

Nalli, N.R.; Gambacorta, A.; Liu, Q.; Tan, C.; Iturbide-Sanchez, F.; Barnet, C.D.; Joseph, E.; Morris, V.R.; Oyola, M.; Smith, J.W. Validation of atmospheric profile retrievals from the SNPP NOAA-Unique Combined Atmospheric Processing System. Part 2: Ozone. IEEE Trans. Geosci. Remote Sensing 2018, 56, 598–607. doi:10.1109/TGRS.2017.2762600.

Nalli, N.R.; Tan, C.; Warner, J.; Divakarla, M.; Gambacorta, A.; Wilson, M.; Zhu, T.; Wang, T.; Wei, Z.; Pryor, K.; Kalluri, S.; **Zhou, L**.; Sweeney, C.; Baier, B.C.; McKain, K.; Wunch, D.; Deutscher, N.M.; Hase, F.; Iraci, L.T.; Kivi, R.; Morino, I.; Notholt, J.; Ohyama, H.; Pollard, D.F.; Té, Y.; Velazco, V.A.; Warneke, T.; Sussmann, R.; Rettinger, M. Validation of Carbon Trace Gas Profile Retrievals from the NOAA-Unique Combined

Atmospheric Processing System for the Cross-Track Infrared Sounder. Remote Sens. 2020, 12, 3245. https://doi.org/10.3390/rs12193245

Nisbet, E. G., Dlugokencky, E. J., Manning, M. R., Lowry, D., Fisher, R. E., France, J. L., Michel, S. E., Miller, J. B., White, J. W., Vaughn, B., Bousquet, P., Pyle, J. A., Warwick, N. J., Cain, M., Brownlow, R., Zazzeri, G., Lanoisellé, M., Manning, A. C., Gloor, E., Worthy, D. E., Brunke, E. G., Labuschagne, C., Wolff, E. W., and Ganesan, A. L. (2016). Rising atmospheric methane: 2007–2014 growth and isotopic shift, Global Biogeochem. Cycles, 30, 1356–1370, https://doi.org/10.1002/2016GB005406.

Nisbet, E. G., Manning, M. R., Dlugokencky, E. J., Fisher, R. E., Lowry, D., Michel, S. E., Myhre, C. L., Platt, S. M., Allen, G., Bousquet, P., Brownlow, R., Cain, M., France, J. L., Hermansen, O., Hossaini, R., Jones, A. E., Levin, I., Manning, A. C., Myhre, G., Pyle, J. A., Vaughn, B. H., Warwick, N. J., and White, J. W. C. (2019). Very Strong Atmospheric Methane Growth in the 4 Years 2014–2017: Implications for the Paris Agreement, Global Biogeochem. Cycles, 33, 318–342, https://doi.org/10.1029/2018GB006009.

Nisbet, E., Fisher, R., Lowry, D., France, J., Allen, G., Bakkaloglu, S., Broderick, T., Cain, M., Coleman, M., Fernandez, J., Forster, G., Griffiths, P., Iverach, C., Kelly, B., Manning, M., Nisbet-Jones, P., Pyle, J., Townsend-Small, A., Al-Shalaan, A., Warwick, N., and Zazzeri, G. (2020). Methane mitigation: methods to reduce emissions, on the path to the Paris Agreement, Rev. Geophys., 58, e2019RG000675, https://doi.org/10.1029/2019rg000675.

NOAA Arctic Report Card (2019_https://arctic.noaa.gov/Report-Card/Report-Card-2019

Nussbaumer E A, Pinker R T. (2012). Estimating surface long-wave radiative fluxes at global scale[J]. Quarterly Journal of the Royal Meteorological Society, 138 (665): 1083- 1093. https://rmets.onlinelibrary.wiley.com/doi/full/10.1002/qj.974

Ohring, G.; Gruber, A.; Ellingson,R. Satellite determinations of the relationship between total longwave radiation flux and infrared window radiance. J. Climatol. Appl. Meteorol. 1984, 23, 416–425.

Pagano, T. S., Aumann, H. H., Hagan, D., & Overoye, K. (2003). Prelaunch and in-flight radiometric calibration of the Atmospheric Infrared Sounder (AIRS). IEEE Transactions on Geoscience and Remote Sensing, 41.2, 265– 273.

Pales, Jack C.; Keeling, Charles David (1965). "The Concentration of Atmospheric Carbon Dioxide in Hawaii". Journal of Geophysical Research. 70 (24): 6053–6076. Bibcode:1965JGR....70.6053P. doi:10.1029/JZ070i024p06053.

Ramanathan, V., R. J. Cicerone, H. B. Singh, and J. T. Kiehl. (1985). Trace Gas Trends and Their Potential Role in Climate Change." Journal of Geophysical Research: Atmospheres 90, no. D3: 5547-66.

Reuter, M., Buchwitz, M., Schneising, O., Noel, S., Bovensmann, H., Burrows, J., Boesch, H., Di Noia, A., Anand, J., Parker, R. J., Somkuti, P., Wu, L., Hasekamp, O. P., Aben, I., Kuza, A., Suto, H., Shiomi, K., Yoshida, Y., Morino, I., Crisp, D., O'Dell, C. W., Notholt, J., Petri, C., Warneke, T., Velazco, V. A., Deutscher, N. M., Griffith, D. W. T., Kivi, R., Pollard, D., Hase, F., Sussmann, R., Te, Y. V., Strong, K., Roche, S., Sha, M. K., De Maziere, M., Feist, D., Iraci, L., Roehl, C. M., Retscher, C. & Schepers, D. (2020). Ensemble-based satellite-derived carbon dioxide and methane column-averaged dry-air mole fraction data sets (2003-2018) for carbon and climate applications. Atmospheric Measurement Techniques, 13 (2), 789-819 https://ro.uow.edu.au/cgi/viewcontent.cgi?article=2211&context=smhpapers1

Richter-Menge, J., Druckenmiller, M. L., and M. Jeffries, M. E. 2019. Arctic Report Card 2019, https://www.arctic.noaa.gov/Report-Card.Razavi, A., Karagulian, F., Clarisse, L., Hurtmans, D., Coheur, P. F., Clerbaux, C., Müller, J. F., and Stavrakou, T. (2011). Global distributions of methanol and formic acid retrieved for the first time from the IASI/MetOp thermal infrared sounder, Atmos. Chem. Phys., 11, 857–872, https://doi.org/10.5194/acp-11-857-2011.

Rigby, M., Prinn, R. G., Fraser, P. J., Simmonds, P. G., Langenfelds, R. L., Huang, J., Cunnold, D. M., Steele, L. P., Krummel, P. B., Weiss, R. F., O'Doherty, S., Salameh, P. K., Wang, H. J., Harth, C. M., Mühle, J., and Porter, L. W. (2008).: Renewed growth of atmospheric methane, Geophys. Res. Lett., 35, 2–7,https://doi.org/10.1029/2008GL036037, 2008.

Rigby, M., Montzka, S. A., Prinn, R. G., White, J. W. C., Young, D., O'Doherty, S., Lunt, M. F., Ganesan, A. L., Manning, A. J., Simmonds, P. G., Salameh, P. K., Harth, C. M., Mühle, J., Weiss, R. F., Fraser, P. J., Steele, L. P., Krummel, P. B., McCulloch, A., and Park, S. (2017). Role of atmospheric oxidation in recent methane growth, P. Natl. Acad. Sci. USA, 114, 5373–5377, https://doi.org/10.1073/pnas.1616426114, 2017.

Rodgers, C. D. (1976). Retrieval of atmospheric temperature and composition from remote measurements of thermal radiation, Rev. Geophys. Space Phys., 14, 609 – 624, 1976.

Rodgers, C. D., (1990). Characterization and error analysis of profiles retrieved from remote sounding measurements, J. Geophys. Res., 95, 5587 5595.

Rodgers, C. D., Inverse Methods for Atmospheric Sounding: Theory and Practice, World Sci., River Edge, N. J., 2000.

Rodgers, C. D., and B. J. Connor, (2003). Intercomparison of remote sounding instruments, J. Geophys. Res., 108(D3), 4116, doi:10.1029/2002JD002299.

Rubino, M., Etheridge, D. M., Thornton, D. P., Howden, R., Allison, C. E., Francey, R. J., Langenfelds, R. L., Steele, L. P., Trudinger, C. M., Spencer, D. A., Curran, M. A. J., van Ommen, T. D., and Smith, A. M.: Revised records of atmospheric trace gases CO2, CH_4, N2O, and δ13C-CO2 over the last 2000 years from Law Dome, Antarctica, Earth Syst. Sci. Data, 11, 473–492, https://doi.org/10.5194/essd-11-473-2019, 2019.

Saad, K. M., Wunch, D., Deutscher, N. M., Griffith, D. W. T., Hase, F., De Mazière, M., Notholt, J., Pollard, D. F., Roehl, C. M., Schneider, M., Sussmann, R., Warneke, T., and Wennberg, P. O.: Seasonal variability of stratospheric methane: implications for constraining tropospheric methane budgets using total column observations, Atmos. Chem. Phys., 16, 14003–14024, https://doi.org/10.5194/acp-16-14003-2016, 2016.

Saunois, M., Bousquet, P., Poulter, B., Peregon, A., Ciais, P., Canadell, J. G., Dlugokencky, E. J., Etiope, G., Bastviken, D., Houweling, S., Janssens-Maenhout, G., Tubiello, F. N., Castaldi, S., Jackson, R. B., Alexe, M., Arora, V. K., Beerling, D. J., Bergamaschi, P., Blake, D. R., Brailsford, G., Brovkin, V., Bruhwiler, L., Crevoisier, C., Crill, P., Covey, K., Curry, C., Frankenberg, C., Gedney, N., Höglund-Isaksson, L., Ishizawa, M., Ito, A., Joos, F., Kim, H.-S., Kleinen, T., Krummel, P., Lamarque, J.-F., Langenfelds, R., Locatelli, R., Machida, T., Maksyutov, S., McDonald, K. C., Marshall, J., Melton, J. R., Morino, I., Naik, V., O'Doherty, S., Parmentier, F.-J. W., Patra, P. K., Peng, C., Peng, S., Peters, G. P., Pison, I., Prigent, C., Prinn, R., Ramonet, M., Riley, W. J., Saito, M., Santini, M., Schroeder, R., Simpson, I. J., Spahni, R., Steele, P., Takizawa, A., Thornton, B. F., Tian, H., Tohjima, Y., Viovy, N., Voulgarakis, A., van Weele, M., van der Werf, G. R., Weiss, R., Wiedinmyer, C., Wilton, D. J., Wiltshire, A., Worthy, D., Wunch, D., Xu, X., Yoshida, Y., Zhang, B.,

Zhang, Z., and Zhu, Q. (2016). The global methane budget 2000–2012, Earth Syst. Sci. Data, 8, 697–751, https://doi.org/10.5194/essd-8-697-2016.

Saunois, M., Bousquet, P., Poulter, B., Peregon, A., Ciais, P., Canadell, J. G., Dlugokencky, E. J., Etiope, G., Bastviken, D., Houweling, S., Janssens-Maenhout, G., Tubiello, F. N., Castaldi, S., Jackson, R. B., Alexe, M., Arora, V. K., Beerling, D. J., Bergamaschi, P., Blake, D. R., Brailsford, G., Bruhwiler, L., Crevoisier, C., Crill, P., Covey, K., Frankenberg, C., Gedney, N., Höglund-Isaksson, L., Ishizawa, M., Ito, A., Joos, F., Kim, H.-S., Kleinen, T., Krummel, P., Lamarque, J.-F., Langenfelds, R., Locatelli, R., Machida, T., Maksyutov, S., Melton, J. R., Morino, I., Naik, V., O'Doherty, S., Parmentier, F.-J. W., Patra, P. K., Peng, C., Peng, S., Peters, G. P., Pison, I., Prinn, R., Ramonet, M., Riley, W. J., Saito, M., Santini, M., Schroeder, R., Simpson, I. J., Spahni, R., Takizawa, A., Thornton, B. F., Tian, H., Tohjima, Y., Viovy, N., Voulgarakis, A., Weiss, R., Wilton, D. J., Wiltshire, A., Worthy, D., Wunch, D., Xu, X., Yoshida, Y., Zhang, B., Zhang, Z., and Zhu, Q. (2017). Variability and quasi-decadal changes in the methane budget over the period 2000–2012, Atmos. Chem. Phys., 17, 11135–11161, https://doi.org/10.5194/acp-17-11135-2017.

Saunois, M., Stavert, A. R., Poulter, B., Bousquet, P., Canadell, J. G., Jackson, R. B., Raymond, P. A., Dlugokencky, E. J., Houweling, S., Patra, P. K., Ciais, P., Arora, V. K., Bastviken, D., Bergamaschi, P., Blake, D. R., Brailsford, G., Bruhwiler, L., Carlson, K. M., Carrol, M., Castaldi, S., Chandra, N., Crevoisier, C., Crill, P. M., Covey, K., Curry, C. L., Etiope, G., Frankenberg, C., Gedney, N., Hegglin, M. I., Höglund-Isaksson, L., Hugelius, G., Ishizawa, M., Ito, A., Janssens-Maenhout, G., Jensen, K. M., Joos, F., Kleinen, T., Krummel, P. B., Langenfelds, R. L., Laruelle, G. G., Liu, L., Machida, T., Maksyutov, S., McDonald, K. C., McNorton, J., Miller, P. A., Melton, J. R., Morino, I., Müller, J., Murgia-

Flores, F., Naik, V., Niwa, Y., Noce, S., O'Doherty, S., Parker, R. J., Peng, C., Peng, S., Peters, G. P., Prigent, C., Prinn, R., Ramonet, M., Regnier, P., Riley, W. J., Rosentreter, J. A., Segers, A., Simpson, I. J., Shi, H., Smith, S. J., Steele, L. P., Thornton, B. F., Tian, H., Tohjima, Y., Tubiello, F. N., Tsuruta, A., Viovy, N., Voulgarakis, A., Weber, T. S., van Weele, M., van der Werf, G. R., Weiss, R. F., Worthy, D., Wunch, D., Yin, Y., Yoshida, Y., Zhang, W., Zhang, Z., Zhao, Y., Zheng, B., Zhu, Q., Zhu, Q., and Zhuang, Q. (2020) Supplemental data of the Global Carbon Project Methane Budget 2019 (Version 2.0), Data set, Global Carbon Project, https://doi.org/10.18160/GCP-CH_4-2019.

Schreck, C.J., III; Lee, H.T.; Knapp, K.R. HIRS Outgoing Longwave Radiation—Daily Climate Data Record: Application toward Identifying Tropical Subseasonal Variability. Remote Sens. 2018, 10, 1325.

Sellers, William D. (1969). <0392:AGCMBO>2.0.CO;2 "A Global Climatic Model Based on the Energy Balance of the Earth-Atmosphere System". Journal of Applied Meteorology. 8 (3): 392–400.

Shepherd, A., Ivins, E., Rignot, E. et al. Mass balance of the Greenland Ice Sheet from 1992 to 2018. Nature 579, 233–239 (2020). https://doi.org/10.1038/s41586-019-1855-2

Shindell, D., A.R. Ravishankara, J.C.I. Kuylenstierna, E. Michalopoulou, L. Höglund-Isaksson, Y. Zhang, K. Seltzer, M. Ru, R. Castelino, G. Faluvegi, V. Naik, L. Horowitz, J. He, J.-F. Lamarque, K. Sudo, W.J. Collins, C. Malley, M. Harmsen, K. Stark, J. Junkin, G. Li, A. Glick, and N. Borgford-Parnell, 2021: Global Methane Assessment: Benefits and Costs of Mitigating Methane Emissions. United Nations Environment Programme.

Smith, N.; Barnet, C.D. Uncertainty Characterization and Propagation in the Community Long-Term Infrared Microwave Combined Atmospheric Product System (CLIMCAPS). Remote Sens. 2019, 11, 1227. doi:10.3390/rs11101227.

Smith, W. L., and Woolf, H. M. (1976) The use of eigenvectors of statistical covariance matrices for interpreting satellite sounding radiometer observations. J. Atmos. Sci.,33, 1127–1140.

Stavert, A. R., Saunois, M., Canadell, J. G., Poulter, B., Jackson, R. B., Regnier, P., Lauerwald, R., Raymond, P. A., Allen, G. H., Patra, P. K., Bergamaschi, P., Bousquet, P., Chandra, N., Ciais, P., Gustafson, A., Ishizawa, M., Ito, A., Kleinen, T., Maksyutov, S., ... Zhuang, Q. (2022). Regional trends and drivers of the global methane budget. Global Change Biology, 28, 182–200. https://doi.org/10.1111/gcb.15901

Steele, L., Dlugokencky, E., Lang, P. et al. (1992). Slowing down of the global accumulation of atmospheric methane during the 1980s. Nature 358, 313–316. https://doi.org/10.1038/358313a0

Steele, L. P., P. J. Fraser, R. A. Rasmussen, M. A. K. Khalil, T. J. Conway, A. J. Crawford, R. H. Gammon, K. A. Masarie, and K. W. Thoning, The global distribution of methane in the troposphere, J. Atmos. Chem., 5, 125-171, 1987.

Strow, L.L.; Hannon, S.E.; Souza-Machado, S.D.; Motteler, H.E.; Tobin, D. An overview of the AIRS Radiative Transfer Model. IEEE Trans. Geosci. Remote Sensing 2003, 41, 303–313.

Sun, F.; Goldberg, M. D.; Liu, X.; Bates, J. J. (2010). Estimation of outgoing longwave radiation from Atmospheric Infrared Sounder radiance measurements. J. Geophys. Res. 2010, 115, D09103.

Susskind, J.; Barnet, C.D.; Blaisdell, J.M. Retrieval of atmospheric and surface parameters from AIRS/AMSU/HSB data in the presence of clouds. IEEE Trans. Geosci. Remote Sensing 2003, 41, 390–409.

Susskind, J.; Blaisdell, J.; Iredell, L.; Keita, F. (2011). Improved temperature sounding and quality control methodology using AIRS/AMSU data: The AIRS Science Team version 5 retrieval algorithm. IEEE Trans. Geosci. Remote Sens. 49, 883–907. doi:10.1109/TGRS.2010.2070508.

Susskind, J., Molnar, G., Iredell, L., and Loeb, N. G. (2012), Interannual variability of outgoing longwave radiation as observed by AIRS and CERES, J. Geophys. Res., 117, D23107, doi:10.1029/2012JD017997.

Susskind, J, Blaisdell, J. M., Iredell, L. (2014). Improved methodology for surface and atmospheric soundings, error estimates, and quality control procedures: the atmospheric infrared sounder science team version-6 retrieval algorithm. J. Appl. Remote Sens.. Vol. 8, No. 1, pp. 084994. DOI: 10.1117/1.JRS.8.084994 ISSN: 1931-3195

Tilmes, S., Lamarque, J.-F., Emmons, L. K., Kinnison, D. E., Ma, P.-L., Liu, X., Ghan, S., Bardeen, C., Arnold, S., Deeter, M., Vitt, F., Ryerson, T., Elkins, J. W., Moore, F., Spackman, J. R., and Val Martin, M. (2015). Description and evaluation of tropospheric chemistry and aerosols in the Community Earth System Model (CESM1.2), Geosci. Model Dev., 8, 1395–1426, https://doi.org/10.5194/gmd-8-1395-2015.

Tilmes, S., Hodzic, A., Emmons, L. K., Mills, M. J., Gettelman, A., Kinnison, D. E., et al. (2019). Climate forcing and trends of organic aerosols in the Community Earth System Model (CESM2). Journal of Advances in Modeling Earth Systems, 11, 4323– 4351. https://doi.org/10.1029/2019MS001827

Tobin, D. C., and Coauthors (2006). Radiometric and spectral validation of Atmospheric Infrared Sounder observations with the aircraft-based Scanning High-Resolution Interferometer Sounder. J. Geophys. Res., 111 , D09S02. doi:10.1029/2005JD006094.

Tobin, D. 2008. An SNO analysis of IASI and AIRS spectral radiances, GSICS Quarterly, vol. 2, no.3, pp. 2-4.

Turner, A. J., Jacob, D. J., Wecht, K. J., Maasakkers, J. D., Lundgren, E., Andrews, A. E., Biraud, S. C., Boesch, H., Bowman, K. W., Deutscher, N. M., Dubey, M. K., Griffith, D. W. T., Hase, F., Kuze, A., Notholt, J., Ohyama, H., Parker, R., Payne, V. H., Sussmann, R., Sweeney, C., Velazco, V. A., Warneke, T., Wennberg, P. O., and Wunch, D.: Estimating global and North American methane emissions with high spatial resolution using GOSAT satellite data, Atmos. Chem. Phys., 15, 7049–7069, https://doi.org/10.5194/acp-15-7049-2015, 2015.

Turner, A. J., Frankenberg, C., Wennberg, P. O., and Jacob, D. J.: Ambiguity in the causes for decadal trends in atmospheric methane and hydroxyl, P. Natl. Acad. Sci. USA, 114, 5367–5372, https://doi.org/10.1073/pnas.1616020114, 2017.

Turner, A. J., Frankenberg, C., and Kort, E. A.: Interpreting contemporary trends in atmospheric methane, P. Natl. Acad. Sci. USA, 116, 2805–2813, https://doi.org/10.1073/pnas.1814297116, 2019.

USGCRP, 2017: Climate Science Special Report: Fourth National Climate Assessment, Volume I [Wuebbles, D.J., D.W. Fahey, K.A. Hibbard, D.J. Dokken, B.C. Stewart, and T.K. Maycock (eds.)]. U.S. Global Change Research Program, Washington, DC, USA, 470 pp.

USGCRP, 2018: Impacts, Risks, and Adaptation in the United States: Fourth National Climate Assessment, Volume II [Reidmiller, D.R., C.W. Avery, D.R. Easterling, K.E. Kunkel,

K.L.M. Lewis, T.K. Maycock, and B.C. Stewart (eds.)]. U.S. Global Change Research Program, Washington, DC, USA, 1515 pp. doi: 10.7930/NCA4.2018.

Voulgarakis, A., Naik, V., Lamarque, J.-F., Shindell, D. T., Young, P. J., Prather, M. J., Wild, O., Field, R. D., Bergmann, D., Cameron-Smith, P., Cionni, I., Collins, W. J., Dalsøren, S. B., Doherty, R. M., Eyring, V., Faluvegi, G., Folberth, G. A., Horowitz, L. W., Josse, B., MacKenzie, I. A., Nagashima, T., Plummer, D. A., Righi, M., Rumbold, S. T., Stevenson, D. S., Strode, S. A., Sudo, K., Szopa, S., and Zeng, G. (2013). Analysis of present day and future OH and methane lifetime in the ACCMIP simulations, Atmos. Chem. Phys., 13, 2563–2587, https://doi.org/10.5194/acp-13-2563-2013.

Wang. L; Chen, Y. Inter-Comparing S-NPP and NOAA-20 CrIS Toward Measurement Consistency and Climate Data Records. IEEE J Sel Top Appl Earth Obs Remote Sens. 2019, 12, 2024-2031.

Wang T., Zhou L., Tan C., Divakarla M., Pryor K., Warner J., Wei Z., Goldberg M., and Nalli N. Validation of Near-Real-Time NOAA-20 CrIS Outgoing Longwave Radiation with Multi-satellite Datasets on Broad Timescales. Remote Sens. 2021

Wark, D. Q., and Fleming, H. E. (1966). Indirect measurements of atmospheric temperature profiles from satellites: I. Introduction. Mon. Wea. Rev.,94, 351–362.

Warner, J.X.; Wei, Z.; Strow, L.L.; Barnet, C.D.; Sparling, L.C.; Diskin, G.; Sachse, G. Improved agreement of AIRS tropospheric carbon monoxide products with other EOS sensors using optimal estimation retrievals. Atmos. Chem. Phys. 2010, 10, 9521–9533. doi:10.5194/acp-10-9521-2010.

Warner, J.X.; Carminati, F.; Wei, Z.; Lahoz, W.; Attié, J.L. Tropospheric carbon monoxide variability from AIRS under clear and cloudy conditions. Atmos. Chem. Phys. 2013, 13, 12469–12479. doi:10.5194/acp-13-12469-2013 .

Warner, J.X.; et al.. Tropospheric carbon gases observed from the Cross-track Infrared Sounder (CrIS). Atmos. Chem. Phys. 2022. Manuscript in preparation.

Weng, F.; Zou, X. Errors from Rayleigh-Jeans approximation in satellite microwave radiometer calibration systems. Appl. Opt. 2013, 52, 505–508.

Wielicki, B.A.; Barkstrom, B.R.; Harrison, E.F.; Lee III, R.B.; Smith, G.L.; Cooper, J.E. (1996). Clouds and the Earth's Radiant Energy System (CERES): An earth observing system experiment. Bull. Am. Meteorol. Soc. 77, 853–868.

Wilson, C., Chipperfield, M. P., Gloor, M., Parker, R. J., Boesch, H., McNorton, J., Gatti, L. V., Miller, J. B., Basso, L. S., and Monks, S. A.: Large and increasing methane emissions from eastern Amazonia derived from satellite data, 2010–2018, Atmos. Chem. Phys., 21, 10643–10669, https://doi.org/10.5194/acp-21-10643-2021, 2021.

WMO (2009). Technical Report of Global Analysis Method for Major Greenhouse Gases by the World Data Centre for Greenhouse Gases (Y. Tsutsumi, K. Mori, T. Hirahara, M. Ikegami and T.J. Conway). GAW Report No. 184 (WMO/TD-No. 1473), Geneva, 29 pp.

WMO (2011). Report of the 15th WMO/IAEA Meeting of Experts on Carbon Dioxide, Other Greenhouse Gases, and Related Tracers Measurement Techniques, Jena, Germany, 7–10 September 2009, GAW 194, available at: http://www.wmo.int/pages/prog/arep/ gaw/gaw-reports.html (last access: 28 January 2014), World, Meteorological Organization, Geneva, Switzerland, 2011.

WMO (2017). The State of Greenhouse Gases in the Atmosphere Based on Global Observations

through 2016, WMO Greenhouse Gas Bulletin, No. 13, 30 October 2017

WMO Greenhouse Gas Bulletin (GHG Bulletin) - No. 15. (2019). The State of Greenhouse Gases in the Atmosphere Based on Global Observations through 2018.

WMO Gas Station report. (2020) - WMO Global Atmosphere Watch (GAW) World Data Center for Greenhouse Gas (WDCGG) Data Summary No 43, March 2020. https://gaw.kishou.go.jp/static/publications/summary/sum43/sum43.pdf

Worden, J. R., Bloom, A. A., Pandey, S., Jiang, Z., Worden, H. M., Walker, T. W., Houweling, S., and Röckmann, T.: Reduced biomass burning emissions reconcile conflicting estimates of the post-2006 atmospheric methane budget, Nat. Commun., 8, 2227, https://doi.org/10.1038/s41467-017-02246-0, 2017.

Wunch, D., Toon, G. C., Blavier, J. F. L., Washenfelder, R. A., Notholt, J., Connor, B. J., Griffith, D. W., Sherlock, V., and Wennberg, P. O.: The total carbon column observing network, Philosophical Transactions of the Royal Society A: Mathematical, Phys. Eng. Sci., 369, 2087–2112, https://doi.org/10.1098/rsta.2010.0240, 2011.

Xie, P., & Arkin, P. A. (1996). Analyses of Global Monthly Precipitation Using Gauge Observations, Satellite Estimates, and Numerical Model Predictions, Journal of Climate, 9(4), 840-858.

Xie, Pingping, and Phillip A. Arkin. "Global Monthly Precipitation Estimates from Satellite-Observed Outgoing Longwave Radiation." Journal of Climate 11, no. 2 (1998): 137-64. Accessed August 31, 2020. http://www.jstor.org/stable/26242915.

Xiong, X., Barnet, C., Maddy, E., Sweeney, C., Liu, X., Zhou, L., and Goldberg, M. (2008), Characterization and validation of methane products from the Atmospheric Infrared Sounder (AIRS), J. Geophys. Res., 113, G00A01, doi:10.1029/2007JG000500.

Yokota, T., Yoshida, Y., Eguchi, N., Ota, Y., Tanaka, T., Watanabe, H., and Maksyutov, S.: Global concentrations of CO2 and CH_4 retrieved from GOSAT: first preliminary results, Scientific Online Letters on the Atmosphere, 5, 160–163, 2009.

Yue, Lambrigtsen, et al. (2020). AIRS Version 7 Level 2 Performance Test and Validation Report. Jet Propulsion Laboratory, California Institute of Technology.

Yurganov, Leonid & Leifer, Ira & Xiong, Xiaozhen. (2014). Atmospheric Methane over the Arctic Ocean: Thermal IR Satellite and Ship-Based Observations, by Leonid Yurganov. Seventh International Symposium on Non-CO2 Greenhouse Gases (NCGG7), November 5-7, 2014.

Zavyalov, V., Esplin, M., Scott, D., Esplin, B., Bingham, G., Hoffman, E., Lietzke C., Predina J., Frain R., Suwinski L., Han Y., Major C., Graham B., and Phillips, L.: Noise performance of the CrIS instrument, J. Geophys. Res.-Atmos., 118, 13108–13120, https://doi.org/10.1002/2013JD020457, 2013

Zhang, K., Goldberg, M.D., Sun, F., Zhou, L., Wolf, W.W., Tan,C., Nalli,N.R., Liu, Q. (2017). Estimation of Near Real-time Outgoing Longwave Radiation from Cross-track Infrared Sounder (CrIS) Radiance Measurements. J.Atmos.Ocean.Technol. 2017, 34, 643-655.

Zhang, X., Wang, F., Wang, W., Huang, F., Chen, B., Gao, L., Wang, S., Yan, H., Ye, H., Si, F., Hong, J., Li, X., Cao, Q., Che, H., Li, Z. (2020). The development and application of satellite remote sensing for atmospheric compositions in China, Atmospheric Research, Volume 245, 105056, ISSN 0169-8095, https://doi.org/10.1016/j.atmosres.2020.105056.

Zhang, Z., Zimmermann, N. E., Calle, L., Hurtt, G., Chatterjee, A., and Poulter, B.: Enhanced response of global wetland methane emissions to the 2015–2016 El Niño-Southern Oscillation event, Environ. Res. Lett., 13, 7, https://doi.org/10.1088/1748-9326/aac939, 2018.

Zhou, L.; Divakarla, M.; Liu, X.; Layns, A.; Goldberg, M. An Overview of the Science Performances and Calibration/Validation of Joint Polar Satellite System Operational Products. Remote Sens. 2019, 11, 698.

Zhou, L., Warner, J., Nalli, N. R., Divakarla, M., Pryor, K., Wei, Z., Liu X, and Kalluri, S. (2022). Spatial and Temporal Variability of Global Atmospheric Methane Seen by Two Decades of U. S. Hyperspectral Infrared Sounders. Remote Sensing, submitted and under review

Zhou L, Divakarla M, Liu X, Layns A, Goldberg M. (2019). An Overview of the Science Performances and Calibration/Validation of Joint Polar Satellite System Operational Products. Remote Sensing 11: 698, 2019. doi: 10.3390/rs11060698.

Zou, C.-Z., Zhou, L., Lin, L., Sun, N., Chen, Y., Flynn, L. E., Zhang, B., Cao, C., Iturbide-Sanchez, F., Beck, T., Yan, B., Kalluri, S., Bai, Y., Blonski, S., Choi, T., Divakarla, M., Gu, Y., Hao, X., Li, W., … Goldberg, M. D. (2020). The Reprocessed Suomi NPP Satellite Observations. Remote Sensing, 12(18), 2891.